UNIVERSIDAD POLITÉCNICA DE MADRID
ESCUELA TÉCNICA SUPERIOR DE INGENIEROS DE TELECOMUNICACIÓN

RADIOFREQUENCY ARCHITECTURES AND TECHNOLOGIES FOR SOFTWARE DEFINED RADIO

TESIS DOCTORAL

Cristina de la Morena Álvarez-Palencia
Ingeniera de Telecomunicación

2012

DEPARTAMENTO DE SEÑALES, SISTEMAS Y RADIOCOMUNICACIONES

ESCUELA TÉCNICA SUPERIOR DE INGENIEROS DE TELECOMUNICACIÓN

UNIVERSIDAD POLITÉCNICA DE MADRID

RADIOFREQUENCY ARCHITECTURES AND TECHNOLOGIES FOR SOFTWARE DEFINED RADIO

TESIS DOCTORAL

Autor:
Cristina de la Morena Álvarez-Palencia
Ingeniera de Telecomunicación

Director:
Mateo Burgos García
Catedrático del Departamento de Señales Sistemas y Radiocomunicaciones
Universidad Politécnica de Madrid

2012

TESIS DOCTORAL

RADIOFREQUENCY ARCHITECTURES AND TECHNOLOGIES FOR SOFTWARE DEFINED RADIO

AUTOR: Cristina de la Morena Álvarez-Palencia
DIRECTOR: Mateo Burgos García

Tribunal nombrado por el Magfco. y Excmo. Sr. Rector de la Universidad Politécnica de Madrid, el día ___ de _____ de 2012.

PRESIDENTE: Félix Pérez Martínez

SECRETARIO: Manuel Sierra Castañer

VOCAL: João Nuno Pimentel Silva Matos

VOCAL: Eduardo Artal Latorre

VOCAL: Iván Alejandro Pérez Álvarez

SUPLENTE: Blas Pablo Dorta Naranjo

SUPLENTE: Íñigo Ederra Urzainqui

Realizado el acto de defensa y lectura de Tesis el día ___ de _____ de 2012, en la E.T.S. de Ingenieros de Telecomunicación, Madrid.

Calificación:

EL PRESIDENTE LOS VOCALES

EL SECRETARIO

‘Dans les champs de l'observation le hasard ne favorise que les esprits préparés’

‘In the fields of observation chance favors only the prepared mind’

Louis Pasteur

Acknowledgments

First of all, I would like to thank my supervisor, Professor Mateo Burgos García, for giving me the opportunity to work under his direction. I really appreciate all his support, guidance, vast knowledge, and helpful advices.

Special thanks to my collages and friends of the Grupo de Microondas y Radar. We have shared many good times that I will never forget.

I am extremely grateful to Professor Bernard Huyart, who gave me the opportunity to do a research stay in the Telecom ParisTech. I would like to thank him, and the rest of the member of the Radiofrequencies and Microwave Group, for their hospitality and kindness during my stay.

Last but no least, thanks to my family for the support they provided me through my entire life. You are the most important thing to me.

This research was performed in the Microwave and Radar Group of the Department of Signals, Systems, and Radiocommunications, Technical University of Madrid. It was sponsored in part by the Spanish National Board of Scientific and Technological Research (CICYT), under project contracts TEC2005-07010-C02-01, TEC2008-02148, and TEC2011-28683-C02-01; and in part by INDRA Sistemas, under TelMAX Project. Acknowledgments to the grant “IX Convocatoria de Ayudas del Consejo Social, Universidad Politécnica de Madrid” for its financial support for the research stay in Telecom ParisTech.

Resumen

La red de seis puertos es una interesante arquitectura de radiofrecuencia que alberga múltiples posibilidades. Surgida en la década de los setenta como una alternativa a los analizadores de redes, en los últimos años se ha empleado en numerosas aplicaciones, tales como receptores homodinos, sistemas radar, detección de ángulos de llegada, UWB (*Ultra-Wide-Band*) o sistemas MIMO (*Multiple Input Multiple Output*). En la actualidad, se perfila como una de las mejores candidatas para implementar una Radio Definida por Software (SDR).

En esta tesis se estudia en profundidad esta prometedora arquitectura, describiendo sus fundamentos teóricos y realizando un estudio del estado del arte. Además, se presenta el diseño y desarrollo de un prototipo de receptor de seis puertos de banda ancha (0.3-6 GHz) para SDR, implementado en tecnología convencional. El sistema será caracterizado experimentalmente y validado para la demodulación de señales de radio frecuencia. El estudio y análisis de la arquitectura de seis puertos se completa con su comparación, teórica y experimental, con otras arquitecturas de RF, desde el punto de vista de su posible aplicación para SDR.

Varias son las aportaciones novedosas que se plantean en esta tesis. Dichas aportaciones se orientan en dos direcciones claras, que se corresponden con los actuales temas de interés en redes de seis puertos: desarrollo y optimización de técnicas de regeneración I-Q y algoritmos de calibración en tiempo real para redes multipuerto; y búsqueda de nuevas técnicas y tecnologías que contribuyan a la miniaturización de la arquitectura de seis puertos. En concreto, las contribuciones novedosas desarrolladas en esta tesis se resumen en:

- Introducción de un nuevo método de auto-calibración en tiempo real para redes multipuerto y aplicaciones de banda ancha, basado en canalización digital.

- Introducción de una nueva técnica de regeneración directa de componentes I-Q para receptores de cinco puertos.

- Contribución a la miniaturización de receptores de seis puertos mediante el uso de la tecnología multicapa LTCC (*Low Temperature Cofired Ceramic*). Desarrollo de un receptor de seis puertos en tecnología LTCC de banda ancha (0.3-6 GHz) y tamaño reducido (30x30x1.25 mm).

Los resultados y conclusiones derivados de los estudios desarrollados en esta tesis han sido muy satisfactorios. En consecuencia, varias son las publicaciones científicas relacionadas con esta tesis. En concreto, catorce suman el número de publicaciones entre revistas, congresos internacionales y congresos nacionales, más un artículo de revista adicional que se encuentra actualmente en proceso de revisión.

Abstract

Six-port network is an interesting radiofrequency architecture with multiple possibilities. Since it was firstly introduced in the seventies as an alternative network analyzer, the six-port network has been used for many applications, such as homodyne receivers, radar systems, direction of arrival estimation, UWB (*Ultra-Wide-Band*), or MIMO (*Multiple Input Multiple Output*) systems. Currently, it is considered as a one of the best candidates to implement a Software Defined Radio (SDR).

This thesis comprises an exhaustive study of this promising architecture, where its fundamentals and the state-of-the-art are also included. In addition, the design and development of a SDR 0.3-6 GHz six-port receiver prototype is presented in this thesis, which is implemented in conventional technology. The system is experimentally characterized and validated for RF signal demodulation with good performance. The analysis of the six-port architecture is complemented by a theoretical and experimental comparison with other radiofrequency architectures suitable for SDR.

Some novel contributions are introduced in the present thesis. Such novelties are in the direction of the highly topical issues on six-port technique: development and optimization of real-time I-Q regeneration techniques for multiport networks; and search of new techniques and technologies to contribute to the miniaturization of the six-port architecture. In particular, the novel contributions of this thesis can be summarized as:

- Introduction of a new real-time auto-calibration method for multiport receivers, particularly suitable for broadband designs and high data rate applications.
- Introduction of a new direct baseband I-Q regeneration technique for five-port receivers.
- Contribution to the miniaturization of six-port receivers by the use of the multilayer LTCC (*Low Temperature Cofired Ceramic*) technology. Implementation of a compact (30x30x1.25 mm) broadband (0.3-6 GHz) six-port receiver in LTTC technology.

The results and conclusions derived from this thesis have been satisfactory, and quite fruitful in terms of publications. A total of fourteen works have been published, considering international journals and conferences, and national conferences. Aditionally, a paper has been submitted to an internationally recognized journal, which is currently under review.

Index of contents

Index of figures

Index of tables

List of abbreviations

***3G**: Third Generation Mobile Communications.*
***4G**: Fourth Generation Mobile Communications.*
***ADC, A/D**: Analog to Digital Converter.*
***ADS**: Advanced Design Systems.*
***AGC**: Automatic Gain Control.*
***ASIC**: Application Specific Integrated Circuits.*
***AWGN**: Additive White Gaussian Noise.*
***BER**: Bit Error Rate.*
***BPSK**: Binary Phase-Shift Keying.*
***CPU**: Central Processing Unit.*
***DAC, D/A**: Digital to Analog Converter.*
***DC**: Direct Current.*
***DoA**: Direction of Arrival.*
***DSP**: Digital Signal Processor.*
***DUT**: Device-Under-Test.*
***EVM**: Error Vector Magnitude.*
***FIR**: Finite Impulse Response.*
***FPGA**: Field Programmable Gate Array.*
***GSM**: Global System for Mobile communication.*
***IC:** Integrated Circuit.*
***IF:** Intermediate Frequency.*
***IMD2:** Second-order intermodulation distortion.*
***IP3**: Third Order Intermodulation Point.*
***JTRS**: Joint Tactical Radio Service.*
***LNA**: Low Noise Amplifier.*
***LTE**: Long Term Evolution.*
***LO**: Local Oscillator.*
***LTCC**: Low Temperature Cofired Ceramic.*
***MEMS:** MicroElectroMechanical Systems.*
***MIC**: Microwave Integrated Circuit.*
***MIMO**: Multiple Input Multiple Output.*
***MMIC**: Monolithic Microwave Integrated Circuit.*
***P_{1dB}**: 1 dB Compression Point.*
***PCS**: Personal Communications Service.*
***PSK**: Phase-Shift Keying.*
***QAM**: Quadrature Amplitude Modulation.*

***QoS**: Quality of Service.*
***QPSK**: Quadrature Phase-Shift Keying.*
***RF**: Radiofrequency.*
***RFC:** Radiofrequency Choke.*
***SDR**: Software Defined Radio.*
***SIW**: Substrate Integrated Waveguide.*
***SNR**: Signal to Noise Ratio.*
***UMTS**: Universal Mobile Telecommunications System.*
***UWB**: Ulta-Wide-Band.*
***VSWR**: Voltage Standing Wave Ratio.*
***VSG:** Vector Signal Generator.*
***WiMAX**: Worldwide Interoperability for Microwave Access.*
***WLAN**: Wireless Local Area Network.*
***WPAN**: Wireless Personal Area Network.*

Chapter 1

INTRODUCTION

1.1 OVERVIEW OF SOFTWARE DEFINED RADIO IMPLEMENTATION

Information and telecommunication technologies are evolving towards a new concept of information society, where different communication standards are combined to form heterogeneous networks. This is precisely the concept of 4G or *Beyond* 3G, since GSM and UMTS are combined with different access technologies, such us WLAN (*Wireless Local Area Network*) and WPAN (*Wireless Personal Area Network*). Users are demanding to communicate using different services, from wherever and whenever they want. However, the main problem derives from the incompatibility between the different standards and technologies.

Software Defined Radio (SDR) is thought to play an important role in future communication systems, due to its reconfiguration and multi-mode operation capabilities. These features enable to change the system functionality without any change in the hardware, providing a cost reduced solution to perform a multi-mode, multi-band, and multi-standard radio platform. Following the SDR forum definition [1], a SDR is a *"radio in which some or all the physical layer functions are software defined"*. SDR provides end-users a dynamic spectrum access, and the capability of communicating whatever, wherever and whenever they need. The benefits of SDR technology are having a significant impact on the area of wireless and military communications, and this trend is expected to continue over the next years [2]-[4]. At present, SDR is increasingly implemented in both military and commercial networks in more modest ways: 3G base stations and their user equipments; military radios such as JTRS (*Joint Tactical Radio Service*) in EEUU [5]; terrestrial mobile radios, such as

Project 25 (APCO-P25) in EEUU [6] or *Mesa Project* in Europe [7]; satellite transceivers; etc.

The original idea of a SDR hardware implementation, conceived by Mitola in 1995 [8], consisted of placing the ADC (*Analog to Digital Converter*) just at the output of the antenna. Digital processing is performed by software, using DSPs (*Digital Signal Processors*), FPGAs (*Field Programmable Gate Array*) o ASICs (*Application Specific Integrated Circuits*). However, this implementation is currently impossible, due to the ADC limitations as for speed, dynamic range, jitter and power consumption [9]. For example, a 12 bit 11 Gsample/s ADC would be required to digitalize the frequency range from 800 MHz to 5.5 GHz, where all cellular communications and WLAN are located at present [10]. Obviously, such an ADC is currently impossible. But in the case it were possible, its power dissipation would be prohibitive. The state of the art is nowadays around 16 bit 130 MS/s A/D conversion for commercial Mitola's type SDRs. In practice, the SDR hardware is composed of a reconfigurable baseband digital signal stage and a broadband radio frequency (RF) front-end.

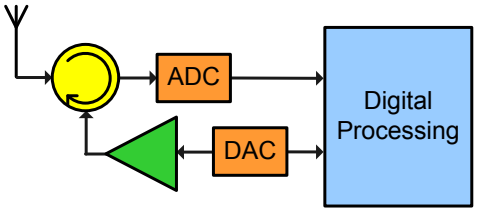

Fig.1.1: Ideal SDR implementation.

Until now, conventional multi-band receivers have consisted of a different reception chain for each standard. This solution is not cost efficient, as it requires specific circuits for each standard, which increase the volume of the radio terminal. On the contrary, a SDR is composed of a single broadband reception stage. All channels are converted to digital domain with a high speed ADC, and channel selection is performed by software defined filters. However, the design of a universal general-purpose broadband RF front-end, with multi-mode and reconfiguration features, is not a simple matter. Furthermore, the difficulty increases if other aspects such as volume or cost are also taken into account.

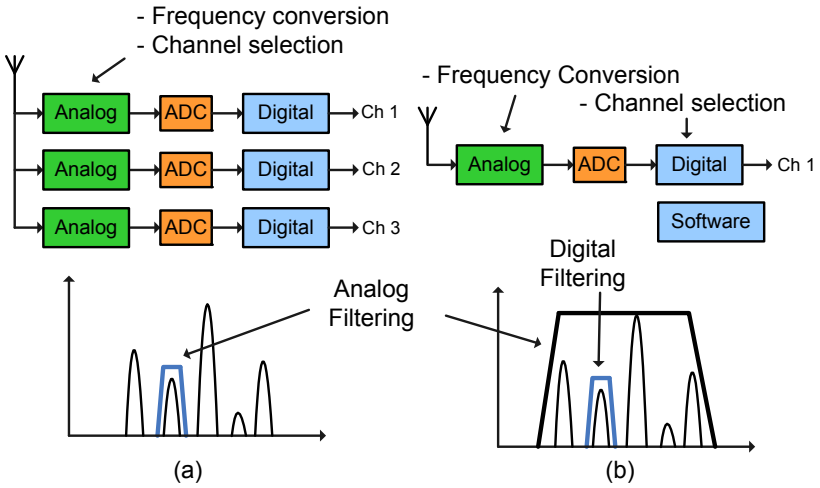

Fig. 1.2: Comparison between (a) Conventional multimode radio, and (b) SDR.

Superheterodyne architecture has been the classical configuration in radiocommunications, due to its selectivity and sensitivity characteristics. However, superheterodyne receivers are complex and expensive, as they require a large number of external components, including bulky RF filters for image frequency rejection. Another problem is the difficulty of changing system parameters such as bandwidth, because RF and IF signals are processed by fixed narrowband analog components, which make difficult to achieve a broadband system with multimode operation. Consequently, heterodyne architecture is not the best option when a SDR hardware implementation is addressed.

Two more suitable alternatives to implement a SDR are the direct frequency conversion architecture, also named homodyne or zero-IF, and the low-IF architecture [9]-[12]. Zero-IF and low-IF architectures have many advantages suitable for SDR, such as flexibility, reconfigurability, low-cost, simplicity, compact size, and high level of integration. However, these architectures have some limitations. In the case of zero-IF receivers, these limitations include DC-offset, 1/f noise, and second-order intermodulation distortion (IMD2). Regarding to the low-IF configuration, the image frequency continues being the main problem. Moreover, the trend towards high data rates services will require larger bandwidths, which become possible at high frequencies. Nevertheless, I-Q mod/demodulators cannot operate in very large frequency ranges, so the use of zero-IF and low-IF architectures is limited by these devices.

Six-port network is an innovative and interesting architecture that is nowadays emerging as a promising alternative, as it does not use I-Q mixers for the frequency conversion [13]-[16]. The main characteristic of the six-port architecture is its extremely large bandwidth, which involves multi-band and multi-mode capabilities. Six-port networks can operate at very high frequencies [17]-[20], being a serious alternative for millimetre-wave frequencies and large relative-bandwidth applications. Furthermore, the six-port architecture can perform high data rates. A 200 Mbps data rate was estimated in 2008 [14], although recent publications have demonstrated the six-port capacity to demodulate 1.7 Gbps signals [21]. These and other advantages make this architecture to be considered a good candidate to implement a SDR.

However, apart from well known problems of direct conversion architectures, there are some issues in six-port networks that need intensive research. On one hand, six-port receivers require a calibration process to recover the original signal. Traditional physical calibration procedures, consisting on measuring the system using several external physical standards terminals, are impractical for a wireless receiver or a SDR, owing to their lack of dynamism and flexibility. Moreover, the performance of current real-time calibration methods will diminish when dealing with high-speed signals. On the other hand, the large dimensions of the passive six-port structure, especially for operating frequencies in the lower gigahertz region, could be prohibitive, for example, for mobile communication applications. In fact, the miniaturization of six-port receivers is the focus of current work.

1.2 MOTIVATION AND SCOPE OF THE THESIS

The present thesis is mainly concerned with the investigation and optimization of RF architectures, in order to achieve a universal and flexible radio platform, with multi-mode and multi-band capabilities. In particular, this thesis focuses on the study of a very promising RF architecture, the six-port architecture, and its possible application to SDR.

Five main issues are addressed in this thesis:

1. Development and validation of a broadband six-port receiver for SDR and high-speed applications. Demonstration of the multi-band and

multi-mode operation capabilities of the six-port receiver in the demodulation of RF signals.

2. Experimental comparison between six-port and conventional zero-IF and low-IF architectures.
3. Research and development of new and efficient multi-port calibration methods for digital IQ regeneration.
4. Investigation on new techniques for real-time analog I-Q regeneration.
5. Contribution to the miniaturization of six-port receivers.

The first two issues comprise an exhaustive study of the six-port architecture. The last three points are the main novel contributions of this thesis, as they are related to the topics that are currently having more intensive research in six-port networks.

1.3 THESIS ORGANIZATION

The thesis organization reflects the main directions of the research:

- Chapter 2 reviews the fundamentals of the three RF architectures with more possibilities to implement a SDR, i.e., zero-IF, low-IF, and six-port network.
- Chapter 3 addresses the design, development, and experimental characterization of an extremely large relative bandwidth six-port receiver.
- Chapter 4 presents an experimental comparison between the six-port receiver, and conventional zero-IF/low-IF receivers.
- Chapter 5 proposes two new I-Q regeneration techniques for six/five-port receivers. The first one is a real-time multi-port auto-calibration method, suitable for broadband applications and high-speed signals. The second technique is a direct baseband IQ recovery technique for five-port receivers, based on the use of a simple analog IQ regeneration circuit.
- Chapter 6 explores the possibilities of the LTCC technology in the miniaturization of six-port receivers. The design, development and characterization of a reduced LTCC six-port receiver are included in this chapter.
- Chapter 7 exposes the conclusions and future work.

1.4 LIST OF PUBLICATIONS

[TOEEJ 2008] C. de la Morena-Álvarez-Palencia, M. Burgos-García, F. Pérez-Martínez, "A Novel and Simple Maximum Available Gain Equalization Technique for Microwave Amplifiers," *The Open Electrical and Electronic Engineering Journal*, vol. 2, pp. 45-49, May 2008.

[URSI 2008] C. de la Morena-Álvarez-Palencia, A. Martín-López, M. Burgos-García, "Comparación entre arquitecturas de RF para Radio Definida por Software", *XXIII Simposium Nacional de la Unión Científica Internacional de Radio URSI 2008*, Madrid, Spain, 22-24 Sept. 2008, pp. 149.

[SDRF 2009] C. de la Morena-Álvarez-Palencia, M. Burgos-García, "Reconfigurable radio technologies for professional wide band communications", in *European Reconfigurable Radio Technologies Workshop and Product Exposition*, *SDR forum*, Madrid, Spain, 22-24 April 2009. Available: *http://groups.winnforum.org/p/cm/ld/fid=69*.

[URSI 2009] C. de la Morena Álvarez-Palencia, M. Burgos García, "Método de autocalibración canalizado para red de seis puertos", in *XXIV Simposium Nacional de la Unión Científica Internacional de Radio URSI 2009*, Santander, Spain, 16-18 Sept. 2009, pp. 97.

[URSI 2010-1] C. de la Morena-Álvarez-Palencia, M. Burgos-García, J. Gismero-Menoyo, "Aplicación de la tecnología LTCC para la miniaturización de redes de seis puertos", in *XXV Simposium Nacional de la Unión Científica Internacional de Radio URSI 2010*, Bilbao, Spain, 15-17 Sept. 2010, pp. 28.

[URSI 2010-2] D. Rodríguez-Aparicio, C. de la Morena-Álvarez-Palencia, M. Burgos-García, "Receptores zero-IF y low-IF para radio definida por software", in *XXV Simposium Nacional de la Unión Científica Internacional de Radio URSI 2010*, Bilbao, Spain, 15-17 Sept. 2010, pp. 39.

[EuMC 2010] C. de la Morena-Álvarez-Palencia, M. Burgos-García, D. Rodríguez-Aparicio, "Three octave six-port network for a broadband software radio receiver", in *40th European Microwave Conference*, Paris, France, 28-30 Sept. 2010, pp. 1110-1113.

[ICCST 2010] C. de la Morena-Álvarez-Palencia, M. Burgos-García, D. Rodríguez-Aparicio, "Software Defined Radio technologies for emergency and professional wide band communications," in *IEEE Int. Carnahan Conf. Security Tech.*, San Jose, CA, 5-8 Oct. 2010, pp. 357-363.

[MILCOM 2010] C. de la Morena-Álvarez-Palencia, M. Burgos-García, "Broadband RF front-end based on a six-port network architecture for software defined radio," in *IEEE Military Communication Conference*, San Jose, CA, 31 Oct. - 3 Nov. 2010, pp. 651-656.

[PIER 2011] C. de la Morena-Álvarez-Palencia, M. Burgos, "Four-octave six-port receiver and its calibration for boradband communications and software defined radios," *Progress in Electromagnetics Research*, vol. 116, pp. 1-21, April 2011.

[URSI 2011] C. de la Morena-Álvarez-Palencia, M. Burgos-García, "Comparación experimental de receptores para radio definida por software", in *XXVI Simposium Nacional de la Unión Científica Internacional de Radio URSI 2011*, Leganés, Spain, 6-9 Sept. 2011, pp. 24.

[EuMC 2011] C. de la Morena-Álvarez-Palencia, M. Burgos, J. Gismero-Menoyo "Contribution of LTCC technology to the miniaturization of six-port networks," in *41th European Microwave Conference*, Manchester, UK, 10-13 Oct. 2011, pp. 659-662.

[MTT 2012-1] C. de la Morena-Álvarez-Palencia, K. Mabrouk, B. Huyart, A. Mbaye, M. Burgos-García, "Direct baseband I-Q regeneration method for five-port receivers improving DC-offset and second-order intermodulation distortion rejection," *IEEE Trans. Microwave Theory Tech.*, accepted for publication.

[URSI 2012] C. de la Morena-Álvarez-Palencia, M. Burgos-García, J. Gismero-Menoyo, “Diseño y construcción de una red de seis puertos LTCC para un receptor radio software”, in *XXVII Simposium Nacional de la Unión Científica Internacional de Radio URSI 2012*, Elche, Spain, Sept. 2012, accepted for publication.

[MTT 2012-2] C. de la Morena-Álvarez-Palencia, M. Burgos-García, J. Gismero Menoyo, "Miniaturized 0.3-6 GHz LTCC six-port receiver for software defined radio," *IEEE Trans. Microwave Theory Tech.*, submitted for publication.

Table 1.1 Relation between objectives and publications of the thesis.

Chapter	Objective	Publications
2	Study and optimization of RF architectures for SDR implementation	[TOEEJ 2008] [URSI 2008] [SDRF 2009]
3	Development and validation of a broadband six-port receiver for SDR and high-speed applications	[EuMC 2010] [MILCOM 2010] [PIER 2011]
4	Experimental comparison between six-port and conventional zero-IF and low-IF architectures	[ICCST 2010] [URSI 2010-2] [URSI 2011]
5	Research and development of new and efficient multi-port calibration methods for digital IQ regeneration	[URSI 2009] [PIER 2011]
5	Investigation on new techniques for real-time analog I-Q regeneration	[MTT 2012-1]
6	Miniaturization of six-port receivers: development of a compact broadband LTCC six-port receiver	[EuMC 2011] [URSI 2010-1] [URSI 2012] [MTT 2012-2]

Chapter 2

STUDY OF RADIO FREQUENCY ARCHITECTURES FOR SOFTWARE DEFINED RADIO

2.1 INTRODUCTION

This chapter presents the study of the three RF architectures with more possibilities to implement a SDR: zero-IF, low-IF, and six-port network. Their fundamentals, as well as their main advantages and drawbacks, are described below. The state of the art in SDR applications is also presented for the three architectures.

2.2 ZERO-IF

2.2.1 Fundamentals of zero-IF

The first circuit based on the homodyne principle was published by Colebrook in 1924 [22]. Thus, the homodyne architecture, also known as direct frequency conversion or zero-IF, is nearby as old as the superheterodyne, which was introduced in 1918 by E.H. Armstrong [23]. Thereafter, the homodyne principle aroused the scientific community interest [24]. However, no commercial applications appeared to be found for this architecture, which has been tried (and failed) many times. The homodyne architecture reappeared with more strength in the 90s [25]-[27]. Due to the advances in IC (*Integrated Circuit*) technology and the possibilities of the digital domain, zero-IF receivers are no longer being considered impractical solutions. Nowadays, zero-IF transceivers are thought to be a serious alternative to classical

heterodyne systems for several applications, especially SDR, where high level of integration and low-cost solutions are required [9]-[12].

The typical configuration of a zero-IF receiver is represented in Fig. 2.1. It is a simple structure, where the RF signal is directly down-converted to zero frequency by means of an I-Q demodulator and a local oscillator (LO) of the same frequency. Next, the I-Q components are low-pass filtered and converted to digital domain with an ADC.

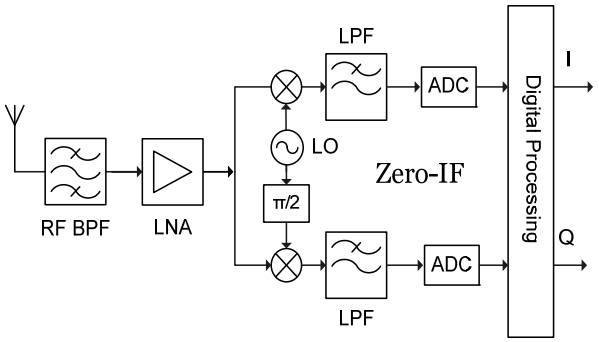

Fig. 2.1: Block diagram of a zero-IF receiver.

The direct conversion architecture comprises clear benefits with respect to the heterodyne. On one hand, since IF is equal to zero, zero-IF receivers does not suffer from the image frequency problem. Therefore, large costly image rejection filters and IF circuits can be eliminated. On the other hand, main operations such as channel selection and amplification are baseband performed, where integration is much easier. Channel filtering can be performed either with a simple low-pass filter or in the digital domain, which raises the possibility of having a universal and multi-standard RF front-end. All these characteristics entail high level of integration, compact size, simplicity, low-power consumption, flexibility and system reconfigurability. Consequently, the direct-conversion architecture is very attractive for integrated and reconfigurable RF receivers. Nonetheless, it suffers from a number of problems that do not exist or are not as serious as in heterodyne receivers [26],[27]. This has been mainly the reason why homodyne receivers have not been as popular as heterodyne ones.

A. DC-offset

Since the downconverted spectrum is located around zero frequency, DC voltage can distort the signal and substantially degrade the bit-error probability.

Furthermore, this offset voltage must be removed in the analog domain prior to sampling, otherwise, it can saturate the baseband amplifiers and ADCs [28]. There are two types of DC-offsets:

- Time-invariant DC-Offset. It is caused by the inherent DC value in the analog circuits and, therefore, it does not vary with time. Time-invariant offset is mainly generated in the LNA or the I-Q demodulator, due to drifts or mismatches in the analog circuits.

- Time variant DC-Offset. It consists in the phenomenon known as self-mixing. The self-mixing occurs when a strong, nearby signal mixes with itself, producing a DC component that appears as interference at the centre of the desired signal. This situation may take place in the cases shown in Fig. 2.2. Due to the isolation between the LO port and the inputs of the mixer and the LNA is not perfect, the LO signal is leaked to the inputs of the LNA and the mixer, producing a DC component at the output of the mixer -Fig. 2.2(a)-. The same effect happens when a strong interference leaks from the LNA or mixer input to the LO port and is multiplied by itself -Fig. 2.2(c)-. Moreover, DC-offset can be produced when the LO leakage signal in the LNA input is radiated from the antenna and reflected from external objects -Fig. 2.2(b)-. The amount of DC-offset coming from radiation is very difficult to predict, since its magnitude can change rapidly with the object movement, fading and multipath reception, etc.

There are many methods for rejecting DC-offset in direct conversion receivers. The simplest solution is by high-pass filtering with a series capacitor (AC-coupling). However, this method is not always feasible. The cut-off frequency of the high-pass filter (HPF) has to be very low for not corrupting the wanted signal, leading to large size capacitors with slow response to variations, in particular for narrow band signals. As for Razavi [27], simulations indicate that the corner frequency of the HPF must be less than 0.1% of the data rate for the signal degradation to be negligible. Thus, for example, a data rate of 48.6 kb/s mandates a corner frequency less than 50 Hz. Abidi [26] points that '*simulations on a representative 200 kHz wide spectrum (150kbps, roll-off=0.35) suggest that at a target bit-error rate of 10-3, a 5 Hz notch at dc causes about 0.2 dB loss in receiver sensitivity, yet this notch need only widen to 20 Hz when the receiver will cease to function*'. One possible solution consists in minimizing the

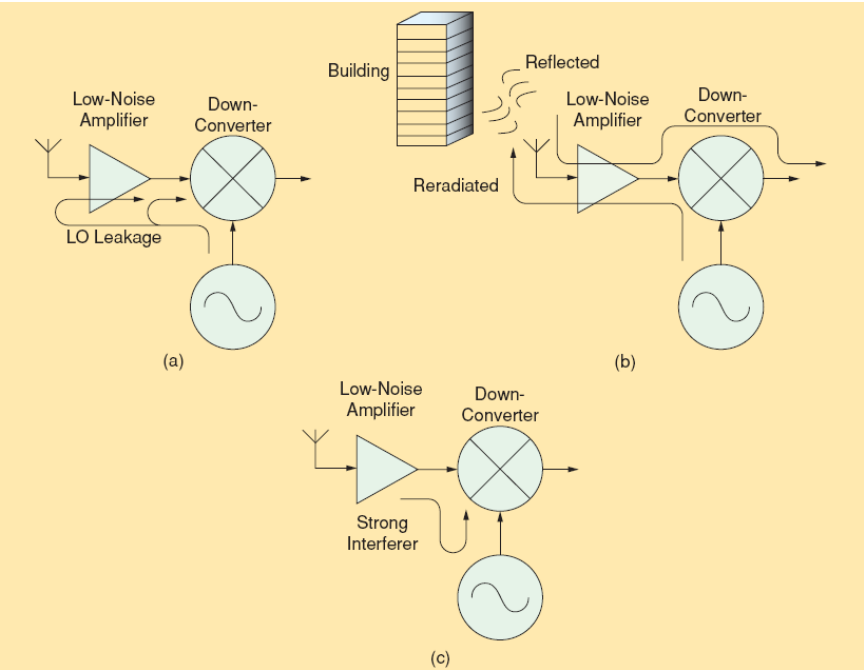

Fig. 2.2: DC-offset mechanisms: (a) Self-mixing of LO (b)LO reradiation (c) Self-mixing of interferers (*© 2005 IEEE* [28]).

signal energy around DC by choosing DC-free modulation schemes, such as BFSK (binary frequency shift keying) [29]. In such a case, a reasonable high-pass filtering can be performed, especially for wideband channels.

Most of the proposed alternatives for the DC-offset rejection consist in improving the mixer characteristics. This is useful not only for eliminating DC-offset, but also other typical zero-IF problems [30],[31]. Other methods are based on the use of either analogical [32],[33] or digital DC-offset cancelling loops, although the combination of both [34] is more effective. In fact, the habitual procedure consists in combining both analogical and digital methods. Therefore, it is usual to apply digital compensation, equalization or calibration techniques, together with some of the methods presented above [35]-[37].

B. I-Q imbalances

The drifts in the nominally 90º phase shift and mismatches between the amplitudes of the I-Q signals distort the downconverted constellation, increasing the BER (bit error rate) [27]. While gain error simply appears as a non unity scale factor in the amplitude, phase imbalance corrupts one channel with a fraction of the data

pulses in the other channel, degrading the signal-to-noise ratio if the I and Q data streams are uncorrelated. Consequently, I-Q demodulator becomes a key element in direct conversion receivers. Nevertheless, I-Q mismatch is much less problematic in direct conversion schemes than in image-reject architectures.

C. Flicker noise

Flicker noise is characterized by presenting a power spectral density inversely proportional to the frequency. That is the reason why it is also called 1/f noise. Since 1/f noise is predominant at low frequencies, the downconverted signal is considerable affected by flicker noise, as it is located around zero frequency. Flicker noise, together with DC-offset, is a main issue in direct conversion receivers [38]. Most of the methods used for DC-offset cancelation are also useful for eliminating the 1/f noise components, especially those using mixers for low noise and high linearity [30]-[31],[39]-[40].

D. Even-order intermodulation distortion

While typical RF receivers only suffer from odd-order intermodulation effects, the even-order distortion is also a problem in direct conversion receivers, especially second-order intermodulation distortion (IMD2) [41],[42]. For example, let us consider the situation where two strong interferers, $cos(2\pi f_1 t)$ and $cos(2\pi f_2 t)$, separated in frequency an amount f_2-f_1=Δ less than the bandwidth of interest, are exposed to a second-order nonlinear behavior. In such a case, undesirable baseband spectral components are generated. These include a DC component and a baseband beat located at Δ Hz, within the downconversion band, which degrade the reception of the wanted signal. The solution leads to implement linear mixers, with higher rejection to second-order intermodulation, as well as the use of calibration techniques [42]-[45].

E. LO leakage

The leakage of the LO to the antenna and its subsequent radiation not only creates unwanted DC-offsets, but also interferences in the bands of other receivers. This problems arises because the LO is tuned exactly to the centre of the LNA and antenna pass-bands.

2.2.2 Zero-IF in software radio applications

The problems commented above have been the reason why homodyne receivers have not been as popular as heterodyne ones. Nevertheless, as different solutions have appeared in the last years, more and more zero-IF receivers for multimode applications have been proposed [46]-[47]. Moreover, new circuits and algorithmic techniques, along with higher levels of integration, have made zero-IF an acceptable choice for multi-standard reception. At present, SDRs based on the zero-IF architecture are capable of covering all cellular and WLAN communications, that is, up to 6GHz [48]-[50]. In fact, practically all commercially available SDRs for wireless communications are based on the zero-IF architecture. For example, *Epic Solutions*' *Matchstiq* [51] is a 2.2"x4.6"x0.9" reconfigurable zero-IF transceiver with CPU/FPGA processing, which covers the 0.3-3.8 GHz frequency range and supports up to 28 MHz channel bandwidths (4500 $). The *FUNcube Dongle* [52] (64-1700 MHz, 80 kHz quadrature sampling rate, 86x23x14 mm) uses an E4000 CMOS multiband tuner, which is based on a zero-IF architecture indeed. *Lime Microsystems* commercializes the LMS6002 [53], a fully integrated (9x9 mm) 0.375-4 GHz zero-IF transceiver with programmable channel bandwidth from 1.5 to 28 MHz.

The challenge for zero-IF SDRs is currently focused on the exploration of higher frequencies, such us millimetre waves, as the trend towards high data rate services demands. The limit is determined by the I-Q mod/demodulator devices, thereby many efforts are being done in order to reach such a challenge [54]. Moreover, the development of broandband tunable RF filters, and wide band amplifiers is also having intensive research [TOEEJ 2008].

2.3 LOW-IF

2.3.1 Fundamentals of low-IF

In a low-IF receiver, the RF signal is down-converted to an IF closed to zero, thereby the name near zero-IF or low-IF. The bock diagram of the low-IF receiver (Fig. 2.3) is similar to the zero-IF one, with the exception of low-pass filters, which are here substituted by band-pass filters. The final downconversion to baseband is performed in the digital domain [55].

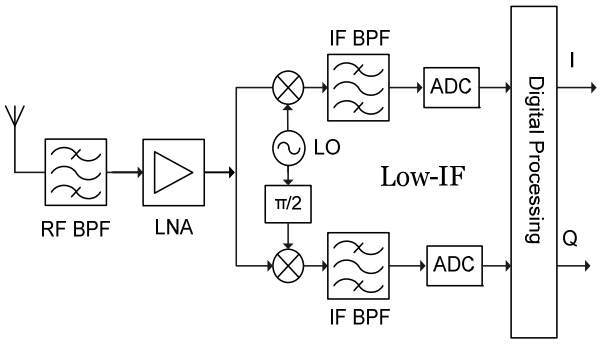

Fig. 2.3: Block diagram of a low-IF receiver.

Low-IF receiver combines the advantages of zero-IF and heterodyne receivers. On one hand, low-IF has zero-IF advantages such as low-cost, compact size, reconfigurability, and high level of integration. On the other hand, as IF is not located around DC, there are no DC-offset and flicker noise problems. However, the main drawback of the low-IF architecture is the image frequency. As the image frequency is located very closed to RF signal, no RF filters for image rejection can be used. Typical image suppression techniques consist in using image rejection architectures, such as Hartley [56] or Weaver [57]. However, I-Q imbalances cause interference that can not be removed in later stages and so directly decrease the image-reject capabilities of the front-end. For example, a relative voltage gain mismatch of 5% and a phase imbalance of 5º lead to an image rejection ratio (IRR) approximately equal to 26 dB. The fact is that, in practice, these architectures can hardly achieve an IRR above 40 dB. Digital signal processing can also be applied to eliminate the image components [58]-[60]. However, the key point is that very strict I-Q balance requirements are demanded for low-IF receivers, making difficult its implementation, especially for broadband applications. Furthermore, a low-IF receiver demands the double IF bandwidth compared with a zero-IF receiver, making the I-Q imbalance problem worse.

2.3.2 Low-IF in software radio applications

The number of publications regarding to low-IF SDRs are not as numerous as zero-IF SDRs. Although many proposals have been published, the image frequency and the strict I-Q balance requirements are problems which are not completely solved at the moment. Therefore, most of the manufacturers are going for zero-IF instead of low-IF to implement a SDR. However, there are some SDRs in the literature based on

a low-IF architecture [61]-[62]. Moreover, it is also usual to find SDRs which use both low-IF and zero-IF schemes [63]-[65].

2.4 SIX-PORT ARCHITECTURE

2.4.1 Fundamentals of six-port networks

The origin of the six-port network dates from the seventies, when it was introduced by Engen and Hoer to measure complex voltage ratios, as an alternative network analyzer [66]-[69]. According to the classical six-port theory, the reflection coefficient of a DUT (*device-under-test*) connected to one of its ports can be determined by means of a certain set of remote independent observations, when an excitation is introduced into one of the other ports [70],[71].

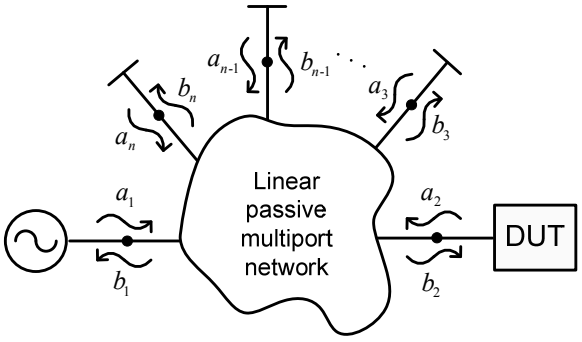

Fig. 2.4: Multiport network for the measurement of complex voltage ratios.

Let us consider the *n*-port network of Fig. 2.4, where the reflection coefficient of the DUT $\Gamma = a_2 / b_2$ wants to be determined. Incident and reflected waves can be related by means of the scattering parameters as follows:

$$b_j = \sum_{k=1}^{n} S_{jk} a_k \qquad j = 1,2,...,n \tag{2-1}$$

where S_{jk} are known complex parameters, and a_j, b_j are, respectively, the complex envelopes of the incident and reflected waves, which are unknown parameters. Therefore, there are *2n* unknowns.

Assuming that the reflection coefficients in the last *n-2* ports are known:

$$a_i = \Gamma_i \cdot b_i \qquad i = 3,...,n \tag{2-2}$$

by joining the expressions (2-1) and (2-2), and after algebraic manipulations, the next system of equations is obtained:

$$\begin{bmatrix} b_3 \\ ... \\ b_n \end{bmatrix} = \begin{bmatrix} \alpha_3 & \beta_3 \\ ... & ... \\ \alpha_n & \beta_n \end{bmatrix} \cdot \begin{bmatrix} a_2 \\ b_2 \end{bmatrix} \tag{2-3}$$

α_i and β_i are known complex constants, since they depend on S_{jk} and Γ_i. A system of *n-2* equations and two unknowns, a_2 and b_2, is obtained. Then two observations, for example b_3 and b_4, are sufficient to resolve the system of equations for a_2 and b_2, obtaining the reflection coefficient of the DUT $\Gamma = a_2 / b_2$. Take into account that any pair a_j and/or b_j could have been specified as unknowns in (2-3), instead of a_2 and b_2. The main problem is that, in practice, it is not an easy matter to measure the reflected waves b_i, being simpler to measure their powers:

$$P_i = \frac{1}{2}\left|b_i\right|^2 \tag{2-4}$$

Substituting (2-3) into (2-4), the next expression for the power of b_i is obtained:

$$\begin{aligned} P_i &= \frac{1}{2}\left|\alpha_i a_2 + \beta_i b_2\right|^2 = \frac{1}{2}\left(\alpha_i a_2 + \beta_i b_2\right)\cdot\left(\alpha_i a_2 + \beta_i b_2\right)^* = \\ &= \frac{1}{2}\left(\left|\alpha_i\right|^2\left|a_2\right|^2 + \left|\beta_i\right|^2\left|b_2\right|^2 + \alpha_i\beta_i^* a_2 b_2^* + \alpha_i^*\beta_i a_2^* b_2\right) \end{aligned} \tag{2-5}$$

(2-5) is linear with $\left|a_2\right|^2$, $\left|b_2\right|^2$, $a_2 b_2^*$ and $a_2^* b_2$. Hence, it is possible to determine a_2 and b_2 with four power readings, that is, *n=6*. These four powers and the remaining two ports (DUT and local oscillator, LO) are the reason for the name "six-port". The system of equations results in:

$$\begin{bmatrix} P_3 \\ P_4 \\ P_5 \\ P_6 \end{bmatrix} = \frac{1}{2} \begin{bmatrix} |\alpha_3|^2 & |\beta_3|^2 & \alpha_3\beta_3^* & \alpha_3^*\beta_3 \\ |\alpha_4|^2 & |\beta_4|^2 & \alpha_4\beta_4^* & \alpha_4^*\beta_4 \\ |\alpha_5|^2 & |\beta_5|^2 & \alpha_5\beta_5^* & \alpha_5^*\beta_5 \\ |\alpha_6|^2 & |\beta_6|^2 & \alpha_6\beta_6^* & \alpha_6^*\beta_6 \end{bmatrix} \cdot \begin{bmatrix} |a_2|^2 \\ |b_2|^2 \\ a_2b_2^* \\ a_2^*b_2 \end{bmatrix} = M \cdot \begin{bmatrix} |a_2|^2 \\ |b_2|^2 \\ a_2b_2^* \\ a_2^*b_2 \end{bmatrix} \tag{2-6}$$

which can be solved if M is not a singular matrix, i.e., $|M| \neq 0$. Under this condition, the previous system is solved as follows:

$$\begin{bmatrix} |a_2|^2 \\ |b_2|^2 \\ a_2b_2^* \\ a_2^*b_2 \end{bmatrix} = M^{-1} \cdot \begin{bmatrix} P_3 \\ P_4 \\ P_5 \\ P_6 \end{bmatrix} \tag{2-7}$$

where the complex constant parameters α_i and β_i have to be determined in advance using an appropriate calibration technique. It is worth to pointing out that determining $|a_2|^2$, $|b_2|^2$, $a_2b_2^*$ and $a_2^*b_2$ does not provide the absolute phases of a_2 and b_2. In effect, as $a_2b_2^*$ is the complex conjugate of $a_2^*b_2$, both quantities lead to the determination of $|a_2|\cdot|b_2|$, and $\arg(a_2) - \arg(b_2)$. With the help of $|a_2|^2$ and $|b_2|^2$, $|a_2|$ and $|b_2|$ can be calculated, but once again we have the term $\arg(a_2) - \arg(b_2)$. In practice, the habitual procedure consists of defining all the phases with respect to one reference port. In any case, the reflection coefficient $\Gamma = a_2 / b_2$ is completely defined by $|a_2|$, $|b_2|$ and $\arg(a_2) - \arg(b_2)$.

Moreover, $|a_2|^2$, $|b_2|^2$, $a_2b_2^*$ and $a_2^*b_2$ are related to each other by

$$|a_2|^2 \cdot |b_2|^2 = a_2b_2^* \cdot a_2^*b_2 \tag{2-8}$$

Consequently, (2-5) can be rewritten as:

$$P_i = \frac{1}{2}\left(|\alpha_i|^2|a_2|^2 + |\beta_i|^2|b_2|^2\right) + |\alpha_i|\cdot|\beta_i|\cdot|a_2|\cdot|b_2|\cos\left(\arg(\alpha_i) - \arg(\beta_i) + \arg(a_2) - \arg(b_2)\right) \tag{2-9}$$

reducing the problem to a system of three nonlinear equations and, therefore, to a five-port network. That means that multiport structures require at least three independent outputs to determine the reflection coefficient. However, the even nature of the cosine

function leads to two solutions for $\arg(a_2)-\arg(b_2)$. Thus, the problem does not have unique solution for a five-port network, which means less accuracy in the measurements and a more complicated calibration process for the determination of α_i and β_i [72]. This affirmation results evident from the six-port graphical interpretation, which will be presented below.

2.4.1.1 Graphical interpretation

It was shown that the power readings at the four detection ports of a six-port junction are:

$$P_i = \frac{1}{2}\left|\alpha_i a_2 + \beta_i b_2\right|^2 \qquad i = \{3,4,5,6\} \tag{2-10}$$

When operating as an alternative network analyzer, the six-port reflectometer is usually designed in such a way that the response of one of the power detectors is proportional to $|b_2|^2$ [69]. It responds to a double purpose. On one hand, $|b_2|$ represents directly one of the measurements of interests. On the other hand, monitoring $|b_2|$ is useful to correct possible power instabilities in the signal source, and to ensure that the power levels at the output ports are maintained at some optimum values as the frequency is varied. Then, the six-port comprises a reference port. The port chosen for this role will be number 3, that is, $\alpha_3 = 0$ and

$$P_3 = \left|\beta_3\right|^2 \cdot \left|b_2\right|^2 \tag{2-11}$$

Thus, the powers of the remaining ports can be normalized by P_3, leading to:

$$\frac{P_i}{P_3} = \frac{\left|\alpha_i a_2 + \beta_i b_2\right|^2}{\left|\beta_3\right|^2 \cdot \left|b_2\right|^2}, \qquad i = \{4,5,6\} \tag{2-12}$$

Defining the so-called q_i-points as [69]:

$$q_i = -\frac{\beta_i}{\alpha_i} \tag{2-13}$$

and by expressing a_2 as $b_2 \cdot \Gamma$, (2-12) can be rewritten in the form:

$$\frac{P_i}{P_3} = \frac{|\alpha_3|^2}{|\beta_i|^2} |\Gamma - q_i|^2, \qquad i = \{4,5,6\} \tag{2-14}$$

The above expression represents three circles, whose centres are the q_i-points, and their radius are

$$R_i = |\Gamma - q_i| = \sqrt{\frac{P_i}{P_3}} \frac{|\beta_3|}{|\alpha_i|}, \qquad i = \{4,5,6\} \tag{2-15}$$

Then, Γ is given by the intersection of these three circles, as it can be seen in Fig. 2.5. Six-port reflectometers are thus characterized by their q_i-points, which can be directly calculated from the six-port scattering parameters:

$$q_i = \frac{s_{i1}}{s_{22}s_{i1} - s_{i2}s_{21}} \tag{2-16}$$

The determination of Γ could be also done by the intersection of only two circles, which would correspond to a five-port network. It is worth highlighting that in such a case, represented in Fig. 2.6, there are two possible solutions for Γ, as the two circles intersect in a pair of points. When the DUT is a passive device, Γ falls within the unit circle. Therefore, if one of the two points is outside the unit circle, which is the situation in Fig. 2.6, it is possible to choose between the two solutions.

In practice, due to measurement errors and detector noises, the circles do not intersect in the right position. In the case of six-port networks, their intersection will comprise a triangular area, where Γ will be included. As for five-port junctions, obviously, less accuracy in the determination of Γ is expected. In fact, there is a high sensitivity to errors in the direction perpendicular to the line between q_3 and q_5, being less in the parallel direction. In particular, if Γ is located around the perimeter of the unit circle, one can assume a considerable variation in the sensitivity to errors.

Six-port reflectometers can be also designed without the requirement of α_3=0. In such a case, the graphical solution leads again to the intersection of three circles (two in a five-port junction), but with different centres and radius [71]. In effect, the normalized powers would be:

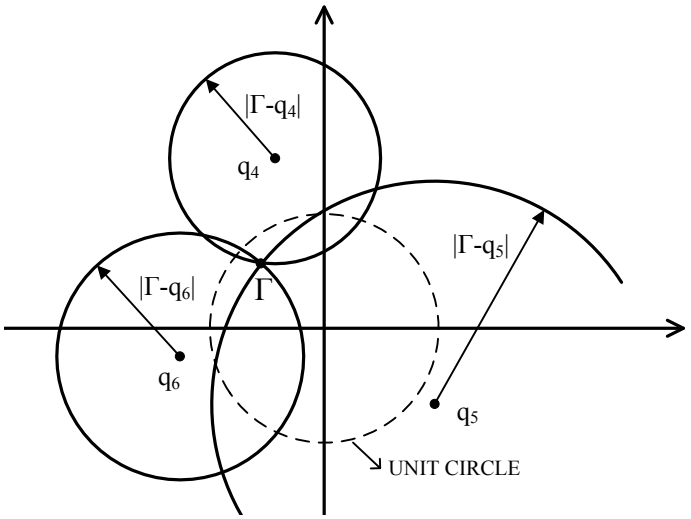

Fig. 2.5: Determination of Γ from the intersection of three circles.

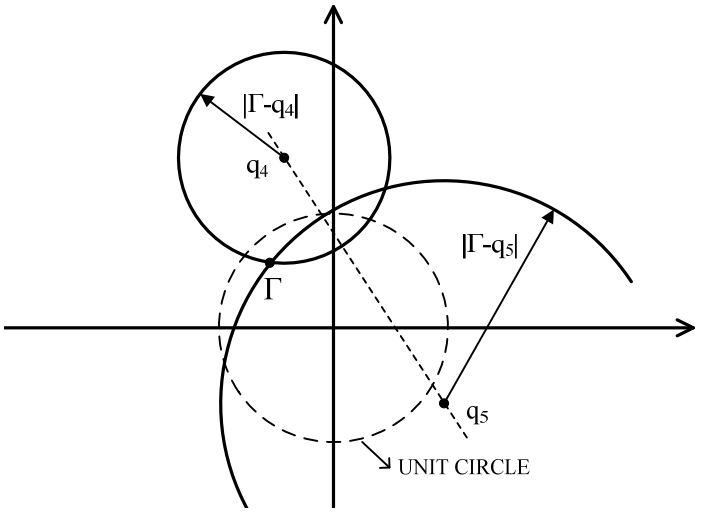

Fig. 2.6: Determination of Γ from the intersection of two circles.

$$\frac{P_i}{P_3}=\frac{\left|\alpha_i a_2+\beta_i b_2\right|^2}{\left|\alpha_3 a_2+\beta_3 b_2\right|^2}=\frac{\left|\alpha_i\right|^2}{\left|\alpha_3\right|^2}\frac{\left|\Gamma-q_i\right|^2}{\left|\Gamma-q_3\right|^2},\qquad i=\{4,5,6\} \tag{2-17}$$

The above equation is a circle equation indeed, so it can alternatively be written as follows:

$$R_i^2=\left|\Gamma-Q_i\right|^2,\qquad i=\{4,5,6\} \tag{2-18}$$

The centre and radius of the circles are now:

$$Q_i = \frac{\frac{k_i}{q_3^*}|q_3|^2 - \mu_i^2 q_i}{k_i - \mu_i^2} \tag{2-19}$$

$$R_i^2 = \frac{k_i \left| \frac{q_i \mu_i}{|q_3|^2} - \frac{\mu_i}{q_3} \right|^2}{\left(\mu_i^2 - k_i\right)^2} |q_3|^4 \tag{2-20}$$

being $k_i = \frac{P_i}{P_3}$, and $\mu_i = \frac{|\alpha_i|}{|\alpha_3|}$.

Notice that the central position of the circles, Q_i, are now functions not only of the six-port junction, but also of the power readings in the Γ plane. Moreover, these power readings are directly related to the load connected to the measuring port 2. Then, a six-port design with α_3=0 is advantageous in order to eliminate the dependence of the Q_i-points on the power readings and, therefore, on the load.

2.4.1.2 Design considerations on six-port junctions

The design criterion of a six-port junction consists of achieving a good distribution of the q_i-points in the Γ plane [69]. By simple inspection of Fig. 2.5, it is evident that an ill-conditioned numerical situation results if $|q_i|$ is either too large or too small. Thus, based on symmetrical configurations, the optimal position of the q_i-points should be located at the vertices of an equilateral triangle whose centre is at the origin. This calls for $|q_4|=|q_5|=|q_6|$, while the relative phase separations between q_i are 120º. The optimum choice of $|q_i|$ may be expected to lie in the range 0.5-1.5. Nevertheless, the six-port network can provide good results even when the ratios of the magnitudes of q_i are greater than 4, and their arguments differ an amount smaller than 25º [73],[74]. In practice, most of the six-port junctions are quasi-optimal design approaches. In general, the closer the magnitudes of q_i, and the larger the differences between the arguments of q_i, the better will be the performance of the circuit.

Six-port junction topologies are based on the interconnection of several passive four- and/or three-port networks, such as couplers and power dividers. Several examples of six-port networks are presented in Fig. 2.7. In the existing art, the

implementation of a broadband optimal six-port circuit can not be accomplished. In effect, a 120º phase shift is achieved with narrowband circuits, such as symmetrical five-port rings [75]—Fig. 2.7 (b)— or phase shifters based on delay lines [76]-[77]. On the contrary, a quasi-optimal six-port design can be realized using only 3dB hybrids and/or power dividers, making ultra-broadband six-port designs feasible [78]-[79]. For example, the topology represented in Fig. 2.7 (c) is the typical six-port configuration [13],[16], where a broadband 90º phase shift can be achieved using three 3dB hybrids and one Wilkinson divider.

A variety of different technologies have been used for six-port implementation. Several six-port network implementations are presented in Fig. 2.8-Fig. 2.12. Along with conventional MIC (*Microwave Integrated Circuits*) technology, six-port networks can be implemented, for example, in SIW (*Substrate Integrated Waveguide*), MMIC (*Monolithic Microwave Integrated Circuit*), or multilayer substrate technologies.

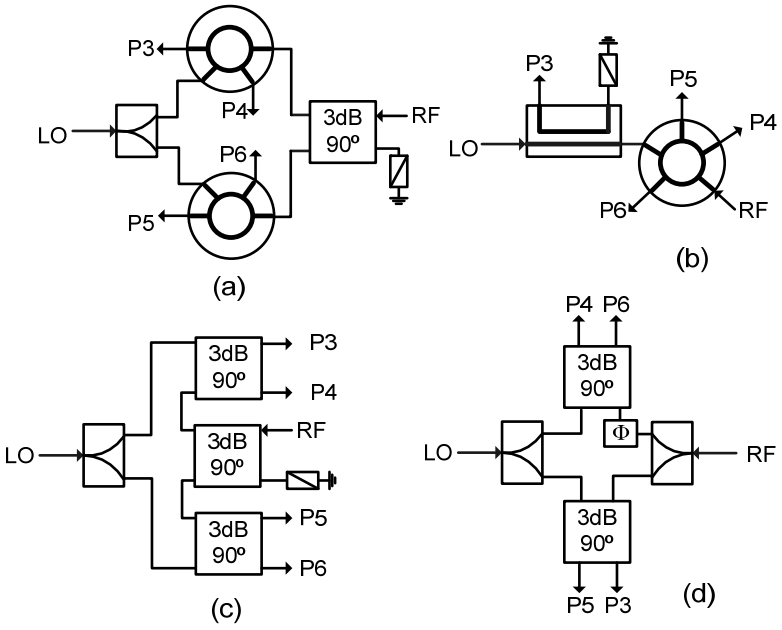

Fig. 2.7: Examples of six-port junction topologies.

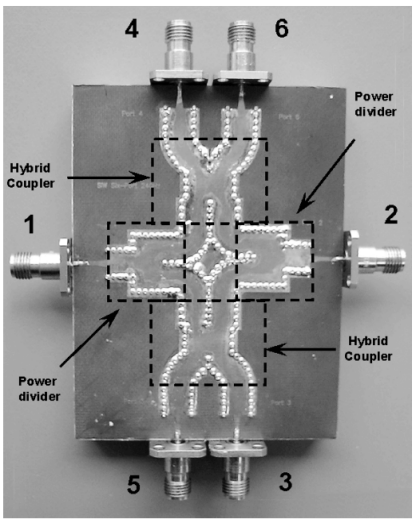

Fig. 2.8 22-26 GHz six-port network in SIW technology (*© 2006 IEEE* [17]).

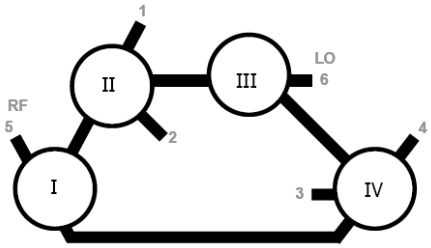

Fig. 2.9 60 GHz six-port network in microstrip technology (*© 2007 IEEE* [19]).

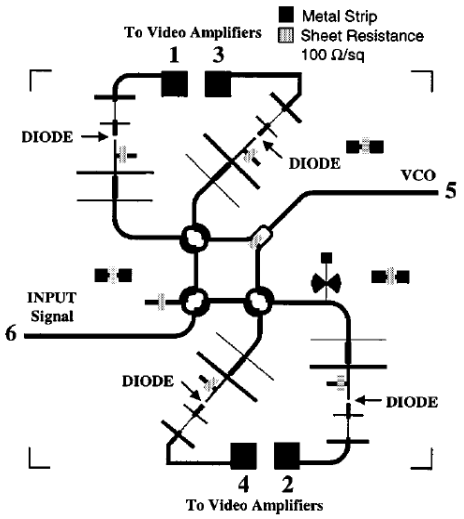

Fig. 2.10 23-31 GHz six-port network in microstrip technology (*© 2001 IEEE* [80]).

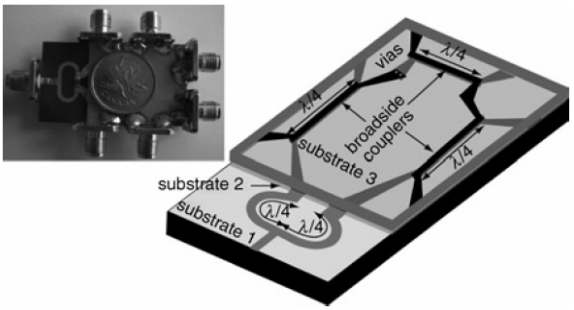

Fig. 2.11 Multilayer 3-5 GHz six-port network (*© 2007 IEEE* [81]).

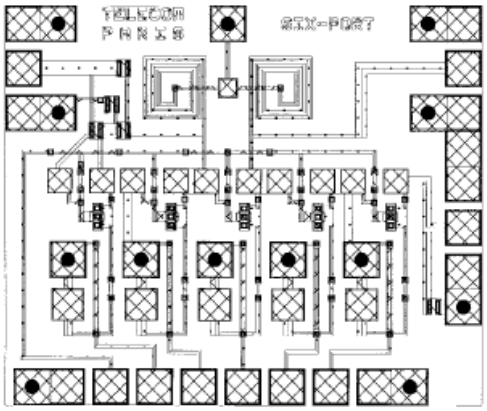

Fig. 2.12 1.3-3 GHz six-port network in MMIC technology (*© 1997 IEEE* [82]).

2.4.2 Operation principle of six-port receivers

Although the concept of six-port network was introduced in the seventies, it was twenty years later when it was firstly used as a communication receiver [83]. The principle of operation of the six-port receiver is based on the measurement of four independent powers, when the LO and RF signals are introduced into the remaining two ports [70]. The original I/Q components can be regenerated from these four power observations and some calibration constants, depending on system response. The block diagram of a six-port receiver is presented in Fig. 2.13. It is composed of a linear and passive six-port junction, where the RF and LO signals are combined using different relative phases. A square law device and a low-pass filter are located at each output port.

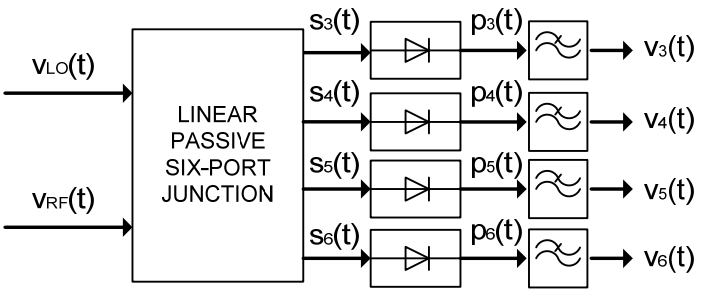

Fig. 2.13: Block diagram of a six-port receiver

In order to understand the six-port receiver behaviour, we will use the pass-band representation of the next two input signals:

$$v_{LO}(t) = V_{LO}\cos(2\pi f_{LO}t) \tag{2-21}$$

$$v_{RF}(t) = I(t)\cos(2\pi f_{RF}t) - Q(t)\sin(2\pi f_{RF}t) \tag{2-22}$$

being V_{LO} the LO amplitude, f_{LO} the LO frequency, and f_{RF} the frequency of the modulated useful signal. $z(t) = I(t) + jQ(t)$ represents the complex envelope of the modulated useful signal, that is:

$$v_{RF}(t) = \Re e\left\{ z(t)\cdot e^{j2\pi f_{RF}t} \right\} \tag{2-23}$$

The six-port junction is a linear and passive circuit, therefore, the output signals are linear combinations of the input signals

$$s_i(t) = A_i V_{LO}\cos(2\pi f_{LO}t + \varphi_i) + B_i[I(t)\cos(2\pi f_{RF}t + \psi_i) - Q(t)\sin(2\pi f_{RF}t + \psi_i)] \tag{2-24}$$

with i={3,…,6}. A_i and φ_i are, respectively, the attenuation and phase shift of the six-port circuit from the LO port, while B_i and ψ_i correspond to the RF port. The transfer characteristic of the power detector can be expressed by a Taylor series expansion

$$f[x(t)] = K_1[x(t)] + K_2[x(t)]^2 + K_3[x(t)]^3 + \ldots \tag{2-25}$$

where K_n are real constant values depending on the power detector characteristics. The expressions of detectors outputs signals can be obtained by substituting (2-24) into (2-25):

$$
\begin{aligned}
(t) = {} & \frac{K_{2i}}{2}\left\{A_i^2 V_{LO}^2 + B_i^2\left(I^2(t)+Q^2(t)\right)\right\} + \quad \text{rectified wave/self-mixing} \\
& + K_{1i}\left\{A_i V_{LO}\cos\left(2\pi f_{LO}t+\varphi_i\right) + B_i I(t)\cos\left(2\pi f_{RF}t+\psi_i\right) + B_i Q(t)\sin\left(2\pi f_{RF}t+\psi_i\right)\right\} \text{ fundamental wave} \\
& + K_{2i}A_i\cdot V_{LO}\cdot B_i\left\{I(t)\cos\left(2\pi(f_{LO}-f_{RF})t+\varphi_i-\psi_i\right) + Q(t)\sin\left(2\pi(f_{LO}-f_{RF})t+\varphi_i-\psi_i\right)\right\} \text{ difference frequency} \\
& + K_{2i}A_i\cdot V_{LO}\cdot B_i\left\{I(t)\cos\left(2\pi(f_{LO}+f_{RF})t+\varphi_i-\psi_i\right) - Q(t)\sin\left(2\pi(f_{LO}+f_{RF})t+\varphi_i-\psi_i\right)\right\} \text{ sum frequency} \\
& + \ldots \quad \text{higher order harmonics and intermodulation products}
\end{aligned}
\tag{2-26}
$$

The typical six-port operation mode corresponds to a direct frequency conversion scheme, where f_{LO} is equal to f_{RF}. Consequently, after ideal low-pass filtering the next signal is obtained:

$$v_i(t) = \frac{K_{2i}}{2}A_i^2V_{LO}^2 + \frac{K_{2i}}{2}B_i^2[I^2(t)+Q^2(t)] + K_{2i}V_{LO}A_iB_i\left(I(t)\cos\Phi_i + Q(t)\sin\Phi_i\right) + IMP_{even} \tag{2-27}$$

being:

$$\Phi_i = \varphi_i - \psi_i \tag{2-28}$$

IMP_{even} represents the even-order intermodulation products mf_{LO}-mf_{RF}, with $m>1$. Even order intermodulation products are the most important in direct conversion receivers, as they are located in baseband. In the case of $K_{ni} \approx 0$ for $n>2$, the even-order intermodulation products can be neglected, resulting in:

$$v_i(t) = \frac{K_{2i}}{2}A_i^2V_{LO}^2 + \frac{K_{2i}}{2}B_i^2[I^2(t)+Q^2(t)] + K_{2i}V_{LO}A_iB_i\left(I(t)\cos\Phi_i + Q(t)\sin\Phi_i\right) \tag{2-29}$$

Each output signal $v_i(t)$ contains three terms: the self-mixing of the LO, $K_{2i}/2\cdot A_i^2\cdot V_{LO}^2$, which is a DC component; the self-mixing of the modulated signal, $K_{2i}/2\cdot B_i^2\cdot[I^2(t)+Q^2(t)]$, which comprises a DC component and a time variant component; and the wanted baseband signal components, $K_{2i}\cdot V_{LO}\cdot A_i\cdot B_i\cdot[I(t)\cos\Phi_i+Q(t)\sin\Phi_i]$. It is worth pointing out that $v_i(t)$ are baseband signals, therefore, a frequency conversion takes place without using I-Q demodulators.

For the four output signals, the following system of equations can be written:

$$\begin{bmatrix} v_3(t) \\ v_4(t) \\ v_5(t) \\ v_6(t) \end{bmatrix} = \begin{bmatrix} G_3 & R_3 & S_3\cos\Phi_3 & S_3\sin\Phi_3 \\ G_4 & R_4 & S_4\cos\Phi_4 & S_4\sin\Phi_4 \\ G_5 & R_5 & S_5\cos\Phi_5 & S_5\sin\Phi_5 \\ G_6 & R_6 & S_6\cos\Phi_6 & S_6\sin\Phi_6 \end{bmatrix} \cdot \begin{bmatrix} V_{LO}^2 \\ I^2(t)+Q^2(t) \\ I(t) \\ Q(t) \end{bmatrix} = D_T \cdot \begin{bmatrix} V_{LO}^2 \\ I^2(t)+Q^2(t) \\ I(t) \\ Q(t) \end{bmatrix} \tag{2-30}$$

where:

$$G_i = \frac{K_{2i}}{2} A_i^2 \tag{2-31}$$

$$R_i = \frac{K_{2i}}{2} B_i^2 \tag{2-32}$$

$$S_i = K_{2i} A_i B_i V_{LO} \tag{2-33}$$

The previous system can be solved by means of a matrix inversion,

$$\begin{bmatrix} V_{LO}^2 \\ I^2(t)+Q^2(t) \\ I(t) \\ Q(t) \end{bmatrix} = D_T^{-1} \cdot \begin{bmatrix} v_3(t) \\ v_4(t) \\ v_5(t) \\ v_6(t) \end{bmatrix} = \begin{bmatrix} g_3 & g_4 & g_5 & g_6 \\ t_3 & t_4 & t_5 & t_6 \\ h_3 & h_4 & h_5 & h_6 \\ n_3 & n_4 & n_5 & n_6 \end{bmatrix} \cdot \begin{bmatrix} v_3(t) \\ v_4(t) \\ v_5(t) \\ v_6(t) \end{bmatrix} \tag{2-34}$$

leading to the general demodulation equations in six-port structures:

$$I(t) = \sum_{i=3}^{6} h_i \cdot v_i(t) \tag{2-35}$$

$$Q(t) = \sum_{i=3}^{6} n_i \cdot v_i(t) \tag{2-36}$$

Consequently, the original I/Q signals can be regenerated from the four output signals and eight constant parameters depending on system response. In fact, h_i and n_i depend on the six-port junction parameters α_i and β_i, the detector parameter K_{2i}, the low-pass filter response, etc. Therefore, a six-port calibration process is required to calculate them. That is the reason why h_i and n_i are commonly known as calibration constants.

The equivalence with classical six-port theory arises clear when the complex envelopes of the input signals $v_{LO}(t)$ and $v_{RF}(t)$ are considered:

$$\overline{v_{LO}} = V_{LO} \cdot \exp\left(j\varphi_{LO}\right) \tag{2-37}$$

$$\overline{v_{RF}} = z(t) = I(t) + jQ(t) \tag{2-38}$$

In this case, (2-29) can be rewritten as follows:

$$v_i(t) = \frac{K_{2i}}{2}[A_i^2 \,|\overline{v}_{LO}|^2 + B_i^2 \,|\overline{v}_{RF}|^2 + A_i e^{j\varphi_i} B_i e^{-j\varphi_i} \overline{v}_{LO} \overline{v}_{RF}^{\,*} + A_i e^{-j\varphi_i} B_i e^{j\varphi_i} \overline{v}_{LO}^{\,*} \overline{v}_{RF}] \tag{2-39}$$

Notice that the above equation coincides with the expression (2-5), excepting for the correction factor K_{2i}. Remind from the classical six-port theory that any two variables a_j and/or b_j can be specified as the two unknowns of the system (2-3). In this case, and following the nomenclature of Fig. 2.4, the two unknowns are a_1 and a_2, corresponding to $\overline{v_{LO}}$ and $\overline{v_{RF}}$, and the four power observations are P_3, P_4, P_5 and P_6.

Let us consider now the case of a five-port receiver. When the LO power level is known, which is reasonable in a receiver design, it can be removed from the unknown parameters in system (2-30). Hence, the number of equations can be reduced from four to three as follows:

$$\begin{bmatrix} v_3(t) - G_3 V_{LO}^2 \\ v_4(t) - G_4 V_{LO}^2 \\ v_5(t) - G_5 V_{LO}^2 \end{bmatrix} = \begin{bmatrix} R_3 & S_3 \cos\Phi_3 & S_3 \sin\Phi_3 \\ R_4 & S_4 \cos\Phi_4 & S_4 \sin\Phi_4 \\ R_5 & S_5 \cos\Phi_5 & S_5 \sin\Phi_5 \end{bmatrix} \cdot \begin{bmatrix} I^2(t) + Q^2(t) \\ I(t) \\ Q(t) \end{bmatrix} \tag{2-40}$$

The system solution leads to:

$$\begin{bmatrix} I^2(t) + Q^2(t) \\ I(t) \\ Q(t) \end{bmatrix} = D^{-1} \cdot \begin{bmatrix} v_3(t) \\ v_4(t) \\ v_5(t) \end{bmatrix} - D^{-1} \cdot V_{LO}^2 \begin{bmatrix} G_3 \\ G_4 \\ G_5 \end{bmatrix} \tag{2-41}$$

where:

$$D^{-1} = \begin{bmatrix} R_3 & S_3\cos\Phi_3 & S_3\sin\Phi_3 \\ R_4 & S_4\cos\Phi_4 & S_4\sin\Phi_4 \\ R_5 & S_5\cos\Phi_5 & S_5\sin\Phi_5 \end{bmatrix}^{-1} = \begin{bmatrix} r_n & s_n & t_n \\ r_I & s_I & t_I \\ r_Q & s_Q & t_Q \end{bmatrix} \tag{2-42}$$

Therefore, the demodulation equations will be:

$$I(t) = r_I\hat{v}_3(t) + s_I\hat{v}_4(t) + t_I\hat{v}_5(t) - c_I \tag{2-43}$$

$$Q(t) = r_Q\hat{v}_3(t) + s_Q\hat{v}_4(t) + t_Q\hat{v}_5(t) - c_Q \tag{2-44}$$

with:

$$c_I = \left(r_I G_3 + s_I G_4 + t_I G_5\right)V_{LO}^2 \tag{2-45}$$

$$c_Q = \left(r_Q G_3 + s_Q G_4 + t_Q G_5\right)V_{LO}^2 \tag{2-46}$$

However, even if the LO power is unknown, or so unstable that it can not be treated as a constant, the equation reduction can be done anyway by applying DC cancellation methods, as the LO self-mixing is a DC term. This is indeed the habitual procedure in five-port receivers, either by analogical or digital methods. The overall DC contribution in $v_i(t)$ comes from the self-mixing of the LO, and the self-mixing of the modulated signal. The self-mixing of the modulated signal comprises a DC component, dc_i, and a time variant component, $n(t)$, that is:

$$\frac{K_{2i}}{2}B_i^2[I^2(t) + Q^2(t)] = dc_i + R_i \cdot n(t) \tag{2-47}$$

Then, (2-29) can be rewritten as follows:

$$v_i(t) = V_{dc,i} + R_i \cdot n(t) + S_i\left(I(t)\cos\Phi_i + Q(t)\sin\Phi_i\right) \tag{2-48}$$

where $V_{dc,i} = G_i \cdot V_{LO}^2 + dc_i$ represents the DC-offset of the output voltages. After DC-offset cancellation, the system of equations reduces to:

$$\begin{bmatrix} \hat{v}_3(t) \\ \hat{v}_4(t) \\ \hat{v}_5(t) \end{bmatrix} = \begin{bmatrix} R_3 & S_3\cos\Phi_3 & S_3\sin\Phi_3 \\ R_4 & S_4\cos\Phi_4 & S_4\sin\Phi_4 \\ R_5 & S_5\cos\Phi_5 & S_5\sin\Phi_5 \end{bmatrix} \cdot \begin{bmatrix} n(t) \\ I(t) \\ Q(t) \end{bmatrix} \tag{2-49}$$

where $\hat{v}_i(t) = v_i(t) - V_{dc,i}$. Therefore, in a five-port receiver the original I/Q signals can be recovered from the three output signals and six calibration constants:

$$I(t) = r_I \hat{v}_3(t) + s_I \hat{v}_4(t) + t_I \hat{v}_5(t) \tag{2-50}$$

$$Q(t) = r_Q \hat{v}_3(t) + s_Q \hat{v}_4(t) + t_Q \hat{v}_5(t) \tag{2-51}$$

The equivalence with the classical five-port theory is also straightforward, just selecting the next expression for the RF input signal:

$$v_{RF}(t) = V_{RF}(t)\cos\left(2\pi f_{RF} t + \varphi_{RF}(t)\right) \tag{2-52}$$

In this case, (2-29) can be rewritten as follows:

$$v_i(t) = \frac{K_{2i}}{2}[A_i^2 V_{LO}^2 + B_i^2 V_{RF}^2(t)] + K_{2i} A_i^2 B_i^2 V_{LO} V_{RF}(t)\cos\left(\varphi_i - \psi_i + \varphi_{RF}(t)\right) \tag{2-53}$$

which coincides with the classical five-port theory equation (2-9), excepting for the factor K_{2i}.

2.4.3 Advantages and drawbacks

Typically, six-port architecture responds to a direct conversion scheme, although it can operate as both homodyne and heterodyne receiver [70]. This means that it possess typical advantages of zero-IF such as no image frequency, no bulky IF components, low cost, flexibility, reconfigurability, etc. Furthermore, since it consists of a linear passive network and some power detectors, frequency conversion takes place without using an I-Q mixer. Therefore, it has the zero-IF advantages without I-Q mixer problems.

The main characteristic of the six-port architecture is its extremely large bandwidth, which involves multi-band and multi-mode capabilities. Moreover, six-port networks can operate at very high frequencies, such us millimeter-wave

frequencies. Consequently, it is a good solution for large relative-bandwidth applications and high data rate services. Six-port radios were estimated to perform data rates of at least 200 Mbps in 2008 [14], and recent publications have demonstrated the six-port gigabit demodulation capability [21].

One point that is worth emphasizing is that six-port receivers require lower LO power levels than conventional zero-IF receivers. This feature not only entails less power consumption, but also other important advantages. On one hand, better isolations can be achieved. On the other hand, the LO self-mixing problem, which is fundamental in direct conversion schemes, can be reduced.

Along with conventional MIC technology, six-port networks can be implemented in MMIC or multilayer substrate technologies. Reduced dimensions and low-cost high volume productions can then be obtained. The higher the frequency, the smaller the passive circuit and the easier the integration in a MMIC design. But for operating frequencies in the lower gigahertz region, a broadband design in conventional MIC technology leads to large dimensions, which could be prohibitive, for example, for mobile communication applications.

All theses characteristics make six-port architecture to be considered a good candidate to implement a SDR. However, some drawbacks have to be taken into account. Firstly, a calibration process is needed for the regeneration of the original signal. The quality of the demodulated signal depends on the accuracy of the calibration method. Therefore, this is a key factor in six-port receivers. Secondly, more baseband outputs are needed, thereby more low-pass filters, video amplifiers, ADCs, etc.). Finally, the sensitivity and dynamic range of the system are determined by the detectors characteristics. As for the dynamic range, it is related to the region where the detectors behave as square law devices. Regarding to the sensitivity, it is a trade-off to video bandwidth and input detector matching [84]. The problem is that sensitivity, video bandwidth, and dynamic range are competitive parameters in a detector design. In fact, the main limitation of multi-port architectures is that they do not present good behaviour as for dynamic range, compared with heterodyne and conventional homodyne receivers. And this is a key point in a SDR implementation.

2.4.4 Calibration methods and I-Q regeneration

The aim of the six-port calibration is to determine the calibration constants and, along with the four/three power observation, to regenerate the I-Q components of the original signal. There are two types of I-Q regeneration: analog regeneration, and digital regeneration.

It is possible to analogically recover original I-Q components, provided that the six-port junction parameters are properly selected. In conventional six-port structures –see Fig. 2.7 (c) –, the phase shifts between the LO and RF signals are selected multiples of π/2, while the amplitudes are selected equal. It means that, ideally: $\Phi_3=0$, $\Phi_4=\pi$, $\Phi_5=\pi/2$, $\Phi_6=-\pi/2$; $G_3=G_4=G_5=G_6=G$; $R_3=R_4=R_5=R_6=R$; and $S_3=S_4=S_5=S_6=S$. In such conditions, the system of equations (2-30) results in:

$$v_3(t) = G \cdot V_{LO}^2 + R \cdot \left(I^2(t) + Q^2(t) \right) + S \cdot I(t) \tag{2-54}$$

$$v_4(t) = G \cdot V_{LO}^2 + R \cdot \left(I^2(t) + Q^2(t) \right) - S \cdot I(t) \tag{2-55}$$

$$v_5(t) = G \cdot V_{LO}^2 + R \cdot \left(I^2(t) + Q^2(t) \right) + S \cdot Q(t) \tag{2-56}$$

$$v_6(t) = G \cdot V_{LO}^2 + R \cdot \left(I^2(t) + Q^2(t) \right) - S \cdot Q(t) \tag{2-57}$$

By inspection, it can be found that I(t) and Q(t) can be easily obtained as follows:

$$I(t) = \frac{v_3(t) - v_4(t)}{2S} \tag{2-58}$$

$$Q(t) = \frac{v_5(t) - v_6(t)}{2S} \tag{2-59}$$

Therefore, the reconstruction can be done in the analog domain by feeding each pair to a differential amplifier, as shown in Fig. 2.14. The analog I-Q reconstruction has two clear advantages. The first advantage is that the IQ signals can be reconstructed by a simple analog circuit. The second one is that two baseband branches are eliminated and, consequently, two low-pass filters, two video amplifiers, two ADCs, etc. Nevertheless, the analog regeneration has its limitations. On one

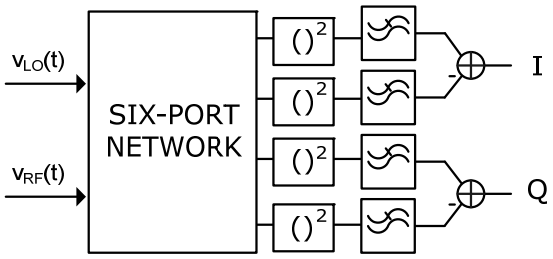

Fig. 2.14: Six-port receiver with analog I-Q regeneration.

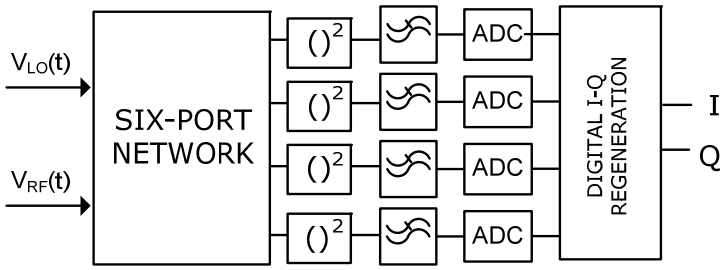

Fig. 2.15: Six-port receiver with digital I-Q regeneration.

hand, the quality of the demodulated signal strongly depends on hardware imbalances and tolerances, since a broadband device without impairments is not realizable in practice. On the other hand, a perfect cancellation of the rectified wave component is required.

In the digital I-Q regeneration, the six(five)-port receiver output signals are digitalized by means of an ADC, as represented in Fig. 2.15. Original I-Q components are then recovered in the digital domain, from the four/three power readings and the calibration constants, which have to be calculated in advance. It is advisable to previously eliminate DC components, since they can saturate next stages. Moreover, in a direct conversion receiver DC-offsets can corrupt the downconverted signal, thus it is convenient to eliminate it one again in digital domain, to achieve a more accurate cancellation. Digital I-Q regeneration enables calibrating the complete front-end and compensating circuit imperfections. The disadvantage of digital reconstruction is the increased number of hardware components and higher power consumption. For most microwave applications, this drawback is acceptable because calibration of the front-end is highly recommended. This option has certainly more sense in a SDR scenario.

It remains to be seen how the six-port calibration is carried out. First six-port calibration methods were based on precalibrated or physical calibration procedures, consisting on measuring the system using several external physical standards terminals [85]-[89]. Nevertheless, this kind of procedures is impractical for a wireless receiver or a SDR, owing to their lack of dynamism and flexibility. In addition, they are subject to measurement errors, component mismatches, tolerances, thermal drifts, etc.

Real-time calibration methods are more suitable, as they can be automatically performed while the system is operating. A reference publication about automatic six-port calibration is the dual-tone calibration method presented by Li et.al. in [90]. This method is based on the use of radio signals for the six-port calibration, instead of physical terminations. The classical real-time auto-calibration method, simplifying the previous one, was proposed by Xu and Bosisio in [91]. It is based on the use of a known training sequence at the beginning of each burst to auto-calibrate the system. The simplification of this method for five-port calibration is presented in [92]. Training sequence based calibration methods are suitable for SDR, due to its dynamic, versatile and robust features. Moreover, they can adapt to the signal and to the state of the system at every moment, eliminating the problems of tolerances, component drifts, and mismatches. This is the calibration method that will be used as reference in the present thesis. Hence we will explain it in more detail next.

2.4.4.1 Auto-calibration method based on training sequence

Well known auto-calibration techniques based on training sequences have been successfully applied to the calibration of six(five)-port receivers [91]-[92]. A known training sequence at the beginning of each burst is used to auto-calibrate the system. Let us consider a training sequence of M symbols at the RF input port. In such a case, demodulation equations (2-35) and (2-36) can be written as:

$$\begin{bmatrix} I(1) \\ \vdots \\ I(M) \end{bmatrix} = \begin{bmatrix} v_1(1) & v_2(1) & v_3(1) & v_4(1) \\ \vdots & \vdots & \vdots & \vdots \\ v_1(M) & v_2(M) & v_3(M) & v_4(M) \end{bmatrix} \cdot \begin{bmatrix} h_1 \\ h_2 \\ h_3 \\ h_4 \end{bmatrix} = V \cdot \begin{bmatrix} h_1 \\ h_2 \\ h_3 \\ h_4 \end{bmatrix} \tag{2-60}$$

$$\begin{bmatrix} Q(1) \\ \vdots \\ Q(M) \end{bmatrix} = \begin{bmatrix} v_1(1) & v_2(1) & v_3(1) & v_4(1) \\ \vdots & \vdots & \vdots & \vdots \\ v_1(M) & v_2(M) & v_3(M) & v_4(M) \end{bmatrix} \cdot \begin{bmatrix} n_1 \\ n_2 \\ n_3 \\ n_4 \end{bmatrix} = V \cdot \begin{bmatrix} n_1 \\ n_2 \\ n_3 \\ n_4 \end{bmatrix} \tag{2-61}$$

where $\tilde{v}_i(t)$ are the output signals of the six-port port receiver. The calibration constants are determined using a deterministic least mean square (LMS) algorithm as follows:

$$\begin{bmatrix} h_1 \\ h_2 \\ h_3 \\ h_4 \end{bmatrix} = \left(V^T \cdot V\right)^{-1} \cdot V^T \cdot \begin{bmatrix} I(1) \\ \vdots \\ I(M) \end{bmatrix} \tag{2-62}$$

$$\begin{bmatrix} n_1 \\ n_2 \\ n_3 \\ n_4 \end{bmatrix} = \left(V^T \cdot V\right)^{-1} \cdot V^T \cdot \begin{bmatrix} Q(1) \\ \vdots \\ Q(M) \end{bmatrix} \tag{2-63}$$

I-Q components of the data sequence, received after the training sequence, are recovered applying the calculated eight calibration constants in (2-35)-(2-36). This adaptive technique does not need high computational complexity and can be easily implemented in a DSP. Obviously, the method is extensible to any multi-port receiver. In the case of a five-port receiver [92], the average values of the output signals are previously subtracted, which is also advantageous for DC-offset rejection. Then V reduces to an Mx3 matrix instead of Mx4, and six calibration constants would be obtained by solving the system. Previous DC-offset cancelation can be also applied in the case of a six-port receiver calibration, without loss of generality.

2.4.5 Six-port in software radio applications

Since the six-port network was firstly used as a communication receiver in 1994 [83], this promising architecture has been used for many applications: radar systems [93]-[94], direction of arrival estimation [95]-[96], UWB (Ultra-Wide-Band) [14],[97], MIMO (Multiple Input Multiple Output) systems [98], etc. But it is especially interesting its possibilities for SDR implementation, due to the advantages

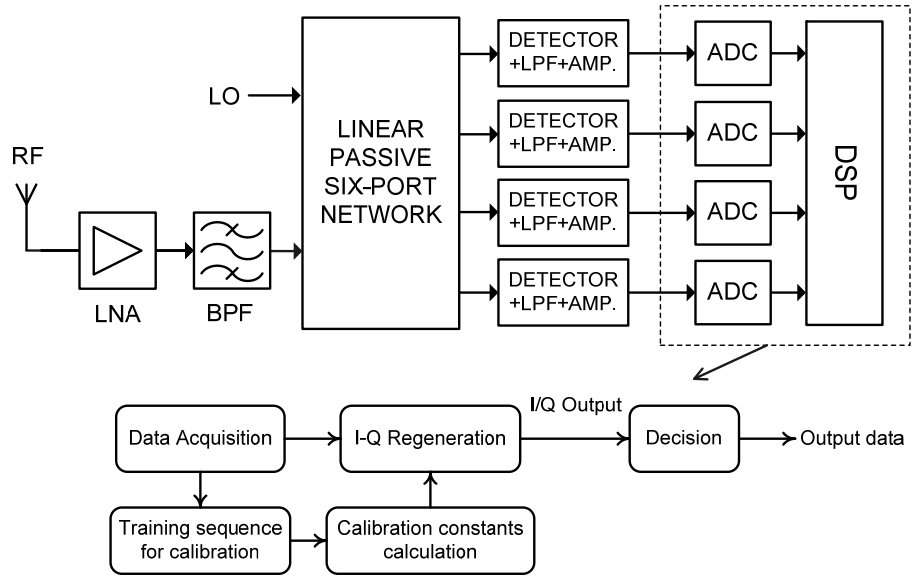

Fig. 2.16: Structure of a software defined radio six-port receiver.

commented above. Fig. 2.16 shows the structure of a SDR six-port receiver, which uses a real-time calibration algorithm based on training sequence.

In the last years, several SDR multi-port receivers have appeared in the literature [14]-[18],[21],[78],[99]-[106]. These first results point six-port architecture in the right direction to be a good candidate for SDR implementation. However, commercial six-port receivers are not available yet, being conventional zero-IF receivers the most extended architecture for SDR implementation. Moreover, future communication systems will demand high bandwidths and high carrier frequencies, requirements that are difficult to handle for conventional homodyne and heterodyne receivers. In this context, six-port can be a valid alternative. Nowadays, the miniaturization of six-port receivers and its integration on a MMIC is the focus of current work.

2.5 SUMMARY

SDR puts new challenges on RF architectures capable of handling several standards and related software implementations. Success depends on architectural innovation and optimization. Here we have presented three RF architectures suitable for SDR implementation: zero-IF, low-IF, and six-port network. Six-port technique is very promising and flexible architecture for the low-cost design of integrated

microwave, millimeter-wave, and photonic systems. Competitive advantages such as broadband behaviour, low-cost, reconfigurability, low power consumption, etc., point to the six-port architecture as a good candidate to implement a SDR. Furthermore, six-port architecture shows high potential and advantages compared to conventional homodyne and heterodyne receivers for future communication systems, which will demand high bandwidths and high carrier frequencies.

In addition to the theoretical study presented in this chapter, several comparative studies based on simulation analysis were carried out. The conclusions extracted from these studies, although not directly presented in this thesis, resulted in a presentation in the *SDR forum European Reconfigurable Radio Technologies Workshop and Product Exposition 2009* [SDRF 2009], and a presentation in the national conference *Simposium Nacional de la Unión Científica Internacional de Radio URSI* in 2008 [URSI 2008]. More details can be also found in [107]. Moreover, some investigations on bandwidth extension techniques for microwave amplifiers were carried out, which resulted in the publication of a paper in The Open Electrical and Electronic Engineering Journal [TOEEJ 2008].

Chapter 3

EXPERIMENTAL VALIDATION OF THE SIX-PORT ARCHITECTURE AS A BROADBAND SDR RECEIVER

3.1 INTRODUCTION

Although the six-port receiver is said to be a good solution for the multi-band demodulation of high-speed signals, not many experimental demodulation results proving the two above characteristics have been published up to now. This chapter presents the design and development of a SDR six-port receiver for broadband applications. The work presented in this chapter demonstrates empirically and quantitatively the wideband behaviour of the six-port architecture, and the capability of performing high data rates.

3.2 BLOCK DIAGRAM AND SYSTEM REQUERIMENTS

Some parts of the work presented in this chapter have been developed under the framework of the TelMAX project [108]. TelMAX is a four-year research project funded by the Spanish Ministry of Science and Innovation, inside CENIT program. The objective of the TelMAX project is to research into a new concept of cellular communication system oriented to Public and Governmental Services. The system must be capable of providing mobility, wide-band IP connectivity services, QoS (Quality of Service) management and a robust and reliable link for voice, video and data professional services. The project is also expected to have a positive impact in other user environments, such as social services, teleassistance, telemedicine, or tele-education. However, the interconnection of Public and Governmental Services requires the interoperability between heterogeneous radio-communication networks.

Since different professional services will have to be interconnected, a flexible and reconfigurable architecture is needed. Our work was precisely focused on the investigation and optimization of RF architectures, with the objective of achieving such a universal and flexible radio platform, with multi-mode and multi-band capabilities.

Our objective is thus to develop a reconfigurable radio front-end for broadband mobile applications. Nowadays, the aim of a SDR for mobile applications can be reduced to receive every standard up to 6 GHz, as all cellular and WLAN communications are located in that frequency range. In particular, TelMAX requirements impose three operating frequency bands: 698-862 MHz, 2500-2690 MHz, and 5725-5850 MHz. Consequently, we have implemented a 698–5850 MHz (three–octave) six–port receiver prototype. The system can operate with broadband signals, from 1 MHz to 100 MHz–wide channels, and different modulation schemes.

The block diagram of the proposed six-port receiver is that shown in Fig. 3.1. We have selected one of the most typical six–port topologies, composed of three 90-degree hybrid couplers and a Wilkinson power divider [13],[80],[78]. The receiver includes a diode detector, a low-pass filter and a video amplifier at each six-port network output. It is worth to mention that the low noise amplifier (LNA) and the automatic gain control (AGC) stage have not been included in the prototype, although these components would be necessary in a SDR front-end. Another important issue in a SDR implementation is the RF filtering to eliminate the out-of-band interference signals. But multi-band or tuneable RF filters are difficult to design over large frequency ranges. Conventional multi-band filtering techniques have consisted of filter banks, with the disadvantage of the circuit size. More advanced techniques are based on single circuits performing the multi-band filtering. Some solutions of dual-, triple-, or quad-band filters have been proposed [109]-[113], and currently the efforts are focused on the design of multi-band filters with an arbitrary number of pass-bands [114]. Microelectromechanical systems (MEMS) devices have displayed remarkable characteristics as variable devices and have been applied as tuneable or reconfigurable multi–band RF circuits [115]. Anyway, the multi-band frequency-selective filtering is a wide research area and it would deserve a separate investigation, which is far from the objective of this thesis.

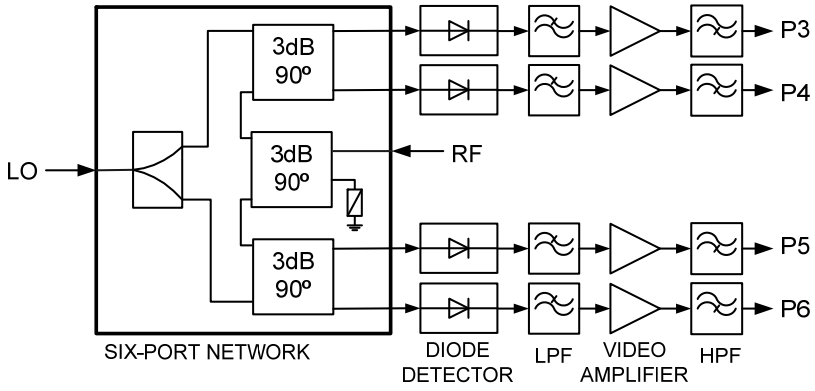

Fig. 3.1: Block diagram of the proposed broadband SDR six-port receiver.

3.3 SIX-PORT RECIEVER DESIGN AND SIMULATION

3.3.1 Six-port network

The chosen six-port network topology comprises three 90-degree hybrid couplers and a Wilkinson power divider, as shown in Fig. 3.2. In this configuration, the output six-port signals are combinations of the input RF and LO signals with different relative phase shifts of 0, $\pi/2$, $-\pi/2$, and π rad. This is a typical six-port network configuration, not only because it can achieve very large relative bandwidths, but also because it is susceptible of analog IQ regeneration.

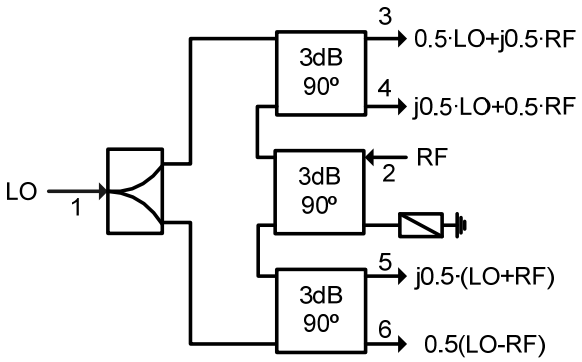

Fig. 3.2: Six-port network topology.

The system bandwidth is conditioned by the hybrid couplers, as they must ensure a frequency independent phase shift. The greatest difficulty is to design a 3 dB coupler over the three octave operating bandwidth (698–5850 MHz). Branch-line and rate-race couplers are suitable for obtaining tight coupling values, such as 3 dB.

However, these couplers are inherently narrowband circuits (<20% bandwidth). The use of 3 dB Lange couplers enhances the bandwidth, but only up to one octave. Therefore, a solution has to be found for achieving a multi-octave tight coupler.

The power divider is not as critical as the hybrid coupler, since the required bandwidth can be obtained by means of a multisection design. In fact, there are some commercial products that cover the desired frequency band, thereby we will use a commercial power divider.

Let us move on the detailed description of the 90-degree hybrid coupler and the power divider.

3.3.1.1 90-degree hybrid coupler

One alternative to obtain a tight coupler consists in connecting two couplers in tandem [116]. In a tandem connection, the direct and coupled ports of the first coupler are connected to the isolated and input ports of the second coupler, respectively, as shown in Fig. 3.3. It can be demonstrated that the tandem connection of two 8.34 dB couplers leads to a 3 dB coupler [117]. Then, a three octave 3 dB coupler could be obtained from two 8.34 dB multisection couplers. In addition, the isolation achieved by connecting two couplers in tandem is better than that obtained with one of the couplers separately.

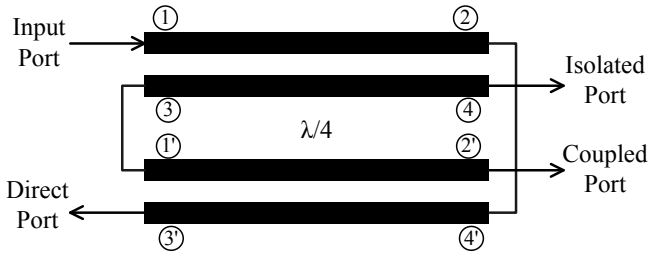

Fig. 3.3: Schematic of a tandem coupler.

Multisection tandem couplers are a good solution to implement ultra-large relative bandwidth tight couplers. For example, in [118] Potter et.al. presented a multilayer 3dB tandem coupler, covering the frequency range from 750 MHz to 26.5 GHz with 22 λ/4 sections. This coupler was used to implement a reflection analyzer based on the six-port technique [79]. However, one of the main problems is that a very good accuracy is needed in the fabrication process, especially at high frequencies. For

instance, Potter points that a 5 μm error corresponds to 5º quadrature distortion at 26.5 GHz [118]. In our case, such high frequencies will not be reached, so accuracy requirements can be relaxed.

The structure of an *N*-section symmetrical coupler is shown in Fig. 3.4. Each section is a λ/4 length section at the central design frequency. It is common to use an odd number of sections, thereby *i*-section is equal to (*N+1-i*)-section. By choosing N odd, the phase behaviour of the coupler improves.

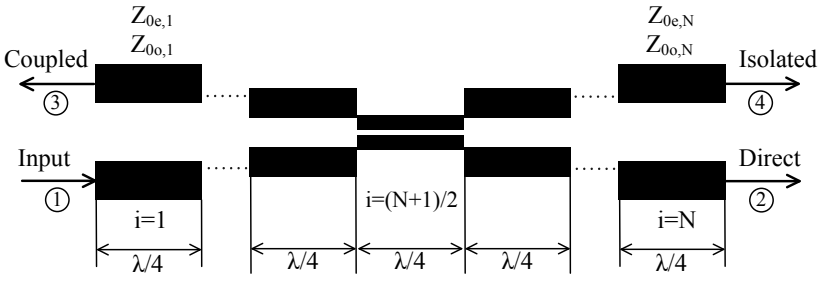

Fig. 3.4: N-section symmetrical directional coupler.

The even- (Z_{0e}) and odd-mode (Z_{0o}) impedances of the *i*th section of the multisection coupler are related by

$$Z_{0o,i} = \frac{Z_0^{\,2}}{Z_{0e,i}} \tag{3-1}$$

where Z_0 is the impedance terminating the ports of the directional coupler. The coupling level of the *i*th section is given by

$$k_i = \frac{Z_{0e,i} - Z_{0o,i}}{Z_{0e,i} + Z_{0o,i}} \tag{3-2}$$

which, expressed in decibels, results in

$$C_i = 20\log(k_i) \tag{3-3}$$

The synthesis theory of symmetrical multisection directional couplers is described in [119]-[120]. Young and Cristal [119] compiled tables of designs for three-, five-, seven-, and nine-section symmetrical couplers. The design tables are given for maximally flat and equal-ripple symmetrical couplers. We will choose an

equal-ripple response, since larger bandwidths can be achieved. The tables give the normalized even-mode impedances (Z_{0e}/Z_0) for different values of mean coupling, and maximum amplitude deviation from the mean coupling (δ). Two bandwidth definitions for directional couplers are in common use, and both are presented in the design tables.

- Fractional bandwidth:

$$\omega = \frac{f_2 - f_1}{f_0} \tag{3-4}$$

where f_2 and f_1 are, respectively, the upper and lower frequencies of the operating frequency range, and f_0 is the central frequency.

- Bandwidth ratio:

$$B = \frac{f_2}{f_1} \tag{3-5}$$

In our case, a mean coupling of 8.34 dB and a bandwidth ratio of B=5850/698=8.38 are needed for the design of each 8.34dB coupler forming the 3dB tandem coupler. From the design tables [119], we obtain that it is possible to cover the specified bandwidth with five λ/4 sections and a maximum deviation of 0.7 dB from the mean coupling. With seven λ/4 sections it is possible to achieve a 0.3 dB maximum deviation, and a theoretical bandwidth ratio of B=8.4458. In a good six-port network design it is convenient to minimise amplitude imbalance, so seven λ/4 sections are more appropriate. An amplitude deviation of 0.35 dB will be selected in order to increase the bandwidth ratio to B=8.9622, and thus the margin of error. In such a case, and for Z_0=50 Ω, the parameters of the 8.34dB coupler are that compiled in Table 3.1.

Note that the highest coupling level required by the design, which corresponds to the central section coupling, is 3.85 dB. The problem is that edge-coupled structures do not provide coupling levels higher than 8 dB. Therefore, a microstrip coupler design with edge-coupled type lines is dismissed. Broadside-coupled lines are more suitable, as they achieve coupling levels up to 2 or 3 dB. Consequently, we will implement a seven section 3 dB tandem coupler with broadside-coupled striplines.

Table 3.1 Parameters of a seven-section 8.34 dB coupler: δ=0.35 dB, B=8.9622.

Section	Z_{0e} (Ω)	Z_{0o} (Ω)	C (dB)
1,7	52.0815	48.0017	27.79
2,6	55.7975	44.8049	19.23
3,5	64.628	38.6829	12.00
4	107.022	23.3597	3.85

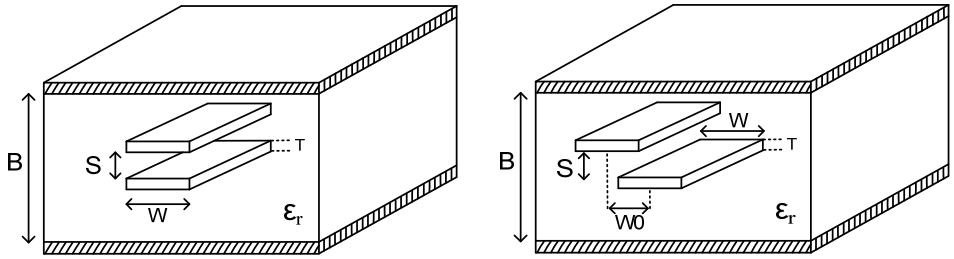

(a) (b)

Fig. 3.5: Broadside-coupled striplines (a) Overlap coupled striplines (b) Offset coupled striplines.

The decision of the substrate parameters is conditioned by the central section coupling level. Coupling can be maximised by reducing the separation of the inner conductors, and increasing the distance to the ground planes. A low dielectric constant substrate also maximises the highest coupling, as the ground plane separation will be large relative to the overlay separation. However, this increases the circuit dimension. We have chosen a 2.17 Cu-Clad substrate, with 380 μm inner conductor separation, and 1143 μm ground separation. The stripline structure is formed by joining three substrate layers, resulting in a 1143-380-1143 μm sandwich. A theoretical 4 dB central section coupling is achieved with 50 Ω overlap broadside-coupled striplines, which is not exactly the required 3.85 dB coupling. However, the other possibility is to use a 254 μm substrate layer instead of a 380 μm one, leading to a 3 dB central section coupling with 50 Ω overlap broadside-coupled striplines. The deviation from the required 3.85 dB coupling is larger in this latter case. Moreover, the central section lines could be separated in order to achieve the 3.85 dB coupling. However, if uniform coupled symmetrical lines were used, crossovers would be required in order to achieve proper interconnections between the couplers, making the coupler fabrication more difficult. Then, the stripline structure parameters are:

$$\begin{aligned} &\varepsilon_r = 2.17 \\ &B = 2.666\ mm \\ &S = 0.38\ mm \\ &T = 0.02\ mm \\ &\tan\delta = 0.0009 \end{aligned} \tag{3-6}$$

where ε_r is the relative dielectric constant, b is the ground plane spacing, S is the spacing between lines, T is the conductor thickness, and $tan\delta$ is the dielectric loss tangent.

Taking into account the parameters of Table 3.1, the conductor width, w_i, and the conductor offset, $W0_i$, of each λ/4 section would be the following

$$\begin{aligned} &w_1 = 2.105\ mm;\ \ W0_1 = 3.665\ mm \\ &w_2 = 2.06\ mm;\ \ W0_2 = 2.776\ mm \\ &w_3 = 1.87\ mm;\ \ W0_3 = 1.97\ mm \\ &w_4 = 1.37\ mm;\ \ W0_4 = 0\ mm \end{aligned} \tag{3-7}$$

However, the fact that only 4 dB of coupling can be achieved for the central section, instead of the required 3.85 dB, involves that the mean coupling of the 8.34 dB seven-section coupler is slightly lower than -8.34 dB, and the amplitude ripple is not perfectly constant over the frequency band. Obviously, these deviations increase when the two 8.34 dB couplers are connected in tandem. Therefore, the conductor line offsets will be modified in order to optimize the frequency response of the 3 dB tandem coupler. The new conductor offsets are:

$$\begin{aligned} &W0_1 = 3.865\ mm \\ &W0_2 = 2.905\ mm \\ &W0_3 = 2.025\ mm \\ &W0_4 = 0\ mm \end{aligned} \tag{3-8}$$

ADS (Advanced Design System) software [121] has been used for the simulations. The schematic of the stripline 3 dB tandem coupler is presented in Fig. 3.6. It includes the connection lines between the two 8.34 dB couplers, and the equivalent circuit elements for discontinuities. The corresponding simulated amplitude and phase responses are plotted in Fig. 3.7 and Fig. 3.8, respectively.

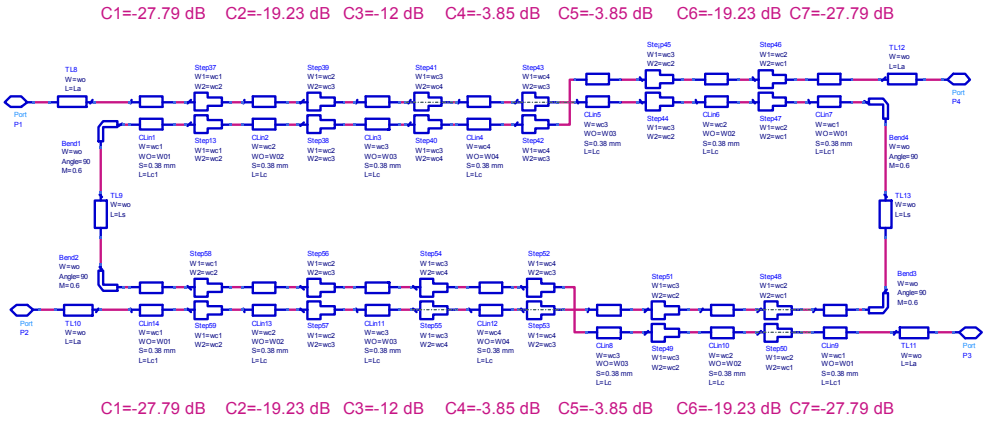

Fig. 3.6: Simulation schematic of the stripline 3dB tandem coupler.

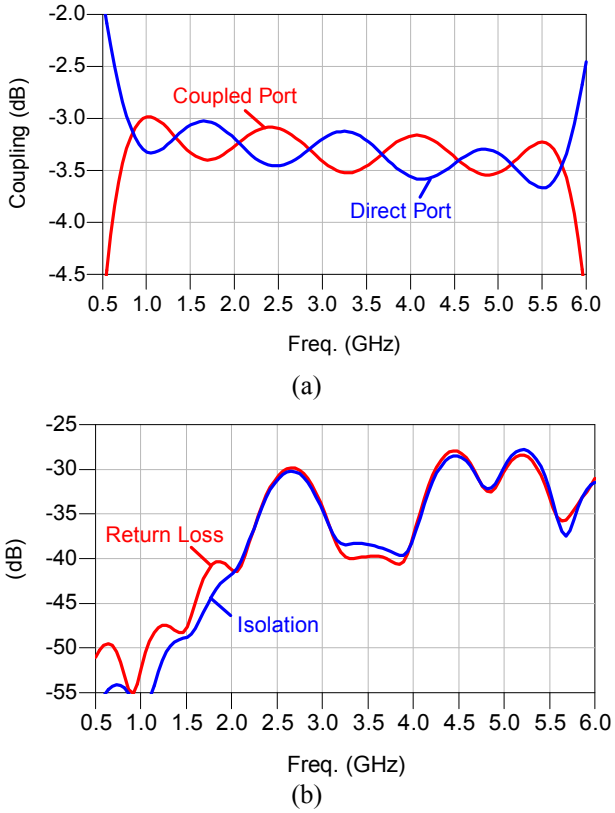

Fig. 3.7: Simulated amplitude response of the stripline 3 dB tandem coupler (circuital simulation): (a) Coupling, (b) Input return loss and isolation.

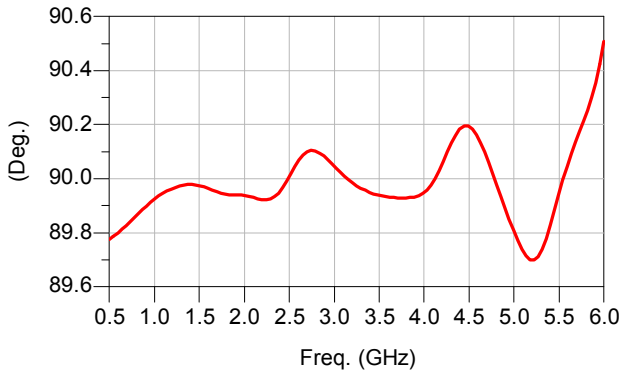

Fig. 3.8: Simulated phase difference between coupled and direct ports of the stripline 3 dB tandem coupler (circuital simulation).

A more accurate analysis of the coupler can be performed using electromagnetic (EM) simulations. Then, additionally to circuital simulations, 2.5D EM simulations have been performed using Momentum [122]. The layout of the 3dB tandem coupler generated from Momentum appears in Fig. 3.9. The upper conductor lines are represented in yellow, and the bottom ones in brown. The dimensions of the designed coupler are 130x17 mm^2. The EM simulated amplitude and phase responses are presented in Fig. 3.10 and Fig. 3.11, respectively. According to EM simulations, the maximum amplitude imbalance between the direct and coupled ports is 1 dB, and the maximum phase imbalance is 1.6º. The input return loss and isolation are below -20dB up to 4 GHz, and below -15 dB from 4 GHz to 6 GHz.

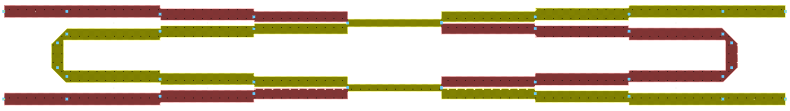

Fig. 3.9: Layout of the 3dB tandem coupler generated from Momentum.

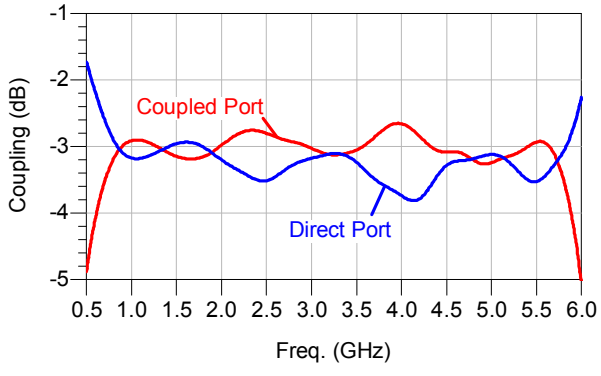

(a)

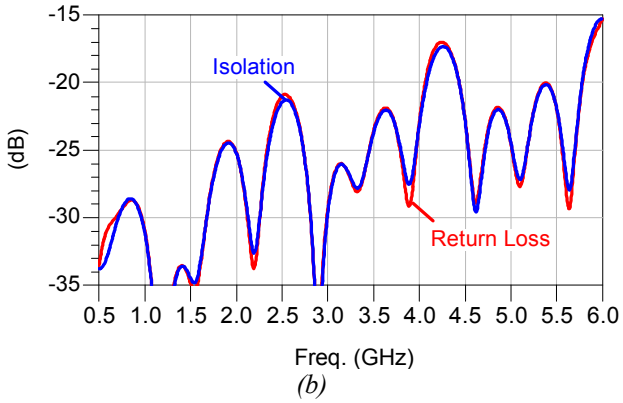

(b)

Fig. 3.10: Simulated amplitude response of the stripline 3 dB tandem coupler (EM simulation): (a) Coupling, (b) Input return loss and isolation.

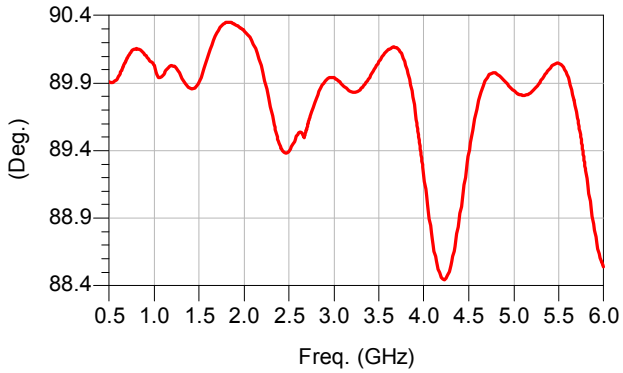

Fig. 3.11: Simulated phase difference between coupled and direct ports of the stripline 3 dB tandem coupler (EM simulation).

3.3.1.2 Power divider

A commercial power divider has been used to implement the six-port network. In particular, we have used the LYNX 111.A0214 power divider, whose characteristics are summarized following

- Frequency range: 0.5 – 6 GHz
- Insertion loss: 3.8 dB
- Isolation: 18 dB
- Input VSWR: 1.4
- Output VSWR: 1.3
- Amplitude balance: ±0.2 dB
- Phase balance: ±3 º
- Power handling: 30 W

3.3.1.3 Simulation of the six-port network response

The next step is to simulate the frequency response of the overall six-port receiver. The circuital schematic used for the simulation is shown in Fig. 3.12. The power divider manufacturer does not provide the scattering parameters of the LYNX 111.A0214 power divider. Therefore, it has been modelled as an ADS divider element, whose parameters are constant in frequency an equal to the worst case values given by the manufacturer (see section 3.2.1.2). That is:

- Amplitude balance: +0.4 dB→ $|S_{21}|$ = -3.6 dB; $|S_{31}|$ = -4 dB
- Phase balance: +6 º→ Φ_{S21} = -3 º; Φ_{S31}= 3 º
- $|S_{32}|$ = -18 dB
- $|S_{11}|$ = -15.5 dB
- $|S_{22}|$ = -17.7 dB

The simulated amplitude response of the six-port network is presented in Fig. 3.13-Fig. 3.16. The simulated attenuations from the LO and RF ports to the output ports of the six-port network are plotted in Fig. 3.13, and Fig. 3.14, respectively. Fig. 3.15 represents the simulated input return loss and isolation, while Fig. 3.16 represents the output return loss.

The attenuation from the LO port to the output ports 3 and 4 is -6.8±0.6 dB, and it is -7.2±0.6 dB to ports 5 and 6. These additional attenuations of 0.8 dB and 1.2 dB at ports 3/4 and 5/6, respectively, are due to the insertion loss and amplitude imbalance of the power divider. The maximum attenuation deviation with respect to the ideal value from the RF port is 0.7 dB at port 3, 2 dB at port 4, 1 dB at port 5 and 1.5 dB at port 6. The input return loss at the RF port is better than 17.5 dB. At the LO port, the input return loss is below -12 dB, since it is limited by the power divider input match. A good isolation between the RF and LO ports is achieved, with values better than 23 dB. As for the output return loss, in the worst case it is -14.4 dB at ports 3 and 6, and -12.1 dB at ports 4 and 5.

With regard to the six-port phase response, according to the six-port topology (Fig. 3.2) and taking port 3 as reference port, the phase shifts from the RF port to output ports 4, 5, and 6 are -90º, 0º, and 90º, respectively. Moreover, the phase shifts from the LO port to output ports 4, 5, and 6 are 90º, 90º, and 0º. That is, the output six–port signals are combinations of the input RF and LO signals with different relative

phase shifts of 0, π/2, –π/2, and π rad. These phase relations must be kept over the whole operating frequency range to ensure proper six-port network behaviour. The simulated phase shifts from the RF port to output ports are presented in Fig. 3.17. The maximum simulated deviation from the ideal phase value is 5º at port 4, 3.4º at port 5, and 2.15º at port 6. As for the phase shifts from the LO port, plotted in Fig. 3.18, a residual error of 6º can be appreciated in ports 5 and 6, due to the phase imbalance value introduced in the power divider model. However, this value corresponds to the worst case, thus the real response may be different. In this case, the maximum simulated phase shift error is 2.46º at port 4, 8.5º at port 5, and 6.4º at port 6.

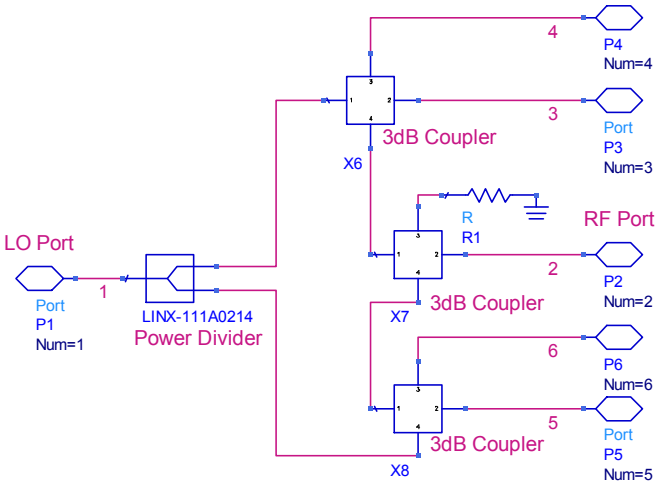

Fig. 3.12: Simulation schematic of the six-port network.

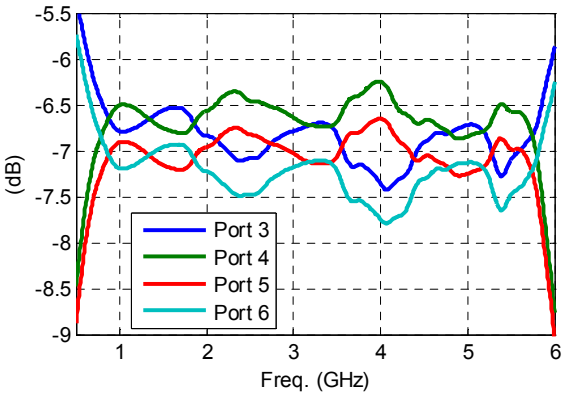

Fig. 3.13: Simulated attenuation from LO port to output ports of the six-port network.

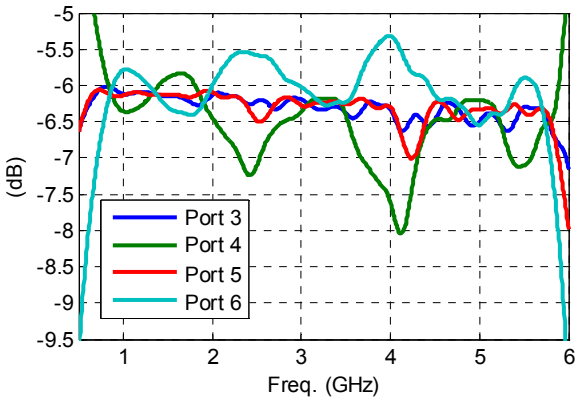

Fig. 3.14: Simulated attenuation from RF port to output ports of the six-port network.

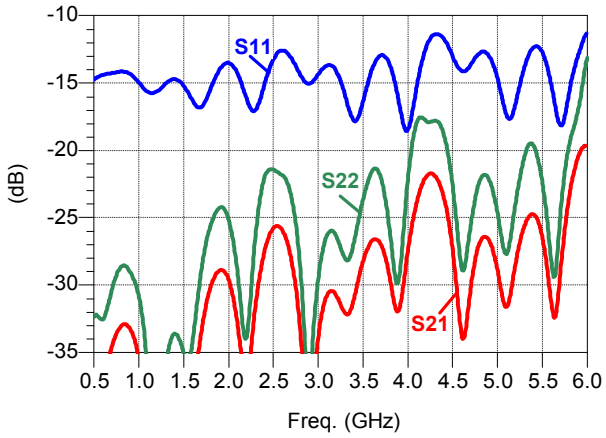

Fig. 3.15: Simulated input return loss and isolation of the six-port network.

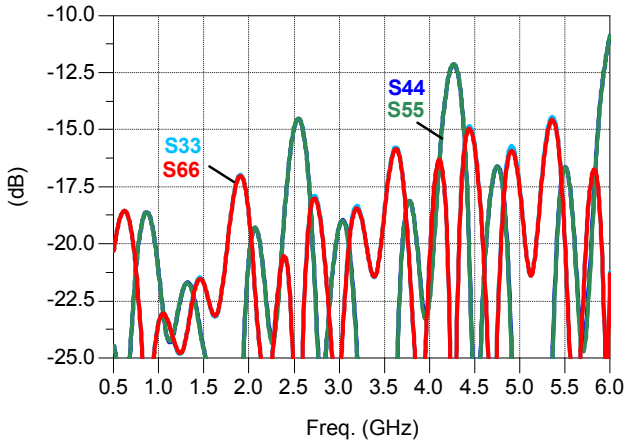

Fig. 3.16: Simulated output return loss.

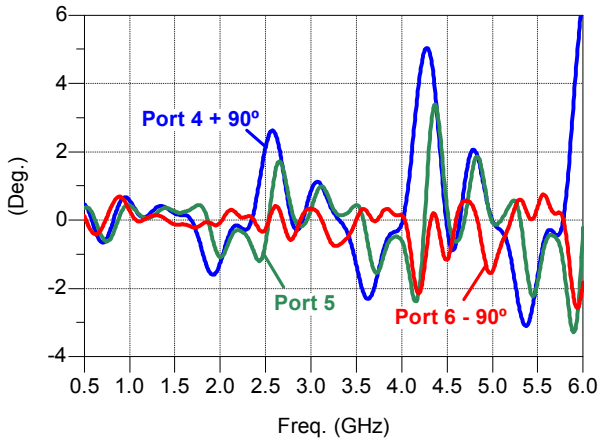

Fig. 3.17: Simulated phase shift from RF port to output ports of the six-port network, considering Port 3 as reference port.

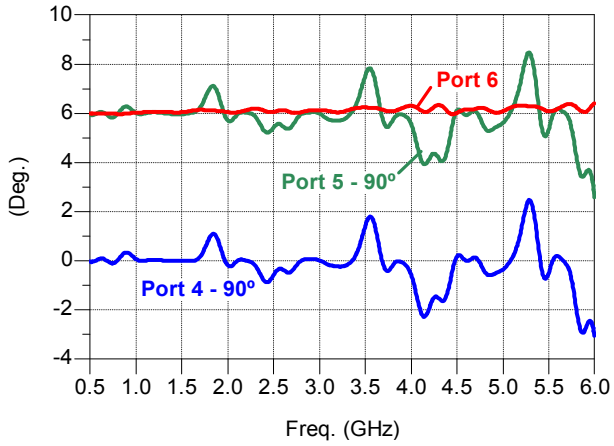

Fig. 3.18: Simulated phase shift from LO port to output ports of the six-port network, considering Port 3 as reference port.

3.3.2 Power detectors

3.3.2.1 Design considerations

A typical video detector circuit is shown in Fig. 3.19 [84],[123]. At RF, the bypass capacitor (C_b) appears as a short circuit, and the input RF choke (RFC) appears as an open circuit. Due to the nonlinearity of the diode, the video signal is extracted from the modulated RF signal and appears across the video load resistance R_L. At video frequencies, *RFC* acts as a short circuit, while C_b and the DC bias filter, consisting of *LFC* and C_c, appear as high impedances. RFC also serves as a return path for the DC bias current.

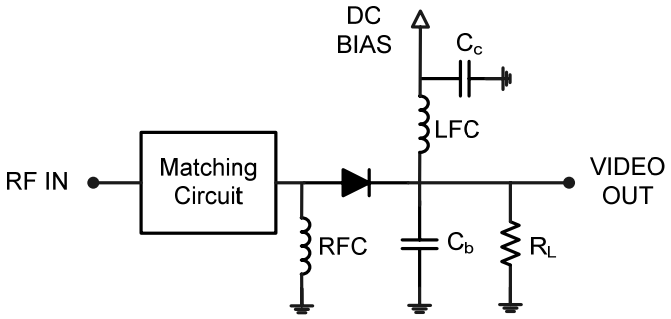

Fig. 3.19: Basic detector circuit.

The starting point in diode detector design is the small-signal equivalent circuit of the Schottky diode, which is shown in Fig. 3.20. It consists of a biased-dependent junction resistance R_j and capacitance C_j, and a parasitic series resistor R_S. L_p and C_p represent the package inductance and capacitance, respectively.

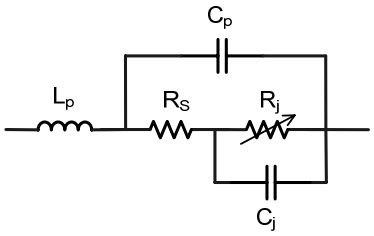

Fig. 3.20: Schottky diode equivalent circuit.

The junction resistance R_j is given by:

$$R_j = \frac{nkT}{q(I_B + I_S)} \tag{3-9}$$

where T is the temperature in ^oK, $q=1.6021917\cdot10^{-19}$ C is the electron charge, $k=1.38\cdot10^{-23}$ *Joule/K* is the Boltzmann's constant, I_B is the externally applied bias current in amps, I_S is the saturation current in amps, and n is the ideality factor.

One characteristic parameter of detector diodes is the video resistance, R_V. In general, the lower the diode's video impedance, the better the design. R_V consists of the sum of the diode's series resistance and the junction resistance:

$$R_V = R_j + R_S \tag{3-10}$$

As for diode selection, one should consider that the small signal diode cut-off frequency should be large relative to the operating frequency. The diode cut-off frequency is given by

$$f_c = \frac{1}{2\pi R_S C_{j0}} \tag{3-11}$$

being C_{j0} the zero-volt junction capacitance. Typically, a value $f_c > 10 \cdot f$ would be used, corresponding to

$$C_{j0} = \frac{1}{20\pi R_S f} \tag{3-12}$$

A small value of C_{j0} would result in a high-Q diode hard to match over a broad bandwidth. Thus, for broadband applications, diodes with a large C_{j0} are often used. In addition, it is advisable to select a diode with low package parasitics in the desired bandwidth.

The principal requirements for a video detector are distortionless recovery of the modulation signal, and maximum RF sensitivity. However, these requirements are competitive, and result in the design being a good compromise between video bandwidth and RF sensitivity. To obtain maximum sensitivity at any given frequency, most detector diodes must be forward DC biased. Moreover, the addition of bias current is seen to reduce the variation in voltage sensitivity with frequency and temperature. It also reduces the diode quality factor, which reduces the complexity of the RF matching circuit. However, when bias current is used, there is a trade-off in sensitivity and square law dynamic range [124]. The dynamic range increment is achieved with high bias currents, while sensitivity is maximized at small values of bias current.

The system specifications impose two strict requirements for the detector design: very large operating frequency range (698-5850 MHz), and wide video bandwidth (up to 50 MHz baseband channels). The use of bias current involves some advantages especially suitable for our design. On one hand, the reduction of the sensitivity variation with frequency and the simplification of the RF matching circuit are important advantages, taking into account the large operating frequency range. On the other hand, the dynamic range extension due to bias current is particularly

advantageous for a SDR receiver, since different standards with different power levels have to be supported. Consequently, the DC biased HSMS-286B Schottky diode will be used, whose parameters are presented below

$$\begin{aligned} R_S &= 5\ \Omega \\ C_{j0} &= 0.18\ pF \\ L_p &= 2\ nH \\ C_p &= 0.08\ pF \\ I_S &= 5{\cdot}10^{-8}\ A \\ n &= 1.08 \end{aligned} \tag{3-13}$$

Detector design is a compromise between several competing requirements, including operating frequency, video bandwidth, input RF impedance, sensitivity, square law dynamic range, and temperature extremes.

3.3.2.1.1 Voltage sensitivity

The detector voltage sensitivity, assuming a perfect lossless impedance match at the diode's input, can be expressed as [84]

$$\beta_v = \frac{0.5R_L}{(I_S + I_B)\cdot(R_V + R_L)\cdot(1 + R_S / R_j)\cdot[(1 + R_S / R_j) + (\omega C_j)^2 R_S R_j]} \quad (V/W) \tag{3-14}$$

This parameter specifies the slope of the output video voltage versus the input signal power of the diode, i.e.:

$$V_{out} = \beta_v \cdot P_{in} \tag{3-15}$$

For a typical diode with no bias, the voltage sensitivity shows a strong dependence on frequency. Biasing the diode reduces the variation in voltage sensitivity, as shown in Fig. 3.21, where the theoretical HSMS-286B diode voltage sensitivity is plotted for R_L=100 KΩ. However, it results in a sensitivity reduction at the lower frequencies.

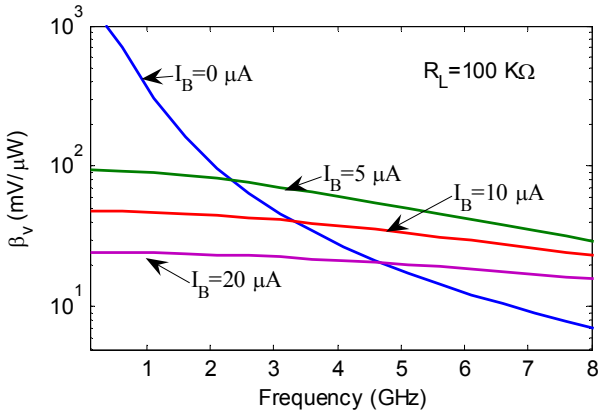

Fig. 3.21: Theoretical detector diode voltage sensitivity, HSMS-286B.

The voltage sensitivity is a parabolic-type function with $I_T = (I_S + I_B)$, whose maximum value at any particular frequency is given by

$$I_{T,opt} = \frac{\omega C_j}{\alpha}\sqrt{\frac{R_S}{R_L}} \quad (A) \tag{3-16}$$

with $\alpha = q/nkT$. For highest sensitivity, one requires $R_S << R_j$ and $R_L >> R_j$. For currents greater than $I_{P,opt}$, β_v drops due to the reduced voltage across the diode junction. For currents less than $I_{P,opt}$, R_j gets large relative to R_L, and the sensitivity is reduced due to the $R_L/(R_L+R_V)$ voltage divider. For example, the measured data provided by the manufacturer (see Fig. 3.22) show an optimal bias current of 5 μA for the HSMS-286B diode at 2.45 GHz and a load resistance R_L=100 KΩ.

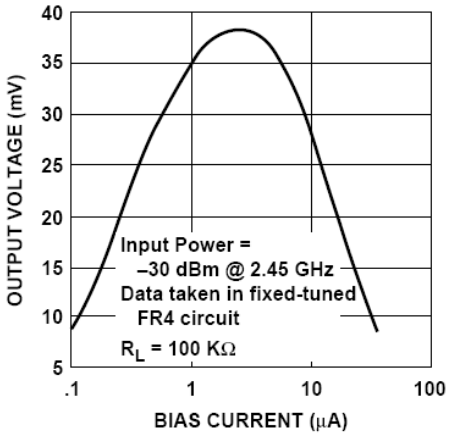

Fig. 3.22: Voltage sensitivity as a function of bias current at 2.45 GHz, HSMS-286.

The diode sensitivity also varies with temperature, due to the dependence of the junction resistance with temperature (see eq. (3-10)). Again, the addition of a bias current reduces this variation in voltage sensitivity.

3.3.2.1.2 Tangential sensitivity

A way to characterize a detector's low-level performance is the tangential sensitivity (TSS), defined as the condition when the negative noise peaks riding on the detected voltage equal the noise peaks when no signal is present [84]. The detector TSS is a function of the bias current, RF frequency, video bandwidth, and video amplifier noise figure. Biasing has the same effect on the TSS than in voltage sensitivity. For a given frequency, there is a bias current which maximizes TSS. A small bias current generally provides the best TSS performance.

3.3.2.1.3 Dynamic range

The square law dynamic range is the range over which the output signal voltage is proportional to the input signal power, i.e., $V_{out} = \beta_v \cdot P_{in}$. Deviation from square-law characteristic occurs when β_v departs from a constant value. The dynamic range may be defined as the difference between the power input for 1 dB deviation from the ideal square law response (compression point), and the input power corresponding to the maximum TSS [124].

In addition to high sensitivity, video detectors are usually required to have a large dynamic range. However, the conditions that assure maximum sensitivity do not provide the maximum value of the compression level.

The compression level can be raised by reducing R_L. Nevertheless, the degradation in TSS exceeds the improvement in compression, so there is no improvement in dynamic range. Another possibility is to increase the bias current. This also degrades the TSS, but in this case the improvement in compression exceeds the sensitivity degradation, as shown in Fig. 3.23. Therefore, when stating bias current, there is a trade-off in sensitivity and square law dynamic range.

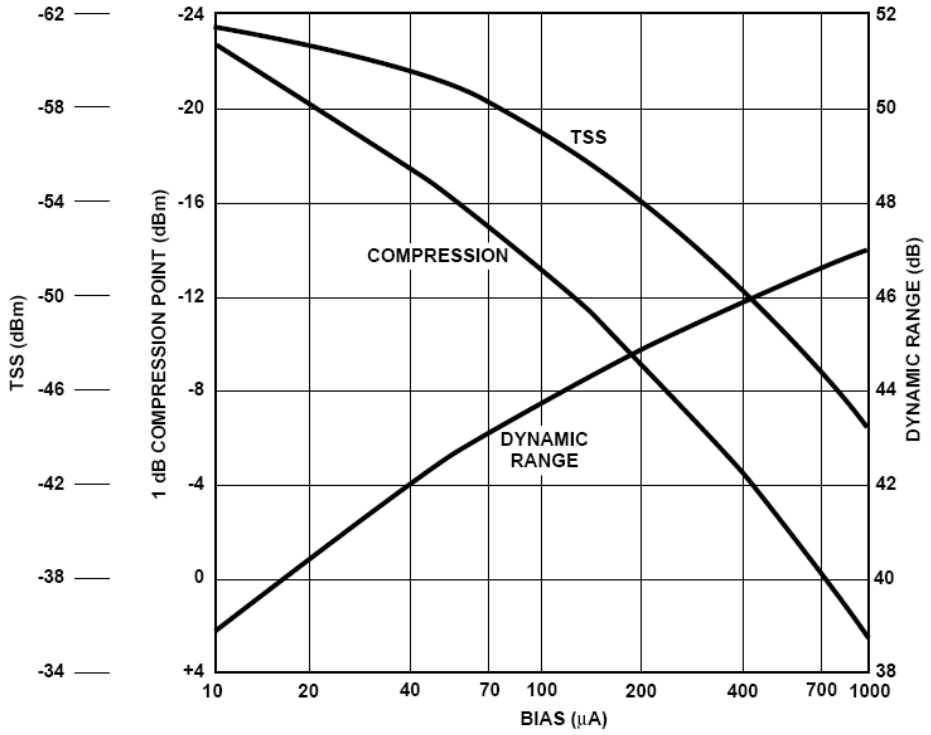

Fig. 3.23: Dynamic range improvement with bias, HP 5082-2751 detector (*© Hewlett-Packard App. Note 956-5* [124]).

3.3.2.1.4 RF input matching

One of the most difficult parts when dealing with a broadband detector circuit design is the input impedance matching network. The loss in power delivered to the diode due to mismatch leads to a loss in sensitivity as follows

$$\beta_v' = \beta_v \left(1 - |\Gamma|^2\right) \tag{3-17}$$

being Γ the detector input reflection coefficient.

The detector equivalent circuit at the video port is represented in Fig. 3.24. To simplify input matching, the impedance of the diode can be reduced by using a DC bias. This can be seen from Fig. 3.25, where the HSMS-286 diode input impedance is plotted for different values of bias current. For broadband matching, the DC bias can be greater than would normally be required for maximum voltage sensitivity. Although there will be a reduction of sensitivity, nevertheless, the trade-off may be worthwhile in broadband systems.

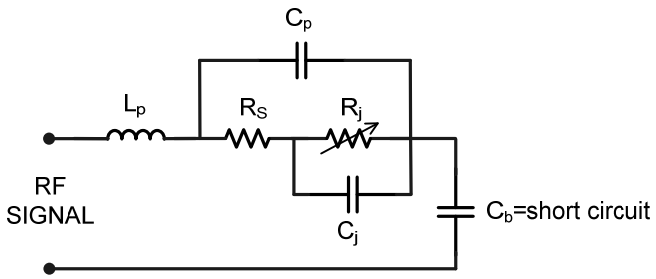

Fig. 3.24: Detector equivalent circuit at the RF port.

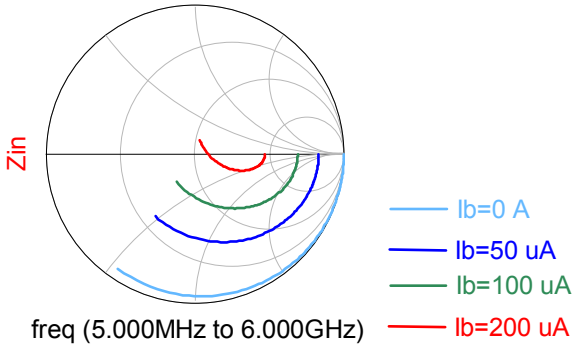

Fig. 3.25: HSMS-286 diode input impedance.

Wide-band detectors use to include a shunt 50 Ω resistor to give good input matching, but at the expense of detection sensitivity. HP recommends a 60 Ω resistor value for the HSMS-286B diode. In effect, by adding a shunt 60 Ω resistor input return loss clearly improves, as shown in Fig. 3.26.

Once the bias current is stated, the last step is to introduce a matching network.

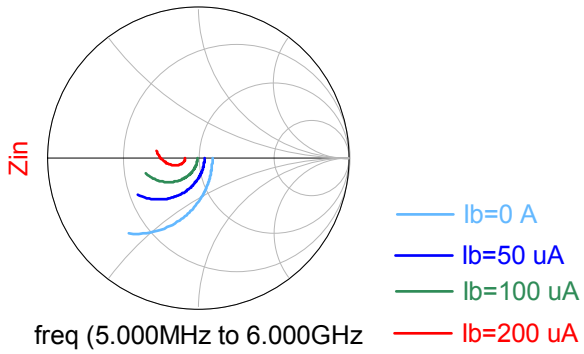

Fig. 3.26: HSMS-286 diode input impedance with a 60 Ω shunt resistor.

3.3.2.1.5 *Video bandwidth*

The detector equivalent circuit at the video port is represented in Fig. 3.27. The limit on the upper 3 dB cut-off frequency of this circuit is imposed by R_V, R_L and C_b as follows [123]:

$$f_{c3dB} = \frac{1}{2\pi R_T C_b} \tag{3-18}$$

where

$$R_T = \frac{R_V R_L}{R_V + R_L} \tag{3-19}$$

Conventional Schottky diode detectors use large load resistance and small bias current in order to maximize voltage sensitivity. Under such conditions, nevertheless, it is not possible to achieve very wide video bandwidths. It is clear from (3-18) that if video bandwidth is wanted to be maximized, a high load resistance will call for a high value of bias current to reduce R_V and minimize R_T. Detector design is a compromise between video bandwidth and RF sensitivity.

The video bandwidth can be increased by reducing all the element values within certain limits. A severe reduction in the value of the RF bypass capacitance C_b will lead to poor RF/video isolation and a decrease in the signal level delivered to the diode. The amount that R_L can be reduced is often limited if voltage amplification is desired, since the output voltage of the detector is maximized by making R_L large. R_V can be lowered by increasing the bias current. Although this results in reduced sensitivity, it may nevertheless be needed to achieve the required video bandwidth. It is worth to mention that a high bias current extends the square law dynamic range. On the contrary, reducing R_L does not lead to an improvement in dynamic range. However, bias introduces shot and flicker noise in the diode.

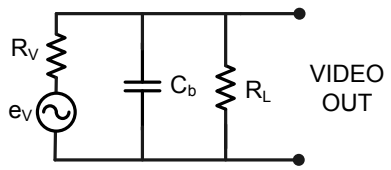

Fig. 3.27: Detector equivalent circuit at the video port.

Moreover, at low RF frequencies and wide video bandwidths it is difficult to achieve, at the same time and with a single capacitor, short-impedance at RF and high impedance at video frequencies. This situation occurs in our design, where the lowest RF frequency (698 MHz) calls for a bypass capacitance of at least C_b=100 pF, and the reactance of this capacitor is 31.8 Ω at the upper video frequency (50 MHz). In such a case, C_b can be replaced by a low pass filter structure, as shown in Fig. 3.28. The pass-band loss is determined by the voltage divider $R_L/(R_L+R_V)$, thus one should choose $R_V<<R_L$ for loss minimization. However, it has to be considered that the higher the load resistance, the higher the inductances and the lower the capacitances of the low-pass filter LC components.

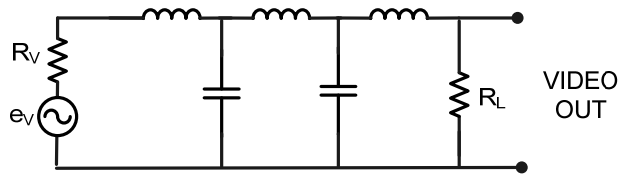

Fig. 3.28: Low-pass video coupling structure.

3.3.2.2 Wide video bandwidth and high dynamic range detector design

Our system specifications impose large RF operation frequency range (698-5850 GHz) and a wide video bandwidth (50 MHz). Obviously, such a detector will not have high voltage sensitivity, since sensitivity and video bandwidth are competitive parameters. A bias current higher than that required for maximum sensitivity will be needed to achieve the required video bandwidth. However, it will be advantageous for RF input matching and dynamic range extension.

Multiport architectures do not present good behaviour as for dynamic range, compared with heterodyne and conventional homodyne receivers. The main reason is that most of the six-port implementations use zero-bias detector diodes, matched at narrow band and/or with small video bandwidth. Consequently, no many experimental six-port demodulation results providing both multiband and high-data rate operation have been published up to now. Therefore, since the maximization of sensitivity will not be possible due to the wide video bandwidth, a high bias current will be selected in order to extend the dynamic range. The detector diode will be biased with bias current

I_b=1 mA. Such a high current will provoke large sensitivity degradation, whereby a video amplifier will be included.

The decision of R_L is determined by the pass-band insertion loss and the realizability of the low-pass filter structure (see Fig. 3.28). For example, a 100 KΩ 3-pole 50 MHz low-pass filter requires prohibitive values, such as two 318.3 μH inductors and one 63.6 fF capacitor. By reducing R_L to 1 KΩ, the capacitance value doubles, while the inductances values divide by two. Therefore, if high load impedance is selected, large inductance values may lead to very large size circuits and high loss due to the low inductor quality factor. On the other hand, pass-band insertion loss is minimized by choosing $R_V << R_L$. At 1 mA bias current, the diode junction resistance is R_V=31.8 Ω. For simplicity, a load impedance of 50 Ω has been selected, due to the numerous available commercial low-pass filters and amplifier devices. However, it is worth to emphasis that higher load impedance should have been more suitable for minimizing insertion loss, although it would have required a custom low-pass filter design. Many times, unfortunately, time restrictions lead to rapid solutions instead of optimum ones.

The *Minicircuits* RLP-50+ low-pass filter has been selected for the design. Its main characteristics are summarized below:

- 3 dB cut-off frequency: 59 MHz.
- Pass-band loss: < 2dB
- Stop-band loss: >20 dB @78-91 MHz; >40 dB @91-1000 MHz.
- VSWR: 1.1

Minicircuits provides the .s2p file of the RLP-50+ low-pass filter scattering parameters up to 200 MHz, which can be imported by ADS for simulation purposes.

The *Minicircuits* MAR8A+ model has been used for the video amplifier. Its main characteristics are presented in Table 3.2. These parameters will be introduced into an *Amplifier2* type block in ADS for simulation purposes.

The amplifier implementation responds to the recommended application circuit of Fig. 3.29, where the next values have been chosen:

- I_{bias}= 36 mA: Vcc= 9 V, R_{bias}=143 Ω.

Table 3.2 MAR8A+amplifier electrical specifications at 25ºC and 36 mA.

Parameter		Min.	Typ.	Max.	Units
Frequency range		DC		1	GHz
Gain	f=0.1 GHz f=1GHz	20	31.5 25		dB
Input return loss	f=DC to 1 GHz		15.5		dB
Output return loss	f=DC to 1 GHz		11		dB
Output power @1dB compression	f=1GHz		12.5		dBm
Output IP3	f=1 GHz		25		dBm
Noise figure	f=1 GHz		3.1		dB
Recommended operating current			36		mA
Operating voltage		3.2	3.7	4.2	V
Thermal resistance			119		ºC/W

- Cblock= 1.5 μF.
- Cbypass=100 nF and 10 μF in parallel connection.
- RFC=10 μH.

Remind that the six-port architecture is a direct frequency conversion scheme, which suffers from the DC-offset problem. The simplest solution for DC-offset rejection is by high-pass filtering with a series capacitor (AC-coupling). Then, the two block capacitors required for the video amplifier (*Cblock*) will be used for high-pass filtering. The cut-off frequency of the HPF has to be very low for not corrupting the wanted signal. As for Razavi [27], simulations indicate that the corner frequency of the HPF must be less than 0.1% of the data rate for the signal degradation to be negligible. In our six-port receiver, baseband channels from 1 MHz to 50 MHz have to be supported, which mandates a 760 Hz cut-off frequency for a 0.35 roll-off. This value is in agreement with the studies carried out previous to this thesis [107],[URSI 2008],[SDRF 2009], where a cut-off frequency less than 1 kHz was deduced for no signal degradation. Consequently, a value of 1.5 μF has been selected for *Cblock*.

The power detector will be implemented in microstrip technology, using a 2.17 Cu–clad substrate. The layout of the designed power detector is represented in Fig. 3.30.

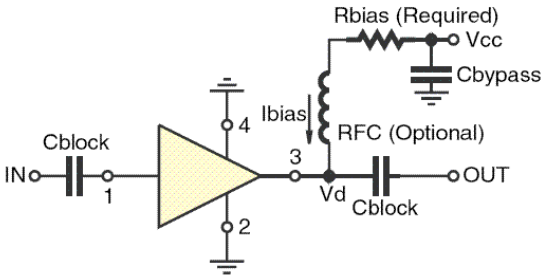

Fig. 3.29: Recommended application circuit for MAR8A+ implementation.

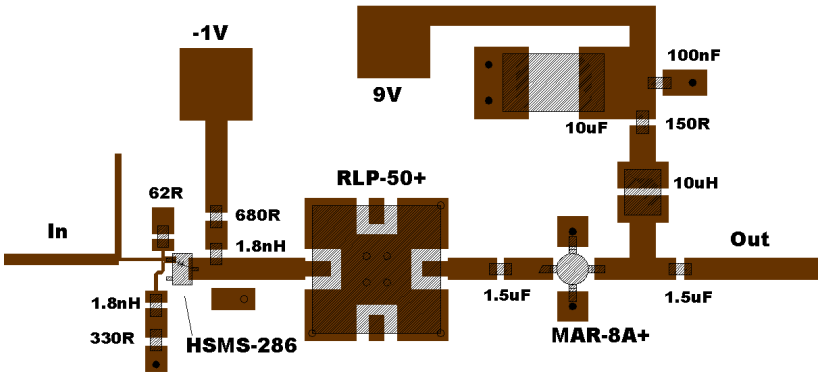

Fig. 3.30: Layout of the power detector.

3.3.3 Complete six-port receiver

Finally, the complete six-port receiver will be simulated. The circuit schematic of the designed six-port receiver can be seen in Fig. 3.31. Harmonic balance simulations will be performed in ADS to characterize the system.

Firstly, the four output voltage signals will be observed in the time domain. Note that the high-pass filter eliminates the DC component, thereby the received signal can not be analyzed at zero IF. Therefore, two RF tones separated 5 MHz will be introduced into the LO and RF inputs. The LO frequency will be set to the central frequency of the three specified frequency bands: 780 MHz, 2595 MHz, and 5786.5 Hz. The LO power will be 7.5 dBm, and the RF power will be -40 dBm. Fig. 3.32 presents the simulated four output voltages of the six-port receiver, for a 2595 MHz LO frequency. Ideally, according to the chosen six-port topology (see Fig. 3.2), the six-port receiver output signals have the same amplitude, and a relative phase shift of 90º, -90º, and 180º. The simulated amplitude and phase relations between the six-port receiver output signals at the three frequency bands are compiled in Table 3.3.

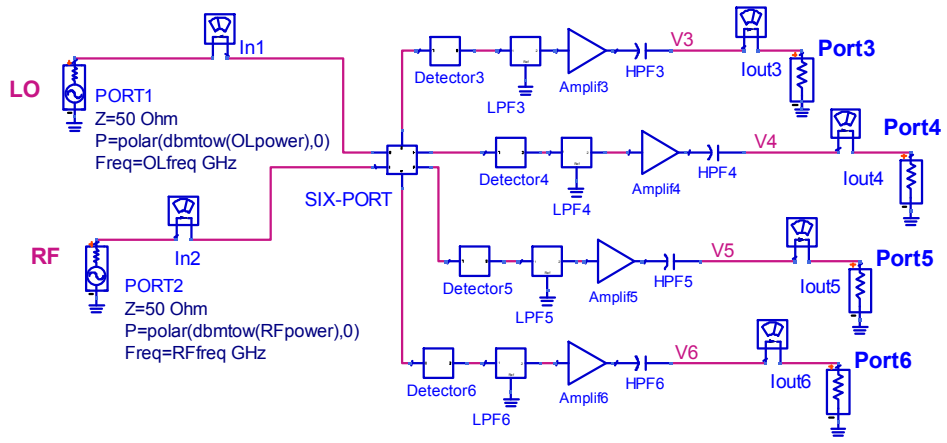

Fig. 3.31: Schematic of the six-port receiver.

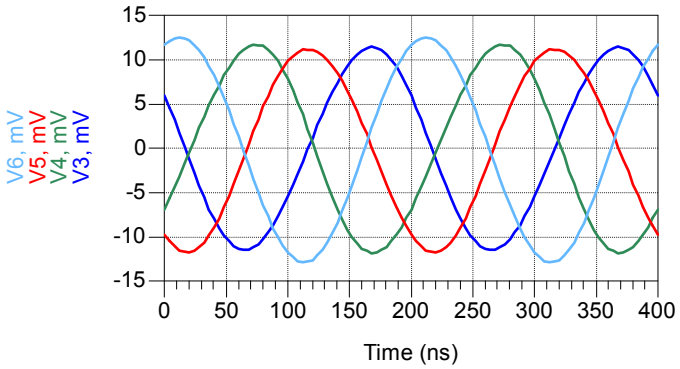

Fig. 3.32: Simulated output voltages of the six-port receiver: f_{LO}=2595 MHz, f_{RF}=2590 MHz, P_{OL}=7.5 dBm, P_{RF}=-40 dBm.

Table 3.3 Simulated amplitude and phase relations of the six-port receiver output signals.

Freq. Band	f_{LO} (MHz)	V_4/V_3 (dB/º)	V_5/V_3 (dB/º)	V_6/V_3 (dB/º)
1	780	-0.73/180.8	-0.77/101.2	-1.14/-86.5
2	2595	0.15/172.5	0.09/89.5	0.86/-82.6
3	5786.5	-2.0/182.9	-0.5/98.9	-1.7/-83.0

(*) f_{LO} - f_{RF}=5 MHz, P_{LO}=7.5 dBm, P_{RF}=-40 dBm.

Secondly, the IF response of the six-port receiver will be simulated. In this case, the RF frequency will be swept 200 MHz around the LO frequency value. The simulated six-port receiver IF response can be seen in Fig. 3.33. From DC to 50 MHz, the simulated small signal gain is 12.6±1.1dB at 780 MHz, 11.5±0.9 dB at 2595 MHz, and 7.5±1 dB at 5786.5 MHz. Moreover, the 3dB cut-off frequency is around 58.5 MHz.

It is worth to mention that the value of gain strongly depends on the LO power, as it can be seen from Fig. 3.34. The lower the LO power, the lower the six-port receiver gain. Nevertheless, a low value of LO has a positive influence on the power consumption, the even-order intermodulation distortion reject, and the reduction of the LO self-mixing problem. In fact, one of the advantages of the six-port architecture is that it can operate with low LO power values. Take into account that no RF amplification has been included in the design, which would increase the overall system gain. Therefore, in practice, it is advisable to reduce the LO power. Typical LO power levels of around 0 dBm are used in six-port receivers.

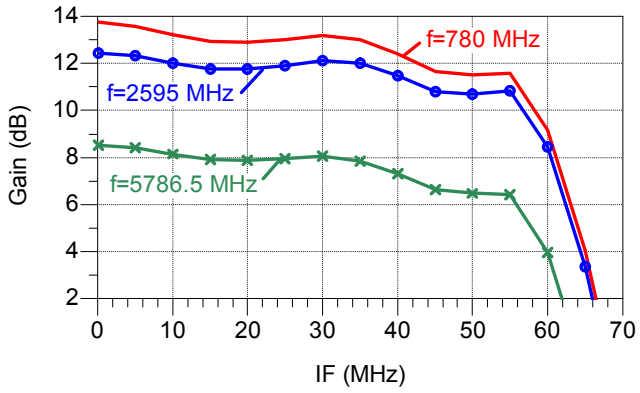

Fig. 3.33: Simulated six-port receiver IF response (at output port 3): P_{LO}=7.5 dBm, P_{RF}=-40 dBm.

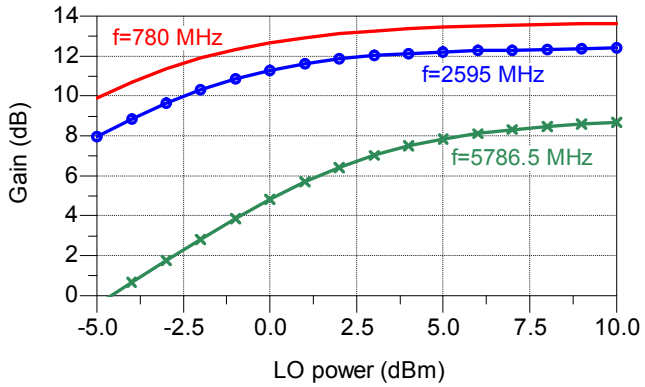

Fig. 3.34: Simulated six-port receiver gain versus LO power (at output port 3): f_{LO} - f_{RF}=5 MHz, P_{RF}=-40 dBm.

Next, the spurious signals reject will be analyzed. In direct frequency conversion architectures, even-order intermodulation products are the most problematic, since they are located at baseband. Obviously, the predominant

intermodulation product will be the product 2·LO-2·RF. However, as previously commented, the spurious signal reject depends on the LO power level. This can be clearly seen from Fig. 3.35, where the power levels of the wanted signal (LO-RF) and the most significant even-order intermodulation product (2LO-2RF) are plotted for different values of LO power (P_{LO}). By selecting a LO power of 0 dBm instead of 7.5 dBm, the spurious signal reject improves 14 dB at 780 MHz, 28 dB at 2595 MHz, and 20 dB at 5786.5 MHz.

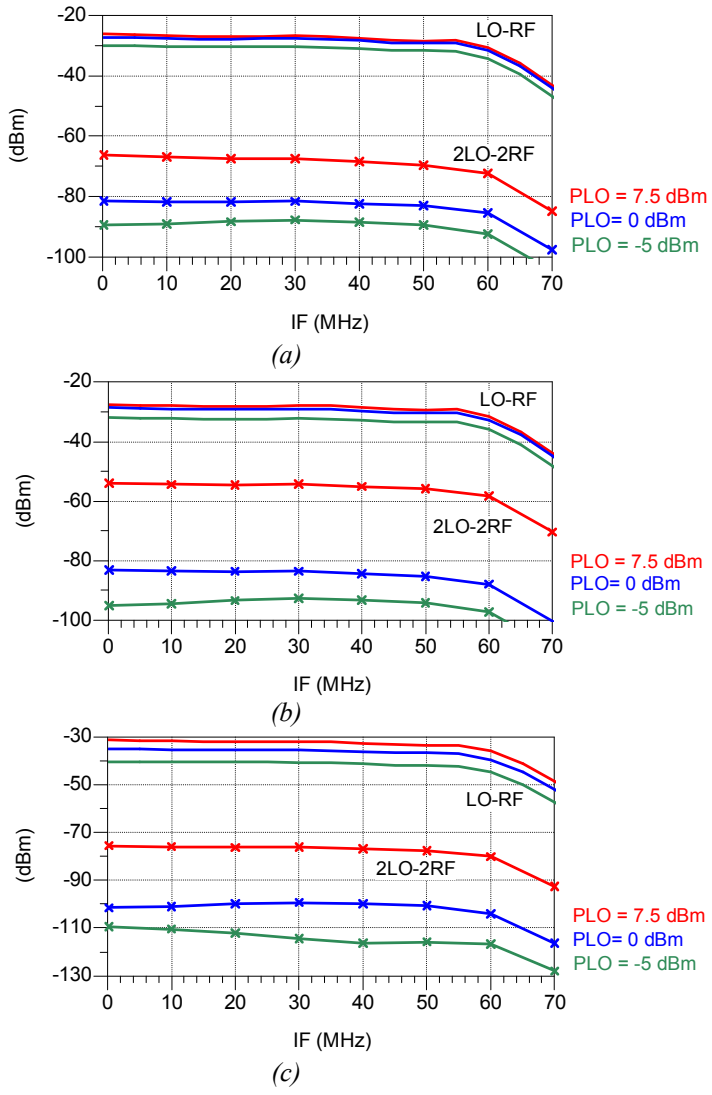

Fig. 3.35: Simulated power of the even-order intermodulation product (at output port 3): P_{RF}=-40 dBm, (a) f_{LO}=780 MHz, (b) f_{LO}=2595 MHz, (c) f_{LO}=5786.5 MHz.

Finally, the gain compression characteristic of the six-port receiver will be evaluated. Once again, the LO and RF signals will be 5 MHz separated in frequency,

and the LO power will be set to 7.5 dBm. The simulated gain compression curves, evaluated at port 3, are presented in Fig. 3.36. The simulated results give an output one-dB compression point (P_{1dB}) of 11.7 dBm at 780 MHz, 11.6 dBm at 2.595 GHz, and 9.2 dBm at 5.7865 GHz.

To sum up, the simulated six-port receiver performance is summarized in Table 3.4.

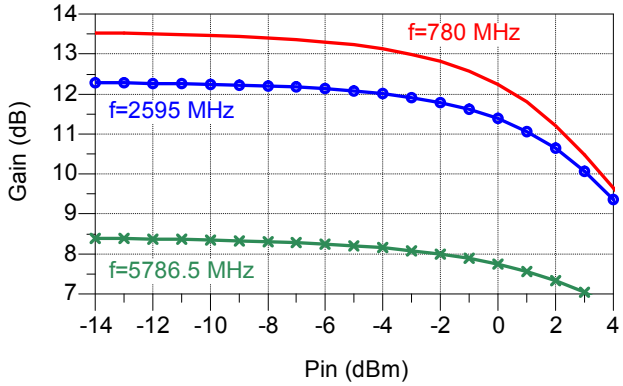

Fig. 3.36: Simulated gain compression curve (at output port 3): f_{LO} - f_{RF}=5 MHz, P_{LO}=7.5 dBm.

Table 3.4 Simulated six-port receiver characteristics, P_{LO}=7.5 dBm.

Parameter	Condition (MHz)	Value			Units
Max. Gain [1] DC-50 MHz	780 2595 5786.5	13.7 12.4 8.5			dB
f_{c3dB} [1]	780 2595 5786.5	58.5 58.7 58.1			MHz
Amplitude imbalance ΔA [2]	@ 5 MHz 780 2595 5786.5	Port 4 -0.73 0.15 -2.0	Port 5 -0.77 0.09 -0.5	Port 6 -1.14 0.86 -1.7	dB
Phase difference $\Delta\Phi$ [2]	@ 5 MHz 780 2595 5786.5	Port 4 180.8 172.5 182.9	Port 5 101.2 89.5 98.9	Port 6 -86.5 -82.6 -83.0	Deg.
Output P_{1dB} [1]	780 2595 5786.5	11.7 11.6 9.2			dBm
Spurious reject @-40 dBm [1]	780 2595 5786.5	P_{LO}=7.5 dBm 39.9 26.4 44.1	P_{LO}=0 dBm 54.2 54.5 63.8		dB

[1] Evaluated at port 3.
[2] With respect to reference port 3.

3.4 IMPLEMENTATION AND EXPERIMENTAL CHARACTERIZATION

In this section, the different fabricated circuits and their experimental characterization are presented. The measured performance of the overall six-port receiver prototype is also included.

3.4.1 90-degree hybrid coupler

Fig. 3.37 illustrates a photograph of one of the three fabricated 3dB tandem couplers. The stripline structure is composed of an 1143-380-1143 sandwich of 2.17 Cu-Clad substrate, where metallization lines are printed on the top and bottom side of the central layer in order to reduce alignment errors. The dimensions of the fabricated 3dB tandem coupler are 130x17x2.6 mm^3.

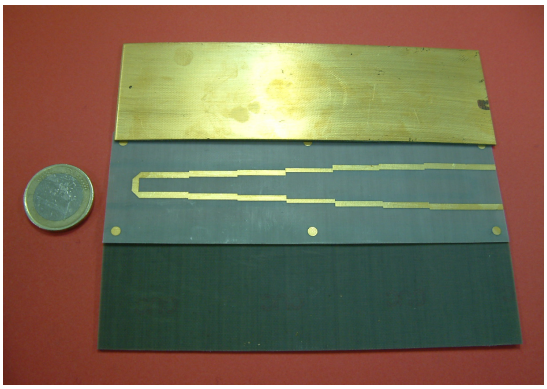

Fig. 3.37: Photograph of the 3 dB tandem coupler in stripline technology.

The three fabricated 3dB tandem couplers have been assembled over a metallic structure, as shown in Fig. 3.38, which allows us to measure the response of each coupler separately. Later on the three tandem couplers will be interconnected by external coaxial cables to form the six-port network.

The couplers have been characterized with good performance. The figures Fig. 3.39-Fig. 3.42 present both simulated and measured amplitude and phase frequency responses of the 3dB tandem coupler. The results show a very good agreement between the simulated and measured responses. Input return loss and isolation are better than 15 dB over the entire bandwidth. The maximum phase imbalance is 4º, and the maximum amplitude imbalance is 1.2 dB.

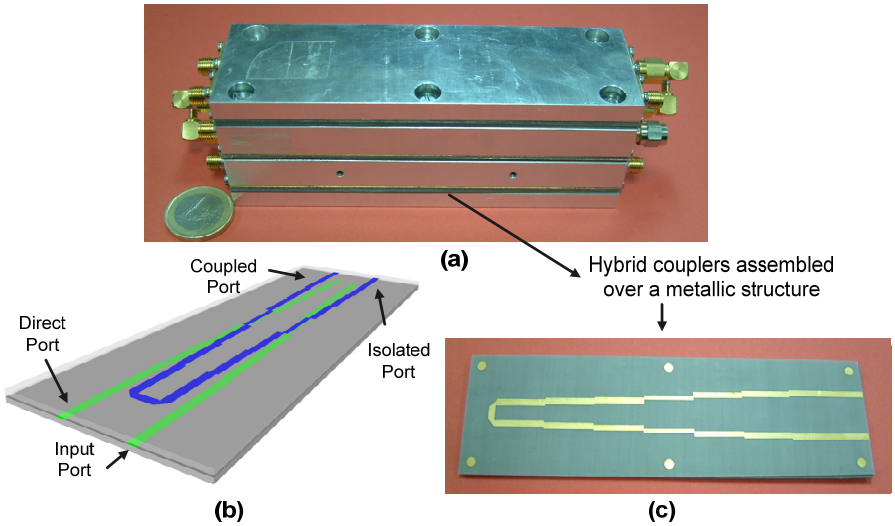

Fig. 3.38: Assembly of the three tandem couplers (a) External appearance, (b) 3D view of the 3dB tandem coupler, (c) Top view of the 3dB tandem coupler.

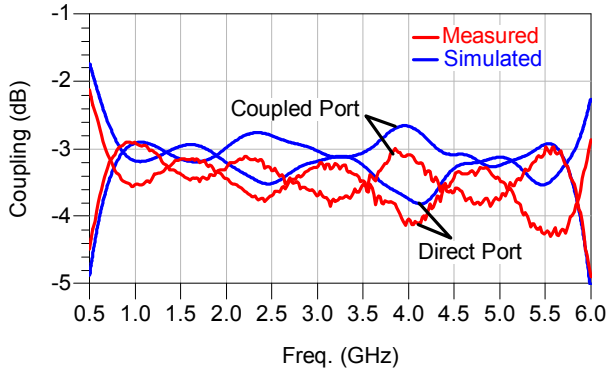

Fig. 3.39: Simulated and measured coupling of the stripline 3 dB tandem coupler.

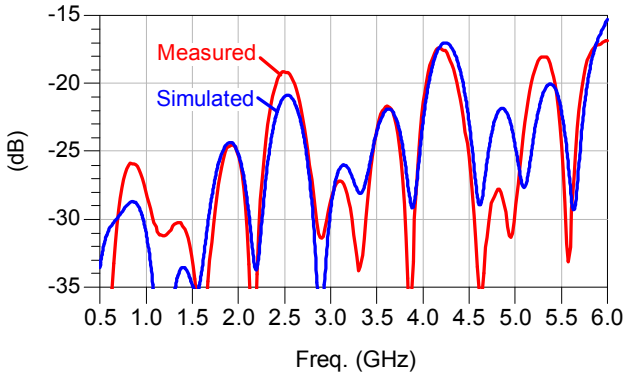

Fig. 3.40: Simulated and measured input return loss of the stripline 3 dB tandem coupler.

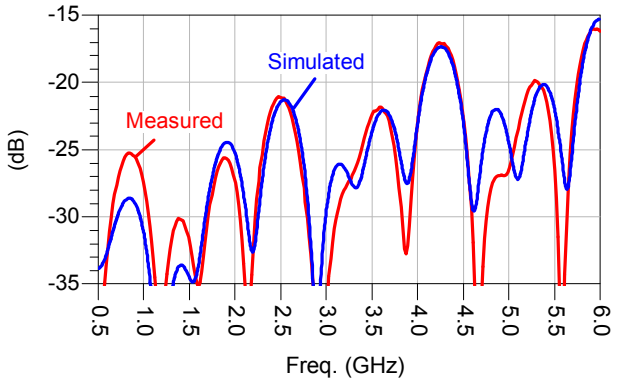

Fig. 3.41: Simulated and measured isolation of the stripline 3 dB tandem coupler.

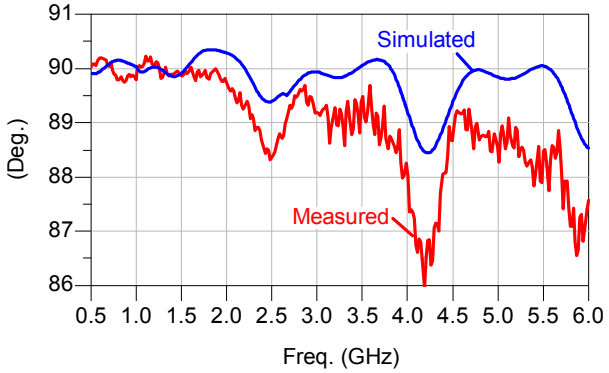

Fig. 3.42: Simulated and measured phase difference between coupled and direct ports of the stripline 3 dB tandem coupler.

3.4.2 Power divider

The photograph of the LYNX 111.A0214 power divider is shown in Fig. 3.43. Its measured response appears in Fig. 3.44, Fig. 3.45, and Fig. 3.46. Note that the measured characteristic of the power divider is better to that provided by the manufacturer (see section 3.2.1.2). In particular, the measured input return loss is below 20 dB, instead of the 15 dB stated by the manufacturer; the measured amplitude imbalance is better to the given 0.2 dB; and the maximum phase imbalance is only 3º. Taking into account that the power divider parameters given by the manufacturer were considered for the simulations, the measured response of the six-port network will be better to that envisaged in the simulations, as it will be seen in the next section.

Fig. 3.43: Photograph of the LYNX 111.A0214 power divider.

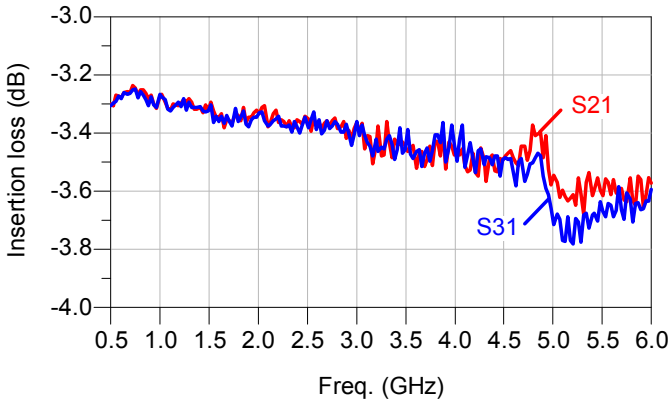

Fig. 3.44: Measured insertion loss of the power divider.

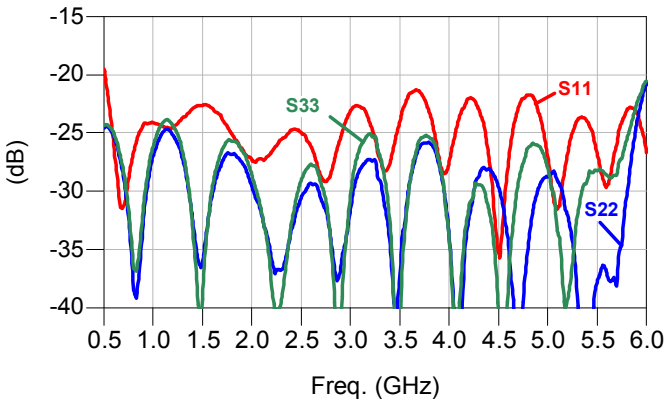

Fig. 3.45: Measured return loss of the power divider.

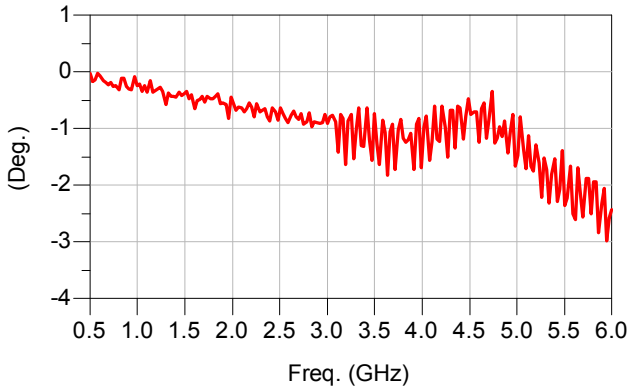

Fig. 3.46: Measured phase imbalance of the power divider.

3.4.3 Six-port network

The six-port network prototype can be seen in Fig. 3.47. The three 3 dB couplers are interconnected by external coaxial cables, which must have the same length in order to preserve the six–port phase behaviour. The power divider is connected to the couplers by two coaxial cables of the same length. However, the two cables connecting the power divider to the couplers do not have to be identical in length to the cables interconnecting the couplers, since what it has to be maintained is the four relative phase shifts of 0, $\pi/2$, $-\pi/2$, and π rad. It will only produce a linear variation with frequency of the absolute phases, which will be compensated by the calibration.

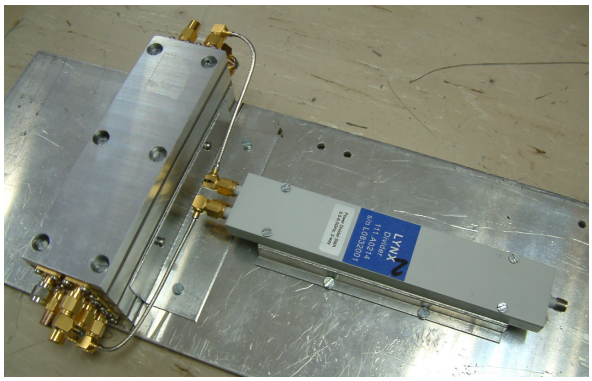

Fig. 3.47: Six-port network physical realization.

Fig. 3.48 illustrates both simulated and measured input return loss. It can be seen that the measured return loss at the LO port are better to the simulated results, since the real return loss of the power divider resulted to be better than the specified

value in the simulations (see section 3.2.1.3). The measured return loss at the RF port is below -20 dB up to 2.4 GHz, and below -16 dB from 2.4 GHz to 6 GHz. Moreover, simulated and measured isolation curves, presented in Fig. 3.49, bear strong resemblance. Measured isolation is better than 20 dB over the whole bandwidth.

The attenuations from LO and RF ports to output ports are shown in Fig. 3.50, and Fig. 3.51, respectively. Ideally, these attenuations are 6 dB. The measured attenuation curves present a loss factor that increases with the increase of frequency, due to the interconnection coaxial cables and the power divider insertion loss. These effects were not introduced into the simulations, thereby the additional losses observed in the measurement results with respect to Fig. 3.13 and Fig. 3.14.

To analyse the six-port network phase behaviour, we will define the parameter $\Delta\Phi_{Pi}$ as the phase difference between S_{i1} and S_{i21}, with i=3,…,6. According to the chosen six-port topology, $\Delta\Phi_{Pi}$ parameters must be 180º, 90º and -90º phase shifted each other. The phase shifts referred to $\Delta\Phi_{P3}$ are presented in Fig. 3.52. Once again, the simulated and measured phase responses differ due to the difference between the specified and measured phase response of the power divider. Measured results show a maximum error of 10º compared to the theoretical behaviour.

Finally, the six-port performance will be analyzed in terms of the q_i-points. Remember that the design criterion of a six-port junction consists of achieving a good distribution of the q_i-points. In general, the closer the magnitudes of q_i, and the larger the differences between the arguments of q_i, the better will be the performance of the circuit. When the RF and LO input ports are completely isolated, the equivalent q_i-points of the six-port network can be expressed in terms of scattering parameters as [125]:

$$q_i = \frac{s_{i1}}{s_{i2}} \tag{3-20}$$

Ideally, in our six-port network topology the magnitudes of q_i-points are equal to 1, and the arguments differ 90 degrees. The measured q_i-points of the developed six-port network satisfactorily fulfill these requirements, as it can be seen in Fig. 3.53. Note that the measured arguments of q_i are not absolute 0º, 180º, 90º, and -90º. In fact, Fig. 3.52 represents the arguments of q_i with port 3 as reference port. Remember that the two cables connecting the power divider to the couplers are not identical in length to

the cables interconnecting the couplers. Therefore, a linear variation with frequency in the arguments of q_i is observed. However, as previously commented, this is not a problem, provided that a 90º relative phase shift between the arguments of q_i is kept. It only produces an additive phase offset dependent on frequency, which will be compensated by the calibration. The magnitudes of q_i are in the range of 0.7 to 1.5 from 500 MHz to 6 GHz, and the maximum error in the relative phase differences is 10º over the theoretical 90º. Therefore, according to [73]-[74], the operating frequency range of the six-port network could be enlarged, as the six-port network is said to provide good results even when the ratios of the magnitudes of q_i are greater than 4, and their arguments differ an amount smaller than 25º.

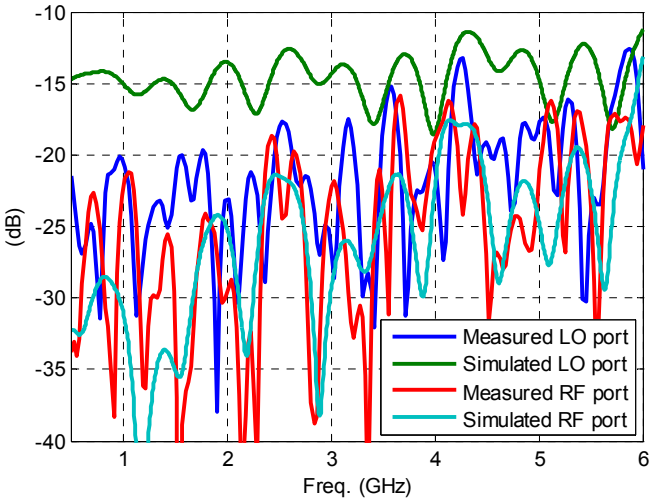

Fig. 3.48: Simulated and measured input return loss of the six-port network.

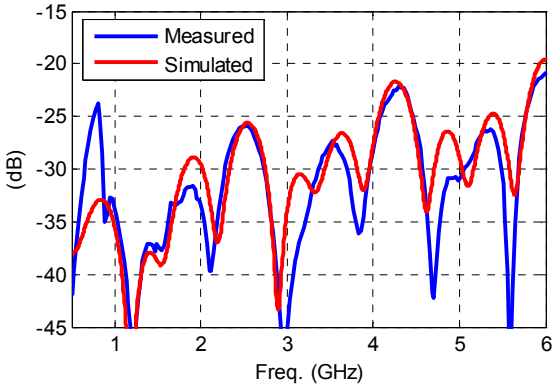

Fig. 3.49: Simulated and measured isolation of the six-port network.

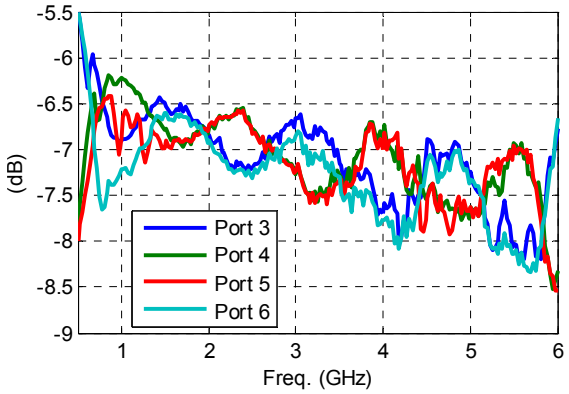

Fig. 3.50: Measured attenuation from LO port to output ports of the six-port network.

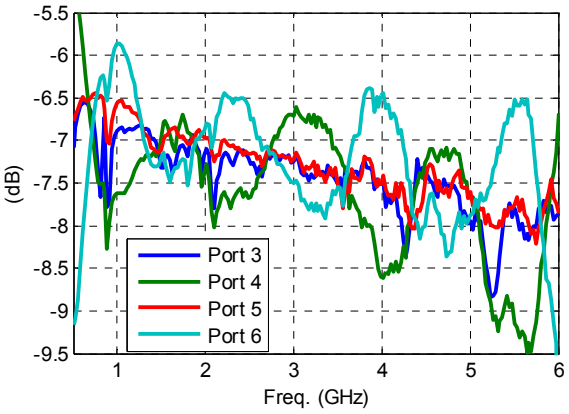

Fig. 3.51: Measured attenuation from RF port to output ports of the six-port network.

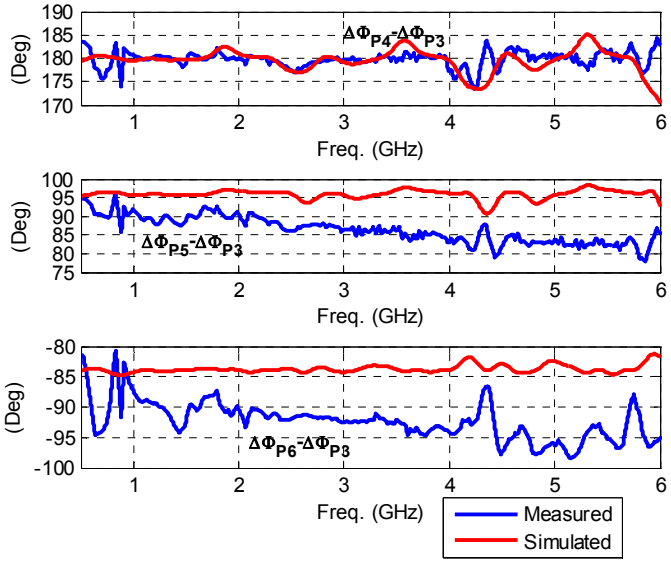

Fig. 3.52: Simulated and measured phase response of the six-port network.

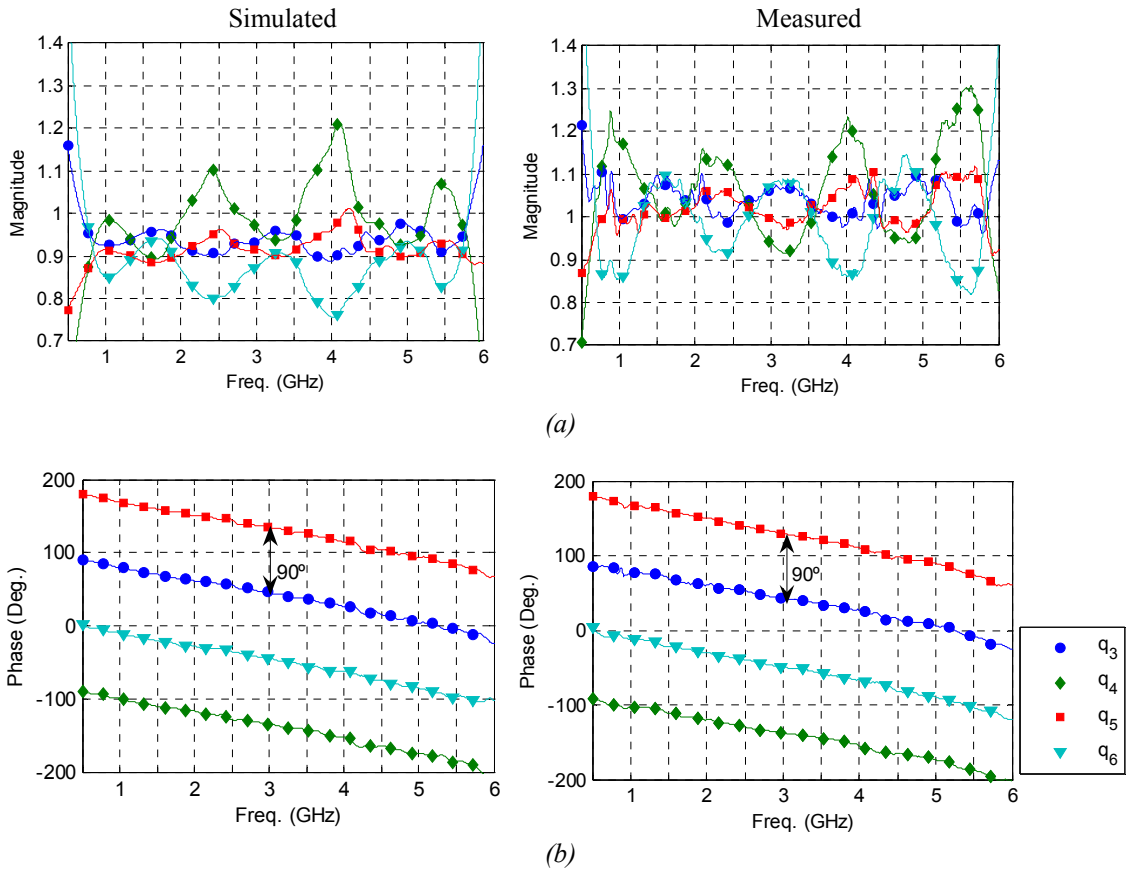

Fig. 3.53: Simulated and measured q_i-points of the six-port network (a) Magnitudes (b) Phases.

3.4.4 Complete six-port receiver

Fig. 3.54 illustrates the fabricated six-port receiver prototype. The six-port receiver performance has been measured over the 0.5-6 GHz frequency band. The measured results are compiled in Table 3.5.

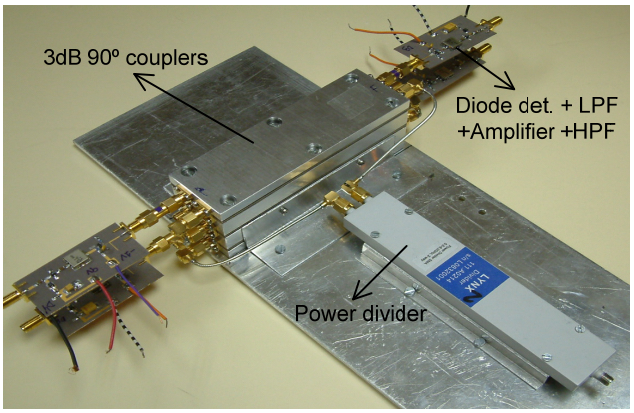

Fig. 3.54: Six-port receiver prototype.

Table 3.5 Measured six-port receiver characteristics, P_{LO}=7.5 dBm.

Parameter	Condition (MHz)	Value			Units
Max. Gain [1] DC-50 MHz	780	11			dB
	2595	7.4			
	5786.5	4			
f_{c3dB} [1]	780	42.1			MHz
	2595	42.5			
	5786.5	42.3			
Amplitude imbalance ΔA [2]	@ 5 MHz	Port 4	Port 5	Port 6	dB
	780	-0.58	-0.49	-0.16	
	2595	-1.35	-0.99	0.4	
	5786.5	-1.9	0.38	0.15	
	@ 10 MHz	Port 4	Port 5	Port 6	
	780	-0.36	-0.36	0.43	
	2595	0.17	-0.48	0.4	
	5786.5	-1.4	-0.15	-0.46	
	@ 20 MHz	Port 4	Port 5	Port 6	
	780	-0.39	-0.45	0.89	
	2595	-1.0	-0.22	0.76	
	5786.5	-1.88	0.46	-0.89	
Phase difference $\Delta\Phi$ [2]	@ 5 MHz	Port 4	Port 5	Port 6	Deg.
	780	162	85.6	-99	
	2595	160.2	84.2	-100.8	
	5786.5	180	70.5	-98.6	
	@ 10 MHz	Port 4	Port 5	Port 6	
	780	168.4	85.6	-109.4	
	2595	165.6	80.6	-109.4	
	5786.5	183.6	69.8	-97.9	
	@ 20 MHz	Port 4	Port 5	Port 6	
	780	184.3	86.4	-96.5	
	2595	175.7	80.6	-100.8	
	5786.5	158.4	61.9	-92.1	
Output P_{1dB} [3]	780	10.2			dBm
	2595	9.9			
	5786.5	10.15			
Input IP3 [3]	780	10.8			dBm
	2595	15.2			
	5786.5	3			
Spurious reject @-40 dBm	780	36			dB
	2595	54			
	5786.5	43			

[1] Measured at port 3.
[2] With respect to reference port 3.
[3] Measured at port 5.

3.5 SIX-PORT DEMODULATION PERFORMANCE

This section presents the validation of the developed six-port receiver as RF demodulator. The quality of the demodulated signal will be measured in terms of the Error Vector Magnitude (EVM). The EVM is a common figure of merit in digital communications [126], defined as the root-mean-square value of the difference between the measured and ideal symbols. The EVM expression is given by

$$\mathrm{EVM} = \sqrt{\frac{\sum_{n=1}^{N}\left(\mathrm{I}_{r,n}-\mathrm{I}_{i,n}\right)^2+\left(\mathrm{Q}_{r,n}-\mathrm{Q}_{i,n}\right)^2}{\sum_{n=1}^{N}\mathrm{I}_{i,n}{}^2+\mathrm{Q}_{i,n}{}^2}} \tag{3-21}$$

where I_r, Q_r are the I-Q components of the demodulated symbols; I_i, Q_i are the ideal I-Q components; and N is the number of symbols over which the EVM is calculated.

The test bench that will be used for the measurements is shown in Fig. 3.55. The Agilent E4438C ESG Vector Signal Generator (VSG) generates the RF modulated signal. The LO is the *Agilent* synthesized sweeper 83752A. Both generators are phase locked. The output signals of the six–port receiver are acquired by a four-channel oscilloscope (*Agilent Infiniium*), with an over–sampling ratio OSR=8. It is worth to mention that the maximum symbol rate that can be obtained with the E4438C ESG VSG is 12.5 Msymbol/s for an OSR=8. However, the six-port receiver demonstrator can operate with up to 100 MHz-wide signals, so it is expected to perform data rates of about 100 Msymbol/s.

The calibration and I-Q regeneration software, implemented in *Matlab,* is applied in a personal computer, which calculates the EVM using (3-21). The calibration method is a new and own real-time channelized auto-calibration algorithm based on training sequence, which has been developed for high-speed signal demodulation. It will be described in detail in section 5.2. In particular, we have applied the channelized auto-calibration method with N=4 filters and previous downsampling (downsampling ratio of 2). The software does not include any diode linearization technique.

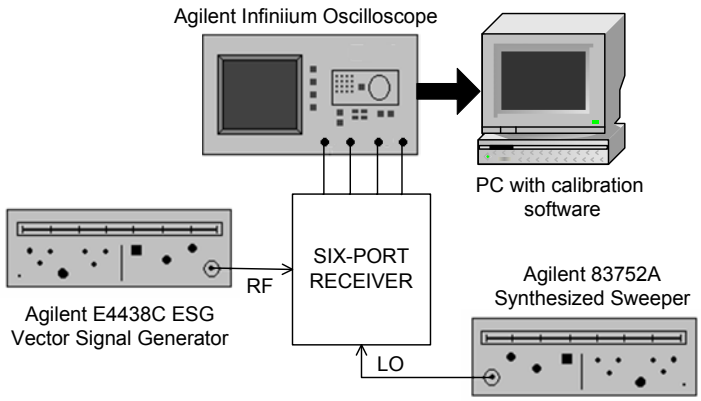

Fig. 3.55: Set-up of the six-port receiver test-bench.

3.5.1 Multi-mode and multi-band behaviour

With the purpose of demonstrating the multi-mode and multi-band characteristics of the SDR six-port receiver, we have measured the EVM for different modulation schemes and frequency bands. We have selected several frequencies corresponding to communication standards, such as GSM (900 MHz, 1800 MHz), PCS (1900 MHz), Wi-Fi (2.45 GHz), or WiMAX (700 MHz, 3500 MHz, 5800 MHz). The modulation schemes are QPSK, 16-QAM, and 64-QAM. The LO power is fixed to P_{LO}=0 dBm, and the input power is P_{in}= –20 dBm. For frequencies below 3 GHz, we have changed the VSG for the *Agilent* N5182A MXG, which can provide a symbol rate of 15.625 Msymbol/s for OSR=8. Therefore, it is possible to achieve a bit rate of 93.75 Mbps for a 64-QAM modulation. In all cases, we have acquired a total of 1000 symbols (8000 samples), which have been processed as bursts of length 200 symbols. The first 50 symbols of each burst are used for calibrating.

The measured values of EVM are presented in Table 3.6. These results show a good performance of the six–port receiver for high data rates over a four-octave frequency range. For example, the typical minimum BER specification of 10^{-3} corresponds to an EVM below 32.4 % for QPSK, 15 % for 16-QAM, and 7.5 % for 64-QAM. More strict specifications, such as those required for WiMAX reception, establishes a minimum BER of 10^{-6}, which means an EVM below 21 % QPSK, 9.5 % for 16-QAM, and 4.7 % for 64-QAM. The relation between BER and EVM can be seen in Fig. 3.57.

Table 3.6 Measured EVM, P_{LO}=0 dBm, P_{in}=-20 dBm.

Frequency (MHz)	Modulation	Bit Rate (Mbps)	EVM (%)
300	64-QAM	75	6.1
700	16-QAM	62.5	4.8
900	64-QAM	93.75	4.7
1800	QPSK	31.25	4.7
1900	16-QAM	62.5	4.6
2450	64-QAM	93.75	4.5
3500	16-QAM	50	4.4
4000	QPSK	25	4.5
5800	64-QAM	75	4.3
6000	QPSK	25	4.4

As it was previously stated in section 3.4.3, the operating frequency range of the six-port network could be enlarged due to its good frequency response. In effect, the results shown in Table 3.6 demonstrate that the six-port operating range can be extended from 300 MHz to 6 GHz (4.32 octaves) with good performance, although it was designed to cover the frequencies from 698 MHz to 5850 MHz. From theoretical analysis based on the measured six-port response, it is derived that the six-port operation could be extended also beyond 6 GHz. However, it has not been experimentally demonstrated due to test equipment limitations.

3.5.2 Operation with low LO power levels

An important advantage of the six-port architecture is its operation with low LO power levels. This means low power consumption, better RF-LO isolation, and reduction of the LO self-mixing, which is one of the main problems of zero-IF architectures. On the contrary, mixers used in conventional zero-IF receivers require high LO powers.

In order to demonstrate this characteristic, we have measured the EVM for different values of P_{LO}, keeping the input power level at P_{in}=–20 dBm. We use a 25 Mbps QPSK modulated signal (α=0.3). Again, the first 50 symbols of each data burst (length 200 symbols) are used to auto-calibrate the system and regenerate the I-Q components of the next 150 data symbols. Fig. 3.56 shows the constellation diagrams of the demodulated signal for 700 MHz, 3 GHz, and 6 GHz. The obtained values of EVM are compiled in Table 3.7. These results prove that six-port receivers can operate for low LO power values.

Nevertheless, a suitable selection of the LO power level is required. A study of the optimal LO power for maximizing the SNR at the baseband outputs is presented in [127]. When the phase noise contribution is not considered, thermal and shot noises are the dominant sources of distortion, and a maximum SNR of 33 dB is achieved for LO powers in the range of 3-7 dBm. Considering the phase noise contribution, the maximum value of SNR, corresponding to a LO power range from –7 to –2 dBm, decreases 14 dB. However, the maximum diode conversion efficiency is achieved for high LO power levels, around 13 dBm. These figures are obtained from the simulation results of [127], although similar values would be obtained in our case. The spurious signal rejection as a function of the LO power must also be considered.

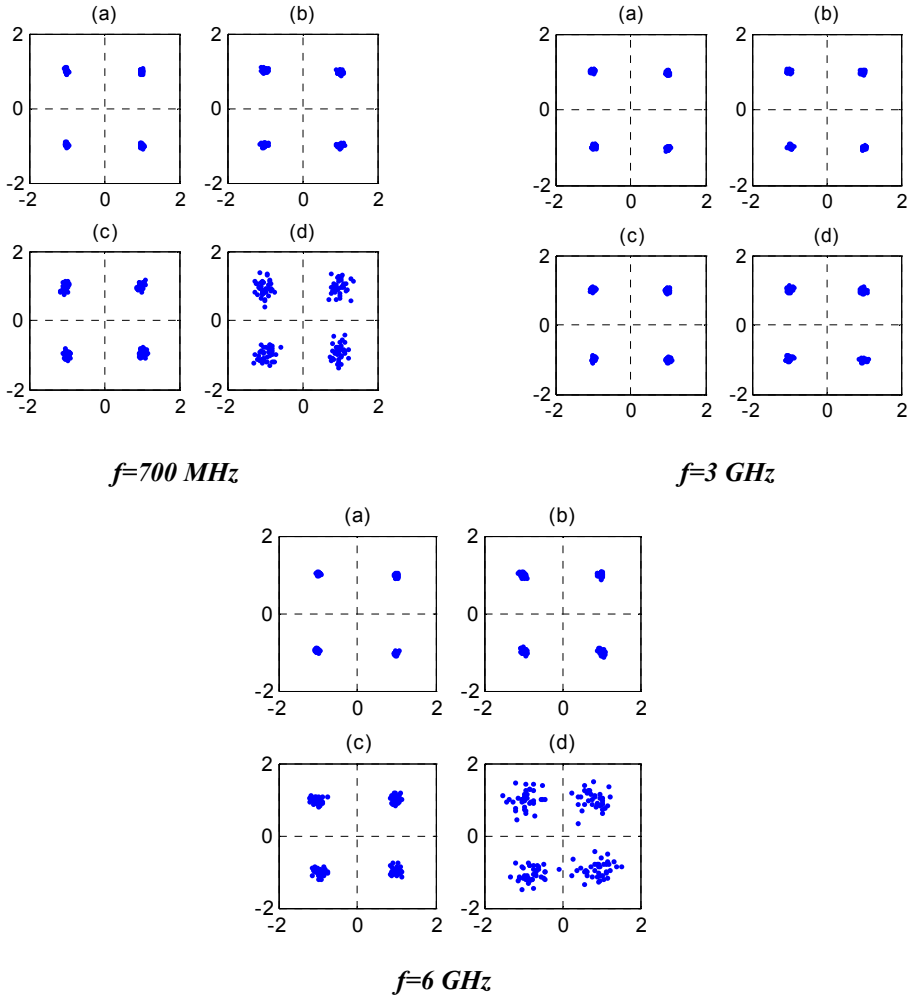

Fig. 3.56: Constellation diagrams for 25 Mbps QPSK, P_{in}=–20 dBm (a) P_{LO}=5 dBm (b) P_{LO}=0 dBm (c) P_{LO}=–10 dBm (d) P_{LO}=–20 dBm.

Table 3.7 Measured EVM versus P_{LO}, 25 Mbps QPSK.

EVM (%)	Frequency		
	700 MHz	***3 GHz***	***6 GHz***
P_{LO}=5 dBm	3.5	3.9	3.7
P_{LO}=0 dBm	4.5	3.8	4.7
P_{LO}=-10 dBm	7.6	4.1	8.8
P_{LO}=-20 dBm	18	5.2	26.3

(*) *Calculated from 150 received symbols.*

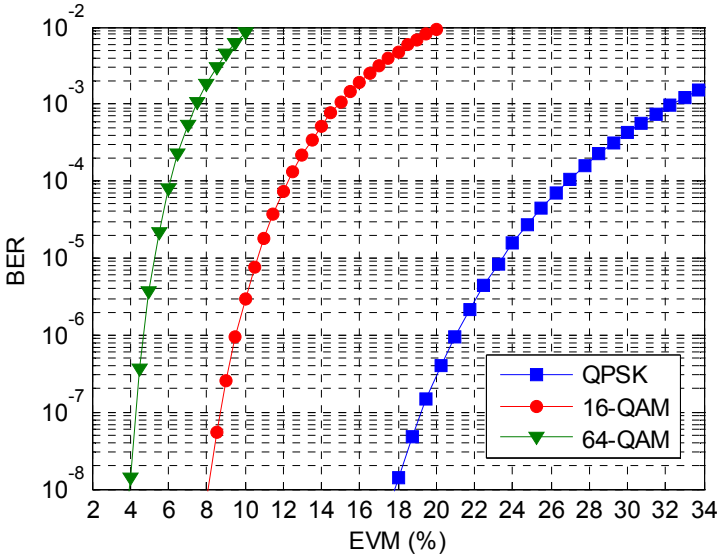

Fig. 3.57: Theoretical BER versus EVM curves.

3.5.3 Comparison of multi-port demodulators

To conclude, the comparison with other multi-port demodulators operating in the frequency range of interest is presented in Table 3.8. As the quality of the demodulated signal is evaluated in terms of EVM or BER, we provide the theoretical BER versus EVM curves for QPSK, 16-QAM and 64-QAM modulation schemes in Fig. 3.57 [126].

The six-port receiver is said to be a good solution for the multi-band demodulation of high-speed signals, but no many experimental demodulation results proving both assumptions have been published up to now. Some published works are not strictly multi-band [92],[104]; other are multi-band but only validate the demodulator for a single frequency [102],[106]; and other prove the multi-band behaviour but do not quantify the quality of the demodulated signal [101]. In [100],[105] the demodulation performance is quantified over the entire operating frequency range, but with data rates much lower than in our experiments. Recently, a

six-port demodulator supporting a 1.67 Gbps data rate has been published [21]. However, this is not a broadband design, as it only covers the range from 7 to 8 GHz. In addition, the measured EVM is quite high, even though the high LO power level (15 dBm). Our six-port receiver has been validated over a four octave bandwidth (0.3-6 GHz), and for up to 93.75 Mbps data rates with low values of EVM. It outperforms the other designs in terms of bandwidth and quality of the demodulated signal.

Table 3.8 Comparison of multi-port demodulation performances.

Ref.	Operating freq. band (GHz)	Measurement results				
		Data signal	P_{LO} (dBm)	P_{in} (dBm)	Freq. (GHz)	Quality of demodulated signal
[100] (2003)	0.9-5	97.2 Kbps QPSK	0	-20	0.9-4	EVM<14 %
[92] (2004)	2-3	200 Kbps QPSK	0	-62.5	2	BER=10^{-3}
[101] (2006)	2-9.4	8PSK	-	-19 -27 -31	2.4 5.8 9.4	Not quantified
[102] (2006)	0.9-4	1 Mbps QPSK	-10	-15	2.45	EVM=12 %
[104] (2008)	3.1-4.8	1 Mbps QPSK	-1.5	-	3.432 3.96 4.488	EVM=5.5 % EVM=4 % EVM=6.3 %
[105] (2009)	0.8-2.4	4 Mbps 16-QAM	-8.5	-33.3 to -2.6 -39.6 to -0.6 -38 to -0.7	0.8 1.6 2.4	BER<10^{-3}
				≈ -32	1.6	BER=10^{-6}
[106] (2010)	0.9-4	400 Kbps QPSK	-10	-20 -40	2.45	EVM=5.9 % EVM=7.9 %
[21] (2010)	7-8	1.67 Gbps 16 QAM	15	-15	7.5	EVM=10.9 %
This work (2011)	0.3-6	75 Mbps 64-QAM	0	-20	0.3	EVM=6.1 %
		62.5 Mbps 16-QAM			0.7	EVM=4.8 %
		93.75 Mbps 64-QAM			2.45	EVM=4.5 %
		25 Mbps QPSK	0	-20	6	EVM=4.4 %
			-20		1.8	EVM=6.3 %

3.6 SUMMARY

The six-port architecture reemerges from the search of low-cost, multi-band and multi-standard transceivers. Its inherent advantages, especially its broadband behavior, make this a structure a good candidate to implement a SDR.

In this chapter, we have presented a SDR six-port receiver prototype for broadband and high data rates applications. The system has been designed and measured with good performance. The demodulation capabilities of the developed six-port receiver have been demonstrated over the frequencies of the main communication standards, from 0.3 GHz to 6 GHz. The prototype has been validated for data rates of 93.75 Mbps (limited by the test instruments), although it has been designed to operate with 100 MHz instantaneous bandwidth, so a bit rate of 600 Mbps for a 64-QAM modulation is foreseen. Our work demonstrates empirically and quantitatively the multi-band behaviour of the six-port architecture, and the capability of performing high data rates.

The contents of this chapter have been published in several media. The design and measurement of the six-port network was presented in the *IEEE 2010 European Microwave Conference* [EuMC 2010]. The overall SDR six-port receiver and the demonstration of its multi-mode, multi-band, and high-speed demodulation capabilities were presented in the *IEEE 2010 Military Communications Conference* [MILCOM 2010], and published in the Journal *Progress in Electromagnetics Research* [PIER 2011].

Chapter 4

COMPARISON BETWEEN SIX-PORT AND CONVENTIONAL RECEIVERS

4.1 INTRODUCTION

Chapter 2 expounded the main characteristic of three RF architectures suitable for SDR. Nevertheless, a complete analysis of the studied RF architectures also entails an experimental comparison based on measured data. It is the purpose of this chapter to compare, by means of experimental results, the performance of six-port, zero-IF, and low-IF techniques. Consequently, a zero-IF/low-IF receiver prototype has been also implemented, which will be described below.

First of all, to have a global picture of the homodyne, heterodyne and six-port techniques, let us see Table 4.1. It gives a parameter-oriented comparison of performances for those architectures based on diode-enabling receivers [128]. It can be seen that the emerging multiport techniques are able to excel in many aspects, in particular, the low LO requirement in terms of power and frequency stability. However, multiport architectures do not present good behaviour as for dynamic range, compared with heterodyne and conventional homodyne receivers. The main reason is that six-port implementations typically use zero-bias detector diodes, while the square-law dynamic range is maximized by biasing the detector diode. In our diode detector design, however, a high bias current was selected in order to extend the dynamic range. Then, a better dynamic range performance is expected in our six-port receiver prototype.

Table 4.1 Performance comparison of heterodyne, homodyne and multi-port techniques (with reference to diode-based receiver architectures) © 2010 IEEE [128].

Parameter	Heterodyne	Homodyne	Six-port
Dynamic range	Excellent	Good	Average
LO power and freq. stability	Average	High	Low
Signal sensitivity	Excellent	Good	Good
Harmonic control	Difficult	Average	Easy
IP3	Average	Good	Excellent
Port-to-port isolation	Difficult to achieve	Average	Easy to achieve
Conversion loss	Good	Good	Excellent
Noise figure	Excellent	Good	Average
Structure complexity	High	Low	Average
Wideband/multiband flexibility	Average	Good	Excellent

4.2 ZERO-IF/LOW-IF RECEIVER PROTOTYPE

As the block diagrams of zero-IF and low-IF configurations are quite similar (see Fig. 2.1 and Fig. 2.3), a single receiver prototype for both architectures has been developed. The zero-IF/low-IF receiver has been designed to cover the frequency range from 2500 MHz to 2690 MHz. Channel bandwidth can be selected from 1 MHz to 20 MHz.

The block diagram of the implemented prototype is shown in Fig. 4.1. The RF signal is amplified by a LNA (*Low Noise Amplifier*), and then it is introduced into an I-Q demodulator. A low-pass filter, a video amplifier and a high-pass filter for DC-offset cancellation are located at each output. The RF band-pass filter has not been included in the prototype. An automatic gain control (AGC) stage would be necessary in a SDR front-end as well.

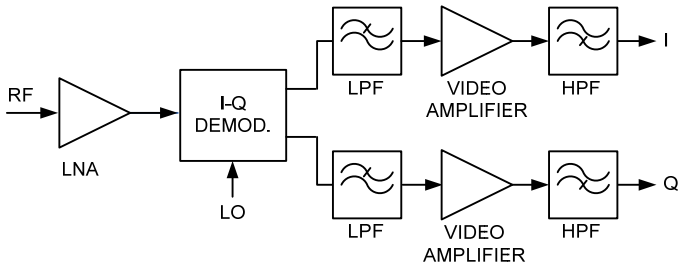

Fig. 4.1: Block diagram of the zero-IF/low-IF receiver.

The prototype, presented in Fig. 4.2, has been implemented in microstrip technology (ε_r=2.17 Cu-clad substrate). The LNA is the Mini-Circuits PMA-545+ model, and the LT5575I-Q is used for the I-Q demodulator. The bandwidth of the low-pass filter, (SXLP-21.4+ Mini-Circuits) is 22 MHz. Notice that for the zero-IF architecture, a 10 MHz low-pass filter is sufficient to receive 20 MHz-wide channels, but the low-IF receiver requires double bandwidth for the IF stage. The video amplifier is the MAR-8A+. DC-offset cancellation, needed for zero-IF, is achieved by means of high-pass filtering with a series capacitor (1 KHz cut-off frequency).

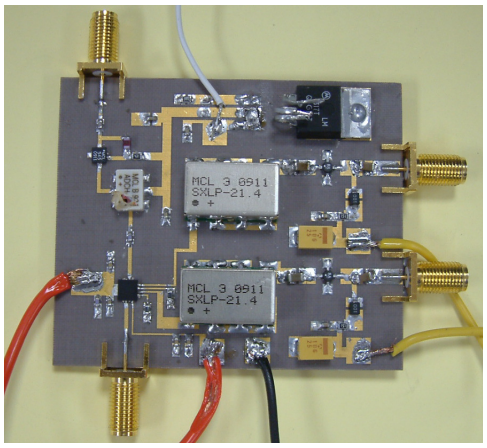

Fig. 4.2: Zero-IF/low-IF receiver prototype.

4.3 MEASUREMENT RESULTS

The experimental comparison of the developed receiver prototypes will be presented in this section. The quality of the demodulated signal will be measured in terms of the EVM (see section 3.5).

The configuration of the test-bench, represented in Fig. 4.3, is described next. The Agilent E4438C ESG Vector Signal Generator (VSG) generates the RF modulated signal. The local oscillator is the Agilent synthesized sweeper 83752A. Both generators are phase locked. The output signals of the receiver are acquired by the *Agilent Infiniium* Oscilloscope with an over-sampling ratio OSR=8. The software, implemented in *Matlab*, is applied in a personal computer to regenerate the I-Q components of the original signal. For the six-port receiver calibration, it has been used the conventional six-port auto-calibration method based on training sequence, which is described in section 2.4.4.1. In this case, we have not used our own

channelized auto-calibration method (see section 5.2), since it carries out a frequency channelization to maximize the quality of the demodulated signal and, therefore, the prototypes would have not been compared under the same conditions.

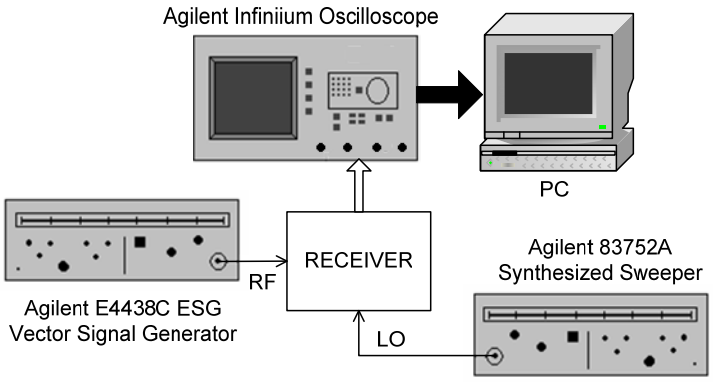

Fig. 4.3: Set-up of the measurement test-bench.

4.3.1 Performance comparison

Firstly, the EVM will be measured and compared for the three architectures. As the six-port receiver prototype does not include a LNA, it has been bypassed in the zero-IF/low-IF prototype, in order to measure the architectures at the same conditions. A 2595 MHz signal with a filtered 64-QAM modulation (0.3 roll-off square-root-raised cosine filter) is used. The LO power is P_{LO}=0 dBm, and the RF power (P_{in}) varies from -45 to 0 dBm (take into account that the LNA is not included). The LO frequency is 2595 MHz for zero-IF and six-port receivers; in the case of low-IF, it is selected to achieve a lower IF of 2 MHz. EVM is calculated after the acquisition of 1000 symbols (8000 samples, OSR=8).

Fig. 4.4 shows the measured EVM for a symbol rate of 5 Msymbol/s (30 Mbps). On one hand, six-port receiver has larger dynamic range than the other architectures due to the high dynamic range detector design, with an EVM below 7.5% from -45 dBm to 0 dBm. The measured values of EVM are bellow 7.5 % from -32 dBm to -11.5 dBm for the low-IF receiver, and from -38.5 dBm to -3.5 dBm for the zero-IF receiver. On the other hand, the minimum value of EVM is obtained with the low-IF architecture (2% for P_{in}=-20 dBm). Zero-IF receiver has a minimum EVM of 4.2 % for P_{in}=-20 dBm. For the six-port receiver the minimum value of EVM is 3.8 %, obtained with P_{in} = -25 dBm. These results are as we expected, as the low-IF

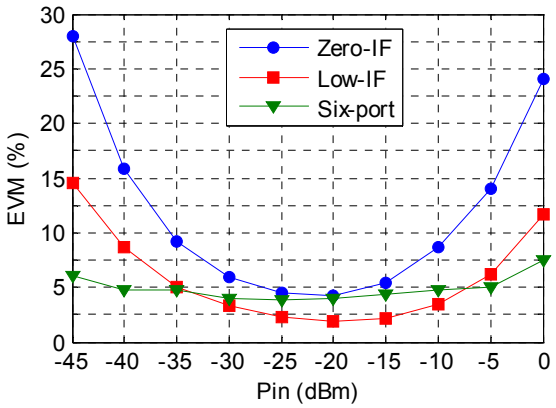

Fig. 4.4: Measured EVM versus Pin: 2595 MHz, 30 Mbps 64-QAM, P_{LO}=0dBm.

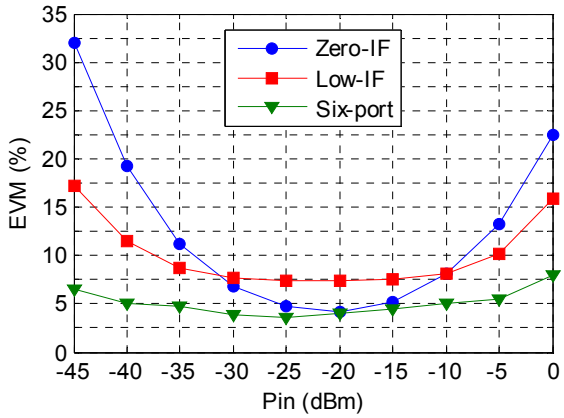

Fig. 4.5: Measured EVM versus Pin: 2595 MHz, 75 Mbps 64-QAM, P_{LO}=0 dBm.

architecture does not have DC-offset and flicker noise problems, whereas the 5 Msymbol/s RF signal is down-converted to a 0-3.25 MHz IF in the direct conversion architectures.

The measurement has been repeated for a wider RF signal. The maximum symbol rate that can be obtained with the VSG is 12.5 Msymbol/s (75 Mbps) for an OSR=8, although the zero-IF/low-IF and the six-port receivers theoretically support 20 MHz and 100 MHz channels, respectively. The measured EVM for a data rate of 75 Mbps is presented in Fig. 4.5. In this case, low-IF presents worse results. The reason is that the IF response curves of the zero-IF/low-IF prototype drop from 15 MHz, as it can be seen in Fig. 4.6, and the 12.5 Msymbol/s RF signal is down-converted between 2 MHz and 18.25 MHz in low-IF configuration. For the zero-IF and six-port receivers, where the signal is down-converted to a 0-8.125 MHz IF, the values of EVM are very

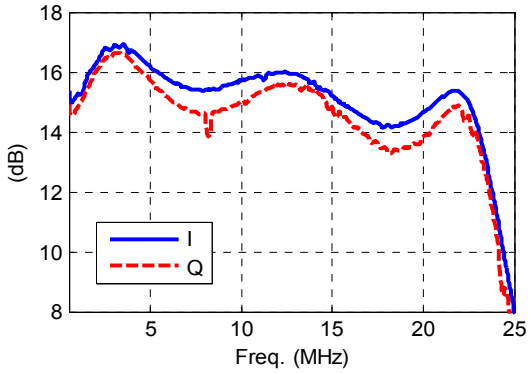

Fig. 4.6: Measured IF response of the zero-IF/low-IF receiver.

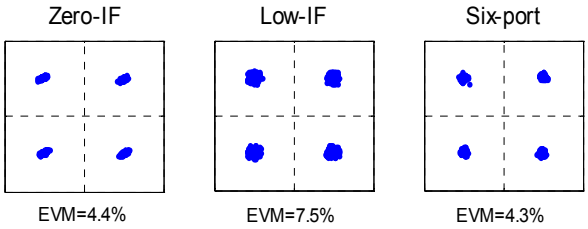

Fig. 4.7: Constellation diagrams: 2595 MHz, 25 Mbps QPSK, Pin=-25 dBm, P_{LO}=0 dBm.

similar to that obtained with 5 Msymbol/s. This proves that the low-IF architecture demands more bandwidth and stricter I-Q balance requirements than the direct conversion scheme. Digital equalization and I-Q imbalance compensation techniques can be applied to solve these problems [58]-[60].

The receiver prototypes have been also validated for other types of modulation schemes with similar results. Fig. 4.7 shows the constellation diagrams obtained after the demodulation of a 2595 MHz QPSK signal (0.3 roll-off square-root-raised cosine filter), with a symbol rate of 12.5 Msymbol/s. The LO power is P_{LO}=0 dBm, and the RF input power is P_{in}=-25 dBm.

4.3.2 Influence of the image frequency in low-IF

Secondly, the effects of the image frequency on the low-IF receiver will be analyzed. The combination of a 2595 MHz 5 Msymbol/s 64-QAM signal and a 2584.5 MHz tone are introduced in the low-IF receiver. The LO power is P_{LO}=0 dBm, and its frequency is fixed to 2589.75 MHz to achieve a lower IF of 2 MHz. After the acquisition of 1000 symbols (8000 samples, OSR=8), the EVM is calculated for

different image attenuation values. Measurements results are collected in Table 4.2. Signal quality degradation is low for image power levels below the desired signal power. Degradation starts being significant for equal RF and image power levels. When the image signal power is higher than the desired signal power, the EVM rises to such high values as 10.7 % for an image attenuation of -10 dB. I-Q imbalance compensation algorithms must be applied, as I-Q imbalances decrease the image-reject capabilities of the front-end [58]-[60].

Table 4.2 Influence of image frequency on low-IF.

Image Attenuation (dB)	EVM (%)
-10	10.7
0	2.9
10	2.5
20	2.4
30	2.3
40	2.1

4.3.3 Influence of the LO power level

Finally, the influence of the LO power will be studied. Remind that one of the advantages of the six-port architecture is its operation with low LO powers. In order to prove that characteristic, the EVM as a function of P_{LO} will be measured for the three architectures. In this case, a 2595 MHz QPSK modulated signal (0.3 roll-off square-root-raised cosine filter) is used. The symbol rate is 5 Msymbol/s (10 Mbps). The input power level is kept at P_{in}=-20 dBm. Fig. 4.8 shows the EVM curves for P_{LO} values of 7, 0, -10, and -20 dBm. EVM is calculated over 1000 demodulated symbols. The six-port receiver performance keeps more stable versus P_{LO} variation, with an EVM increase of 0.6 points in percentage from 7 dBm to -20 dBm. Signal quality degrades 3.7 points in percentage for the low-IF receiver and 4.6 points for the zero-IF receiver. These results demonstrate that six-port receivers can operate with very low LO powers with good performance. This is an important advantage for SDR, as it entails low power consumption and cost reduction. In addition, problems derived from LO leakage and the self-mixing of LO, which are major drawbacks in direct conversion architectures, can be reduced.

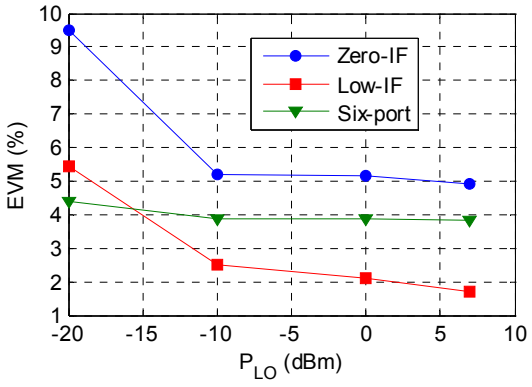

Fig. 4.8: Measured EVM versus P_{LO}: 2595 MHz, 10 Mbps QPSK, Pin=-20 dBm.

4.3.4 Conclusions

Interesting conclusions can be extracted from the previous results. Low values of EVM can be obtained with the low-IF architecture for narrowband signals, as DC-offset and flicker noise problems do not affect the quality of the signal. However, this behaviour is not kept when wideband signals are demodulated. More bandwidth and stricter I-Q balance specifications are required in the low-IF configuration, and the image frequency is a major problem that can not be easily solved.

Direct frequency conversion is a promising alternative, as it does not have the image frequency problem. The zero-IF receiver and the six-port receiver have been demonstrated to have better performance than the low-IF receiver for wideband signals. However, the six-port receiver presents clear benefits over the other two architectures. On one hand, it has been demonstrated that the six-port receiver has larger dynamic range than the other two architectures for the same LO power, due to the high dynamic range diode detector design. All previous reported six-port receivers use zero-biased detector diodes, thereby multi-port receivers are said to have average dynamic range performance. However, the work presented in this chapter demonstrates that the use of a bias current has significant benefits in the dynamic range extension. On the other hand, the six-port receiver works whenever the LO power is very low. This is an important advantage for SDR, as it entails low power consumption, low cost, and reduction of the problems derived from LO leakage and the self-mixing of LO, which are major drawbacks in direct conversion architectures. But the main advantage is that the six-port receiver can operate over extremely large bandwidths, as it has been demonstrated in section 3.5. The multi-band capability of

the six-port receiver has been proved from 300 MHz to 6 GHz with a good quality of the demodulated signal for high-data rates [PIER 2011],[MILCOM 2010].

4.4 OPERATION OF SIX-PORT AS DUAL ZERO-IF/LOW-IF ARCHITECTURE

Six-port receivers are typically direct frequency conversion architectures. Nevertheless, the operation principle of six-port networks as both homodyne and heterodyne receivers was analytically demonstrated in [70]. In spite of it, almost all previous reported six-port receivers have been homodyne ones.

The first reported six-port network used as a heterodyne receiver was presented in [129]. The six-port architecture is used for down-converting the RF signal to an intermediate frequency of 900 MHz. The second frequency conversion is performed by an analog IF module, composed of two differential amplifiers and a conventional IF demodulator. However, the demodulation capability of the heterodyne six-port receiver is only demonstrated by means of simulation results. In any case, the problem of heterodyne receivers is that they require a large number of external components, including bulky RF filters for image frequency rejection and IF circuits. Another problem is the difficulty of changing system parameters, since the RF and IF signals are processed by fixed narrowband analog components. Consequently, heterodyne architecture is not the best option when a SDR hardware implementation is addressed.

It is known that low-IF combines the advantages of homodyne and heterodyne schemes. On one hand, low-IF has typical advantages of homodyne configuration such as low-cost, flexibility, simplicity, compact size, reconfigurability, and high level of integration. On the other hand, as the IF is not located around DC, there are no DC–offset and flicker noise problems, like in homodyne receivers. The main drawback of low-IF receivers is the image frequency. As the image frequency is located very closed to RF signal, no RF filters for image rejection can be used. On the contrary, zero-IF receivers do not have the image frequency problem. Therefore, the most appropriate solution would be to take advantage of both zero-IF and low-IF benefits.

The transformation of the developed SDR six-port receiver into a dual zero-IF/low-IF SDR six-port receiver does not require any change in hardware. In effect, the new block diagram only has changes in software, as it can be seen in Fig. 4.9. In

the low-IF operation mode, the RF signal is down-converted to an IF closed to zero by properly selecting the value of the LO frequency, which could be controlled by software. The final down-conversion to baseband is also performed in the digital domain. In the zero-IF operation mode, the LO and RF frequencies are equal, hence the acquired signals are directly baseband signals and no additional frequency conversions are required. Finally, the six-port calibration algorithm is applied to regenerate the original I-Q components.

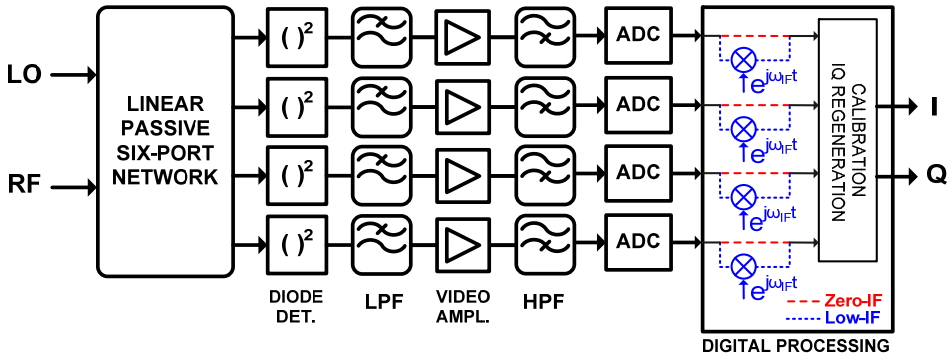

Fig. 4.9: Block diagram of the dual zero-IF/low-IF SDR six-port receiver.

First of all, we will validate the six-port receiver in low-IF operation mode. The RF input signal will be a 2.5 GHz signal with a filtered 64-QAM modulation (roll-off α=0.3) and a power level of -20 dBm. The LO frequency will be fixed to achieve that the lowest IF is equal to 2 MHz, and the LO power level will be 0 dBm. In such conditions, the constellation diagram is that presented in Fig. 4.10.

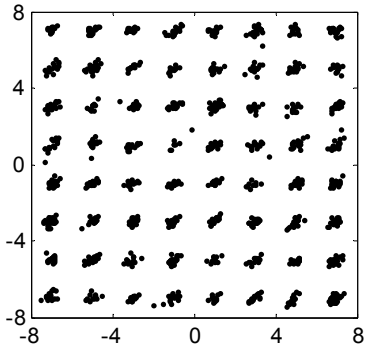

Fig. 4.10: Constellation diagram obtained from the six-port receiver in low-IF operation mode.

The performance comparison of the six-port receiver operating in zero-IF and low-IF modes is presented in Table 4.3. The lowest values of EVM are obtained in the

low-IF mode, as DC-offset and flicker noise problems do not affect the quality of the signal. That is the reason why the low-IF improvement is more evident for narrow band signals, apart from the additional signal degradation in zero-IF due to the DC-offset cancellation high-pass filter. However, remind that this did not happen in the conventional zero-IF/low-IF receiver prototype, where low-IF was superior only for narrow band signals. It was due to the I-Q imbalances, which are now compensated by the calibration method in the six-port receiver. Nonetheless, it is worth to emphasis that the double baseband bandwidth is required in the low-IF mode, which means more complexity in the diode detector design and in the A/D conversion module.

Furthermore, image frequency remains a major problem in low-IF mode. Analogously to proceed in section 4.3.2, a RF tone located at the image frequency is introduced in combination with the desired signal. Table 4.4 shows the effect of the image frequency on the EVM. Note that in this case the degradation of EVM is higher than that observed with the conventional low-IF receiver for the same image attenuation. Take into account that the calibration constants are calculated from a training sequence within the received data frame. Therefore, in the presence of an image frequency the six-port calibration may produce erroneous calibration constants values, leading to an inadequate IQ regeneration.

To sum up, the six-port architecture is susceptible to operate as both zero-IF and low-IF down-conversion schemes without any hardware modification. The system reconfigurability can be completely controlled via software. Such flexibility is a very important advantage, since the system operation mode can be selected depending on, for example, the application, the environment conditions, etc. For example, the low-IF operation mode can be selected for narrow band signals, since DC-offset and 1/f noise would not degrade the downconverted signal and the A/D conversion requirement would be reachable. However, digital compensation techniques must be applied for image rejection. Moreover, zero-IF mode is more suitable for high-speed signal demodulation, as half video bandwidth is demanded compared with low-IF.

Table 4.3 Performance of the six-port receiver operating in zero-IF and low-IF modes.

Symbol rate (Msymbol/s)	Bit rate (Mbps)	Six-port as zero-IF		Six-port as low-IF	
		IF (MHz)	EVM (%)	IF (MHz)	EVM (%)
1.9531	11.71	0-1.2695	6.37	2-4.539	3.05
12.5	75	0-8.125	4.4	2-18.25	3.69

Table 4.4 Influence of image frequency on the six-port receiver in low-IF mode.

Image Attenuation (dB)	EVM (%)
-10	36.73
-5	31.45
0	22.77
10	13.15
20	4.04

4.5 SUMMARY

An experimental performance comparison between the developed six-port receiver and a conventional zero-IF/low-IF receiver has been presented in this chapter.

On one hand, low-IF architecture can achieve very low values of EVM for narrow band signals, as it is not affected by DC-offset and 1/f noise problems. However, direct conversion receivers seem to be the best option when dealing with broadband signals. Low-IF requires the double bandwidth than direct conversion schemes, whereby it is more difficult to maintain proper I-Q balance, which is indispensable to achieve a good image frequency rejection. Image frequency remains a major problem in low-IF receivers, as it can not be easily solved.

On the other hand, the six-port technique shows benefits over conventional zero-IF and low-IF receivers. It can operate with very low values of LO power such as -20 dBm, keeping good quality of the demodulated signal. This is a very important advantage for SDR, as it entails low-cost and low power consumption, as well as a reduction of the LO self-mixing problem, troublesome in direct conversion architectures. In addition, the six-port receiver presents larger dynamic range for a LO power around 0 dBm, due to the selection of a high bias current in the diode detector design. Another key advantage is that six-port receivers can operate over extremely large frequency ranges. The demodulation capability of the developed six-port receiver has been proved from 300 MHz to 6 GHz, which is a four-octave frequency range.

Last but not least, we have demonstrated the capability of the six-port architecture to operate as both zero-IF and low-IF down-conversion schemes. Six-port receivers are traditionally direct conversion architectures. However, we have proposed a dual zero-IF/low-IF SDR six-port receiver, in order to take advantage of both

architectures. Such dual operation mode does not require any change in hardware, since all signal processing is digitally performed.

Considering all the factors mentioned above, it seems logical to go for six-port architecture as a strong candidate to implement a SDR.

The contents of this chapter have been presented in the *IEEE International Carnahan Conference on Security Technologies 2010* [ICCST 2010], and in the national conference *Simposium Nacional de la Unión Científica Internacional de Radio URSI* in 2010 [URSI 2010-2], and 2011 [URSI 2011]. More details can also be found in [130]. As commented in chapter 2, previous to the experimental results presented in this chapter, several comparative studies based on theoretical and simulation analysis were carried out [SDRF 2009],[URSI 2008],[107]. The results extracted from these studies were the starting point for the work presented in this chapter.

Chapter 5

I-Q REGENERATION TECHNIQUES FOR SIX/FIVE-PORT RECEIVERS

5.1 INTRODUCTION

One of the key points of this thesis consists in the research and development of new real-time I-Q regeneration techniques for multi-port receivers. In fact, this is a highly topical subject in six-port receivers. Two new techniques are proposed in this chapter. The first technique is a training-sequence-based auto-calibration method for multi-port receivers. The second one is an analog direct baseband I-Q regeneration method for five-port receivers. The detailed description of the two proposed techniques is presented below.

5.2 CHANNELIZED AUTO-CALIBRATION METHOD

5.2.1 Motivation

As it was seen in section 2.4.2, and according to (2-35) and (2-36), in a six-port receiver the original I-Q components can be recovered from four power measurements and eight calibration constants depending on system response. In the case of a five-port receiver, three power observations are enough, thus six calibration constants are required. However, six/eight constant values may be insufficient to characterize the system, especially for wide-band applications.

Radio frequency architectures for SDR require broadband capabilities to operate in multiple bands with multiple standards. Furthermore, future communication systems will operate with ultra-high-speed signals, which occupy very large bandwidths. The problem is that broadband designs do not present a constant or flat response over their large bandwidth. Reflections provoked by mismatches between the

components can produce a ripple over the response. In the case of six-port receivers, such reflections are typically caused by diodes mismatches, as well as by the variations of the diodes coefficients. Therefore, it seems clear that the regeneration of the I-Q components from eight/six calibration constants could not be accurate enough for high-speed signals, as the calibration constants depend on frequency. To solve this problem we propose an auto-calibration method based on a computational efficient sub-band division. The method is specially suited for broadband communications and strict quality of service (QoS) requirements.

5.2.2 Method description

The proposed method is based on the use of a known training sequence at the beginning of each burst to auto-calibrate the system, as the classical real-time six-port auto-calibration method presented in section 2.4.4.1 [91]-[92]. In order to deal with the problem presented above, we propose a new auto-calibration method based on digital channelization. The method consists of separating the signal in sub-bands in the digital domain, and calculating the calibration constants at each band separately and simultaneously. Although the concept of digital channelization seems simple, however, in a communication system it must be done in real-time, so a computationally efficient filtering is needed.

We have selected a particular family of FIR (*Finite Impulse Response*) type filters for this purpose. The number of filters of the family, *N*, coincides with the order of each filter. The coefficients, b_k, of each filter, *i*, are:

$$b_k^{\,i} = \frac{1}{N} e^{j(i-1)\frac{2\pi}{N}k} \tag{5-1}$$

with *k=0,…,N-1* and *i=1,…,N*. Notice that the coefficients of the first filter, b_k^1, are all one (corrected by a 1/N factor to normalize the filter gain), and the coefficients of the other filters are equal to b_k^1 but with phase shifts that are integer multiples of $2\pi/N$ radians. This means that the first filter is an Nth-order low-pass filter, and the other filters are equal to the first one but shifted an integer multiple of $2\pi/N$ rad/sample. Each filter has a null response at the central pulsation of the other filters. Therefore, the spectrum is divided into N sub–bands using a small number of coefficients, so the required operations can be performed by the hardware in a real time processing. Let us

consider the family of four filters, whose frequency response is shown in Fig. 5.1. The coefficients of the four filters are:

$$b_k^1 = [1 \quad 1 \quad 1 \quad 1] \tag{5-2}$$

$$b_k^2 = [1 \quad +j \quad -1 \quad -j] \tag{5-3}$$

$$b_k^3 = [1 \quad -1 \quad 1 \quad -1] \tag{5-4}$$

$$b_k^4 = [1 \quad -j \quad -1 \quad j] \tag{5-5}$$

In this case, central digital pulsations are 0, ±π/2 and ±π rad/sample; and the coefficients are equal to b_k^1 but shifted ±π/2 and ±π rad. This characteristic is especially interesting, as it means that multiplications are not necessary. The required operations reduce just to sums and subtractions, speeding up the signal processing. Indeed, a ±π rad phase shift means just to subtract the sample, and a ±π/2 rad phase shift means to exchange the real part for the imaginary part and to sum/subtract.

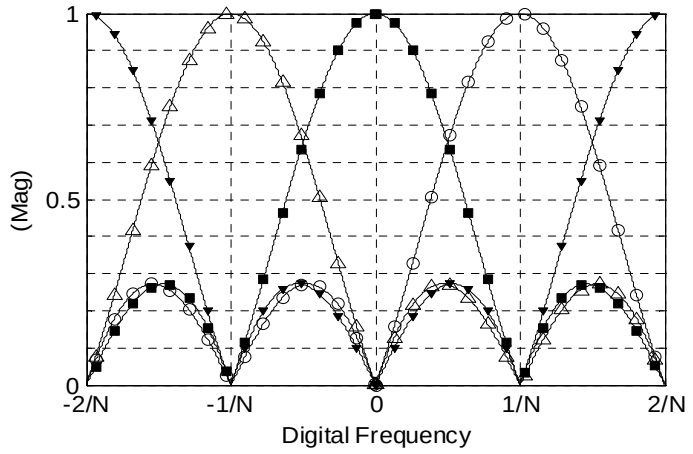

Fig. 5.1: Frequency response of the family of N=4 filters.

It can be demonstrated that the sum of every filter response forms a flat all-pass filter. Then, the I-Q components of every sub–band can be added up to obtain the overall I-Q components of the original signal. Therefore, signals coming from the four six-port receiver outputs are filtered, and the calibration constants of every sub-band are simultaneously calculated from (2-62)-(2-63). I-Q components at each sub-band are obtained applying the corresponding calibration constants into (2-35)-(2-36).

Finally, adding the I-Q components of every sub–band, the I-Q components of the original signal are obtained. Fig. 5.2 represents the scheme of the channelized auto-calibration method for N=4. The proposed method can be also combined with adjacent channel rejection techniques, as that described in [92].

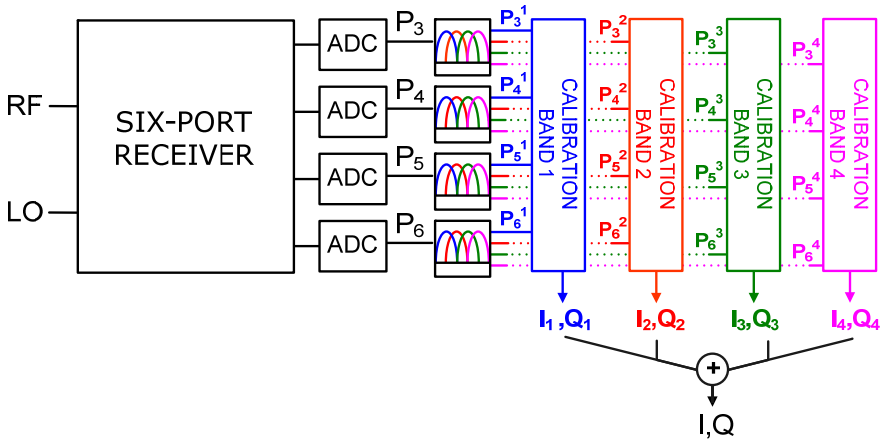

Fig. 5.2: Scheme of the channelized auto-calibration method.

5.2.3 Method validation

The test bench corresponds to that presented in Fig. 3.55. The Agilent E4438C ESG Vector Signal Generator (VSG) generates the RF modulated signal. The LO is the Agilent synthesized sweeper 83752A. Both generators are phase locked. The output signals of the six-port receiver are acquired by a four-channel oscilloscope (*Agilent Infiniium*), with an over-sampling ratio OSR=8. The auto-calibration and I-Q regeneration software, implemented in *Matlab,* is applied in a personal computer, and the EVM is calculated. We use a 2.45 GHz RF signal with a filtered 64-QAM modulation (α=0.3 roll-off square-root-raised cosine filter). The six-port receiver demonstrator can operate with up to 100 MHz-wide signals, so it is expected to perform symbol rates of about 100 Msymbols/s. However, the Agilent E4438C VSG limits the symbol rate to 12.5 Msymbols/s (75 Mbps) for OSR=8. The LO power is P_{LO}=0 dBm, and the RF power (P_{in}) varies from –45 to –5 dBm. After the acquisition of 9200 symbols (73600 samples, OSR=8), we process the data as bursts of length 200 symbols. We use the first 50 symbols to auto-calibrate the system at each burst, and then we demodulate the data sequence of length 150 symbols.

It is advisable to use families with few filters, as it entails few coefficients and thus filtering operations can be real-time performed by the hardware. A lower number of filters can be used by means of previous downsampling. We have used a downsampling ratio of 2, so downsampling and filtering with N filters is similar to use 2N filters without downsampling, except for a slight worsening for low input powers due to the noise aliasing provoked by the downsampling. Nevertheless, this could be solved by applying a simple anti-aliasing pre-filtering technique, consisting of forming a decimated version of the signal summing the samples of the original sequence in twos (presumming technique). This is equivalent to use a low-pass second-order FIR filter whose coefficients are equal to one followed by a downsampling with a ratio of 2.

We have compared the EVM obtained from the conventional auto-calibration method (Conventional AM), with no sub-band division [91],[92], to that obtained from our proposed channelized auto-calibration method (Channelized AM), with and without downsampling. Fig. 5.3 (a) shows the measured EVM as a function of P_{in}. Take into account that neither a LNA nor an AGC have been included in the receiver. EVM curves show quality degradation for high levels of P_{in} due to the rectified wave, a baseband term superposed to the desired signal that increases quadratically with the signal power and, therefore, produces more degradation for high power levels [70]. The results show significant EVM improvements, up to 0.3 percentage points with respect to conventional AM for N=8 filters or N=4 with downsampling. For a Gaussian noise model and a number of received symbols greater than the alphabet length, EVM and signal to noise ratio (SNR) are related by the expression [126]:

$$\mathrm{SNR} \approx \frac{1}{\mathrm{EVM}^2} \tag{5-6}$$

From (5-6), we can obtain the BER (Bit Error Ratio) curves represented in Fig. 5.3 (b). A maximum BER improvement of about one order of magnitude is achieved with N=8 filters or N=4 with downsampling. The channelized auto-calibration method is specially suited for broadband communications and strict QoS requirements, but it is not useful for reducing the sensitivity. The BER reduction is significant with few filters, but if best results are desired, there will be a trade-off between BER reduction and computational efficiency. The use of the proposed channelized auto-calibration

method with only four filters introduces an improvement of 8dB in the dynamic range of a receiver subject to a BER=10^{-6} specification. This is an important advantage of the method, as multi–port schemes do not present good dynamic range behaviour [128].

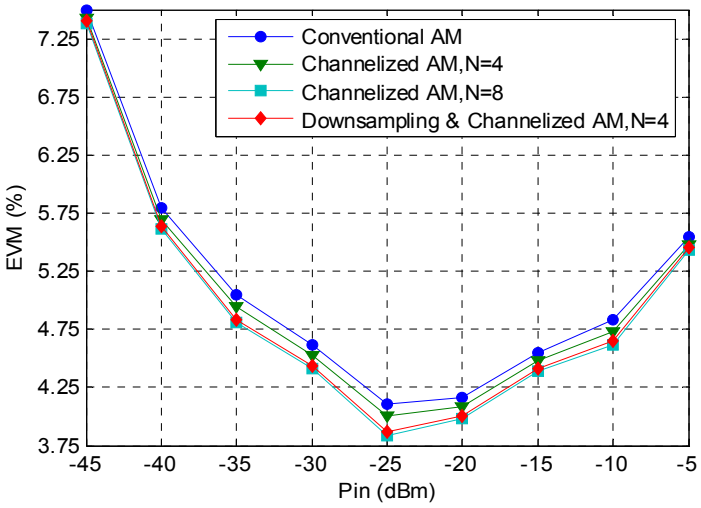

(a)

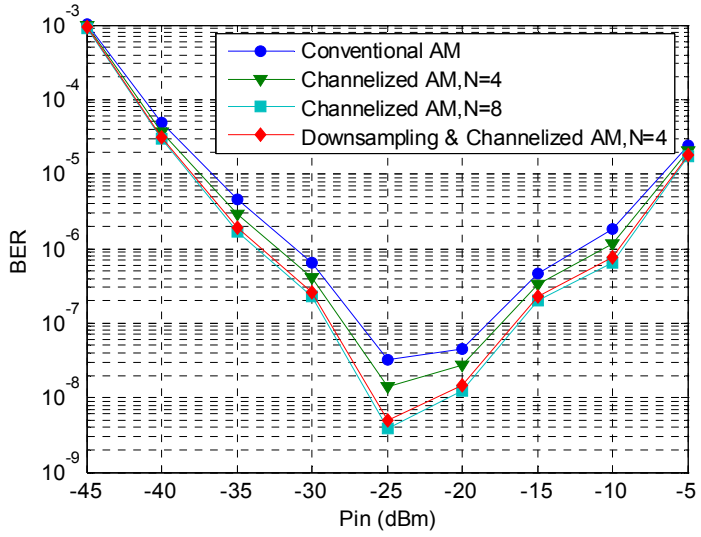

(b)

Fig. 5.3: Validation of the channelized auto-calibration method: 75 Mbps 64-QAM, 2.45 GHz (a) Measured EVM versus P_{in} (b) BER calculated from EVM.

Obviously, the benefits of the auto-calibration method will be more significant for wideband signals and strong system imbalances, although we can not experimentally prove it because of the test instruments limitations (max. 12.5 Msymbol/s). To demonstrate it, we have simulated the performance of a six-port receiver composed of a six-port network, four power detectors and four low-pass

filters. The input signal is the complex envelope of a 64-QAM modulated signal (α=0.3) with a bit rate of 420 Mbit/s, combined with an additive white Gaussian noise (AWGN). The OSR is 8. The LO power is 0 dBm, and the RF power varies from –70 to –10 dBm. Power detectors present square law behaviour and the low–pass filters have ideal responses. The six-port network topology is that shown in Fig. 3.2. We have introduced different ripples over the nominally magnitude and phase parameters of each output port: between 2.5 and 3 dB in magnitude, and 1º and 6º in phase. These ripples have been modelled as sine type functions with a fast frequency variation, in order to validate the auto–method under critical conditions. The simulated BER curves versus SNR are presented in Fig. 5.4. It is worth noting that simulated BER curves respond to the real curves tendency observed in Fig. 5.3. On one hand, no significant BER improvements are achieved for low values of SNR. The effect of the noise aliasing when the downsampling is applied can clearly be appreciated in Fig. 5.4. On the other hand, it can be seen the increase in BER for high input power levels due to the rectified wave. And finally, the BER improvement is maximized when the dominant source of distortion responds to system imbalances (SNR=40 dB). As it happened in the experimental validation, BER improvements of about one order of magnitude are achieved with N=8 filters or N=4 with downsampling. Using N=16 filters or N=8 with downsampling, a BER below 10^{-6} is reached, since the original BER value of 10^{-3} obtained with the conventional AM.

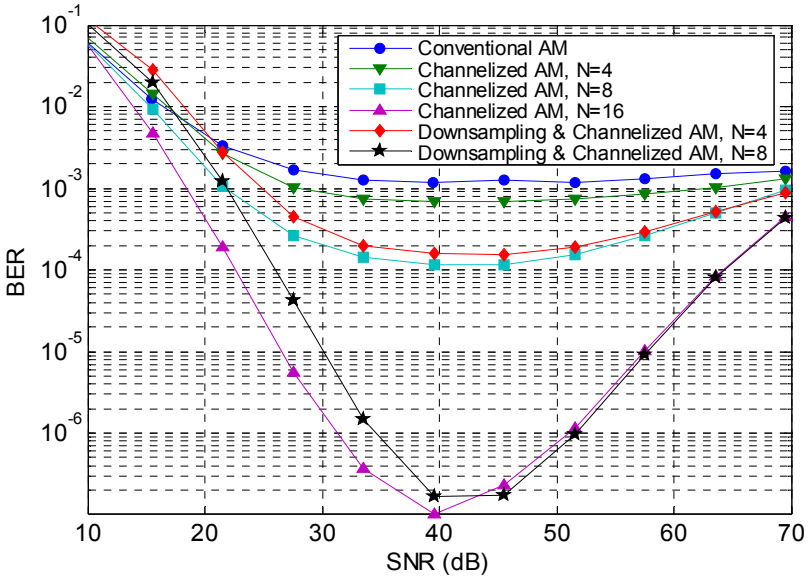

Fig. 5.4: Simulated BER versus SNR for a 420 Mbps 64-QAM signal and strong six-port frequency response variations.

5.3 DIRECT BASEBAND I/Q REGENERATION METHOD FOR FIVE-PORT RECEIVERS

5.3.1 Motivation

The main characteristic of the six(five)-port architecture is its extremely large bandwidth, which involves multi-band and multi-mode capabilities. Six(five)-port networks can operate at very high frequencies, being a serious alternative for millimeter-wave frequencies and high data rate applications. Nevertheless, as it happens with the conventional zero-IF architecture, DC-offset, 1/f noise and second-order intermodulation distortion (IMD2) are primordial drawbacks. In addition, a calibration process is required in order to recover the original I-Q signals, and more baseband outputs are needed (hence more low-pass filters, video amplifiers, ADCs, etc.).

The typical six-port topology admits analog I/Q regeneration by means of a simple circuit, eliminating two baseband branches and the calibration process (see section 2.4.4). This is possible due to the particular characteristics of this six-port topology: the LO and RF signals are combined with equal amplitudes, and relative phase shifts of 0, $\pi/2$, $-\pi/2$, and π rad. However, the habitual procedure in five-port receivers is to digitalize the three output signals and apply a calibration algorithm [15],[92],[131]. Some first approaches of analog I-Q regeneration in five-port receivers used the above mentioned six-port topology with one port reduction. From these particular five-port parameters, a formulation is derived and an analog circuit is proposed to recover the original I/Q components. However, the particular conditions from which the analog circuit is derived in [133], cannot be extended to a general five-port network. For example, the design criterion of an optimal five-port network imposes relative phase shifts of 0º, 120º, and -120º. Here we propose a new, general, and simple method to recover the original I/Q signals in five-port architectures, without using any calibration process. It is based on the use of an analog I/Q regeneration circuit [132], whose structure is derived from a mathematical formulation, which is valid for any kind of five-port topology fulfilling simple necessary conditions. In fact, it will be demonstrated that the work presented in [133] responds to a particular case of the proposed method. The analog I/Q regeneration circuit can be easily integrated without adding complexity to the original circuit. The proposed method solves the

above-mentioned six(five)-port architecture drawbacks, as it eliminates one baseband output and the calibration algorithm without any reduction in the operating frequency band. Moreover, the method allows not only to recover the original I-Q signals, but also to reduce the DC-offset and IMD2. Consequently, the dynamic range can be extended due to the lower output voltages, as a consequence of the DC-offset and IMD2 reduction.

5.3.2 Method description

The present I/Q regeneration method is based on the assumption that there is a symmetry axis in port 4 [132]. That means that the amplitudes of the output signals in ports 3 and 5 have to be equal, and their phase shifts with respect to the signal in port 4 have to be complementary. Therefore, the next two symmetry conditions have to be fulfilled:

(I) Amplitude symmetry condition:

$$A_3 = A_5 \, , B_3 = B_5 \, , K_{23} = K_{25} \tag{5-7}$$

(II) Phase symmetry condition:

$$\theta_3 = C_0 + \gamma \, , \theta_4 = C_0 \, , \theta_5 = C_0 - \gamma \tag{5-8}$$

To simplify the expressions, we will choose C_0= 0, which will only cause a rotation of the constellation. This rotation can be easily compensated by an equalization process. Under amplitude and phase symmetry conditions, the system of equations (2-49) reduces to:

$$\begin{bmatrix} v_3(t) \\ v_4(t) \\ v_5(t) \end{bmatrix} = \begin{bmatrix} R_3 & S_3\cos\gamma & S_3\sin\gamma \\ R_4 & S_4 & 0 \\ R_3 & S_3\cos\gamma & -S_3\sin\gamma \end{bmatrix} \cdot \begin{bmatrix} n(t) \\ I(t) \\ Q(t) \end{bmatrix} + \begin{bmatrix} V_{dc,3} \\ V_{dc,4} \\ V_{dc,3} \end{bmatrix} \tag{5-9}$$

Consequently, the calibration constants result in:

$$r_1 = -\frac{1}{2S_3} \frac{\beta}{\alpha - \beta\cos(\gamma)} \tag{5-10}$$

$$s_I = -\frac{1}{S_3}\frac{1}{\alpha - \beta\cos(\gamma)} \tag{5-11}$$

$$t_I = r_I \tag{5-12}$$

$$r_Q = -\frac{1}{2S_3}\frac{1}{\sin(\gamma)} \tag{5-13}$$

$$s_Q = 0 \tag{5-14}$$

$$t_Q = -r_Q \tag{5-15}$$

with $\beta = \frac{R_4}{R_3}$, and $\alpha = \frac{S_4}{S_3}$.

Substituting (5-10)-(5-15) into (2-50)-(2-51), we obtain:

$$I(t) = \mu_I[-v_3(t) + \frac{2}{\beta}v_4(t) - v_5(t)] + \mu_I V_{dcI} \tag{5-16}$$

$$Q(t) = \mu_Q[v_3(t) - v_5(t)] - \mu_Q V_{dcQ} \tag{5-17}$$

being

$$\mu_I = \frac{1}{2S_3}\frac{\beta}{\alpha - \beta\cos(\gamma)} \tag{5-18}$$

$$\mu_Q = \frac{1}{2S_3}\frac{1}{\sin(\gamma)} = \frac{\beta\sin(\gamma)}{\alpha - \beta\cos(\gamma)} \cdot \mu_I \tag{5-19}$$

$$V_{dcI} = -V_{dc,3} + \frac{2}{\beta}V_{dc,4} - V_{dc,5} \tag{5-20}$$

$$V_{dcQ} = V_{dc,3} - V_{dc,5} = 0 \tag{5-21}$$

Note that the amplitude symmetry condition (5-7) involves that the DC component in the Q-path, V_{dcQ}, is null, since $V_{dc,3}$ is equal to $V_{dc,5}$. The two expressions given by (5-16) and (5-17) can be easily performed by a low-cost operational-amplifier-based circuit, as that shown in Fig. 5.5. The output voltages $v_3(t)$, $v_5(t)$, and

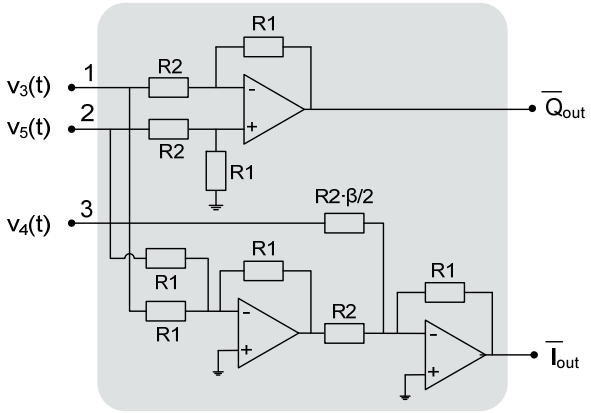

Fig. 5.5: Structure of the analog I/Q regeneration circuit.

$v_4(t)$, are injected into the input ports 1, 2 and 3, respectively. The first operational amplifier performs the subtraction of $v_3(t)$ and $v_5(t)$. The other two amplifiers perform the sum of $v_5(t)$ and $v_3(t)$, and the subtraction of twice the voltage $v_4(t)$ divided by β. This provides the $I_{out}(t)$ and $Q_{out}(t)$ signals, which are equal to the original I/Q signals, excepting for the factors $1/\mu_I$ and $1/\mu_Q$:

$$I_{out}(t) = -v_3(t) + \frac{2}{\beta} v_4(t) - v_5(t) = \frac{I(t)}{\mu_I} - V_{dcI} \tag{5-22}$$

$$Q_{out}(t) = v_3(t) - v_5(t) = \frac{Q(t)}{\mu_Q} \tag{5-23}$$

The expression of the I_{out}/Q_{out} signals regenerated from the proposed technique can be obtained by substituting the values of the three output signals given by (2-48) into (5-22)-(5-23):

$$\begin{bmatrix} I_{out}(t) \\ Q_{out}(t) \end{bmatrix} = \begin{bmatrix} \vec{a}_I \\ \vec{a}_Q \end{bmatrix} \cdot \begin{bmatrix} I(t) \\ Q(t) \end{bmatrix} + \begin{bmatrix} R_I \\ R_Q \end{bmatrix} \cdot n(t) + \begin{bmatrix} V_{dcI} \\ V_{dcQ} \end{bmatrix} \tag{5-24}$$

where

$$\vec{a}_I = \left(-S_3\cos\phi_3 + \frac{2}{\beta}S_4\cos\phi_4 - S_5\cos\phi_5 \;,\; S_3\cos\phi_3 - S_5\cos\phi_5\right) \tag{5-25}$$

$$\vec{a}_Q = \left(-S_3\sin\phi_3 + \frac{2}{\beta}S_4\sin\phi_4 - S_5\sin\phi_5 \;,\; S_3\sin\phi_3 - S_5\sin\phi_5\right) \tag{5-26}$$

$$R_I = -R_3 + \frac{2}{\beta}\mathrm{R}_4 - R_5 \tag{5-27}$$

$$R_Q = R_3 - R_5 = 0 \tag{5-28}$$

The amplitude symmetry condition (5-7) involves that the terms V_{dcQ}, and R_Q are null. Therefore, the DC component and the rectified wave, $R_Q \cdot n(t)$, will not appear in the regenerated $Q_{out}(t)$ signal. If we consider, in addition to symmetry of ports 3 and 5, that the three outputs are amplitude balanced, that is, $\alpha=1$ and $\beta=1$, the expressions (5-16) and (5-17) are reduced to

$$I(t) = \mu_I[-v_3(t) + 2\mathrm{v}_4(t) - v_5(t)] \tag{5-29}$$

$$Q(t) = \mu_Q[v_3(t) - v_5(t)] \tag{5-30}$$

where

$$\mu_I = \frac{1}{2\mathrm{S}_3}\frac{1}{1-\cos(\gamma)} \tag{5-31}$$

$$\mu_Q = \tan\left(\frac{\gamma}{2}\right)\cdot\mu_I \tag{5-32}$$

In this case, V_{dcI}, and R_I are null, hence V_{dcI} and $R_I \cdot n(t)$ will be also eliminated in the regenerated $I_{out}(t)$ signal. In any case, the DC components could be eliminated from the recovered $\mathrm{I_{out}}/\mathrm{Q_{out}}$ signals with analog high-pass filters, or in the digital domain by simply removing the average. On the contrary, the rectified wave, $n(t)$, cannot be eliminated from $\mathrm{I_{out}}/\mathrm{Q_{out}}$, as it is a baseband term superposed to the desired signal. The rectified wave increases quadratically with the signal power and, therefore, produces degradation for high power levels.

5.3.2.1 Orthogonality of the Regenerated I/Q Signals

$\vec{a}_I$ and $\vec{a}_Q$ form a vector base relating the I/Q signals and the $\mathrm{I_{out}}/\mathrm{Q_{out}}$ signals. Therefore, the orthogonality of the $\mathrm{I_{out}}/\mathrm{Q_{out}}$ signals is determined by the vector base orthogonality. This means that the scalar product of $\vec{a}_I$ and $\vec{a}_Q$ must be zero:

$$\vec{a}_I \cdot \vec{a}_Q = \left(-S_3\cos\phi_3 + \frac{2}{\beta}\mathrm{S}_4\cos\phi_4 - S_5\cos\phi_5 \right) \cdot \left(S_3\cos\phi_3 - S_5\cos\phi_5 \right) + \left(-S_3\sin\phi_3 + \frac{2}{\beta}\mathrm{S}_4\sin\phi_4 - S_5\sin\phi_5 \right) \cdot \left(S_3\sin\phi_3 - S_5\sin\phi_5 \right) = 0 \quad (5\text{-}33)$$

Assuming amplitude symmetry in ports 3 and 5 (5-7), the scalar product results in:

$$\vec{a}_I \cdot \vec{a}_Q = \frac{2}{\beta}\mathrm{S}_3 S_4\cos(\phi_3 - \phi_4) - \frac{2}{\beta}\mathrm{S}_3 S_4\cos(\phi_4 - \phi_5) \quad (5\text{-}34)$$

which is equal to zero if:

$$\left|\Phi_3 - \Phi_4\right| = \left|\Phi_4 - \Phi_5\right| \quad (5\text{-}35)$$

This above expression corresponds precisely to the phase symmetry condition (5-8). Consequently, the orthogonality of the received I_{out}/Q_{out} signals is ensured under the amplitude and phase symmetry conditions expressed in (5-7)-(5-8). This means that a symmetrical 3-way RF circuit with respect to port 4 is needed, that is, with symmetry between ports 3 and 5. And most of the five-port circuits in the literature satisfy this condition.

The orthogonality of the regenerated IQ signals does not depend on the value of γ, provided that the amplitude and phase symmetry conditions are fulfilled. Nonetheless, when the five-port circuit response deviates from the symmetrical behavior, the selection of γ can be important. To illustrate this situation, we have simulated the orthogonality degradation due to lack of symmetry. The degradation coming from lack of phase symmetry has been evaluated by introducing a phase error into port 5, that is: $\Phi_3=\gamma$, $\Phi_4=C_0=0$, $\Phi_5=-\gamma-\Delta\Phi$, where $\Delta\Phi$ represents the phase deviation from symmetry. To evaluate the degradation due to lack of amplitude, $v_5(t)$ has been divided by a factor α, which represents the amplitude error. The results are plotted in Fig. 5.6. The conclusion is that the orthogonality is more vulnerable to phase errors as γ separates from 90º. For example, a ±10º phase error leads to a maximum IQ phase imbalance of 5º for γ=50º and γ=130º; 2.3º for γ=70º and γ=110º; and 0.5º for γ=90º. Moreover, a ±10º IQ phase imbalance can be obtained with amplitude errors of ±3 dB.

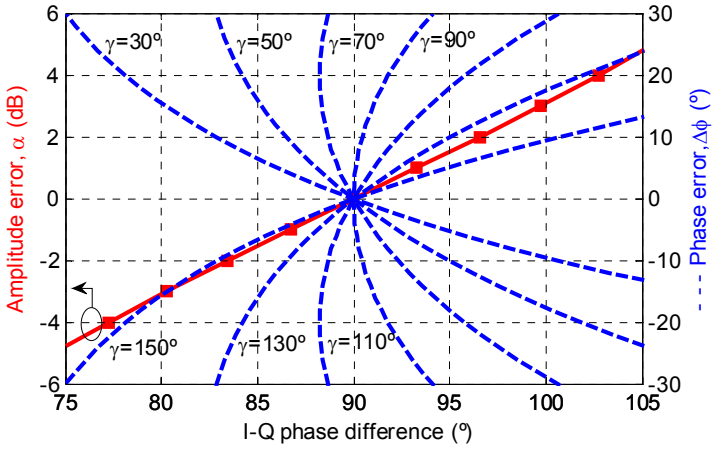

Fig. 5.6: Orthogonality degradation due to lack of symmetry.

5.3.2.2 Amplitude of the Regenerated I/Q Signals

The regenerated $I_{out}(t)$ and $Q_{out}(t)$ signals differ from the original I(t) and Q(t) signals by the factors $1/\mu_I$ and $1/\mu_Q$ (5-22)-(5-23), respectively. Moreover, μ_I and μ_Q depend on γ as for (5-31)-(5-32). This means that, although the selection of γ does not have influence in the fulfilment of condition (5-8) and, therefore, in the I_{out}/Q_{out} orthogonality, the amplitude of the regenerated $I_{out}(t)$ and $Q_{out}(t)$ signals will be different depending on γ.

Let us consider, for simplicity, a fully symmetrical five-port circuit, that is, $\alpha=1$ and $\beta=1$. As it can be derived from (5-32), the relation between the amplitudes of $I_{out}(t)$ and $Q_{out}(t)$ responds to $\mu_Q/\mu_I=\tan(\gamma/2)$. Therefore, the I-Q amplitude imbalance will be determined by $\tan(\gamma/2)$. Fig 5.7 represents the values of $1/\mu_I$, $1/\mu_Q$, and $\tan(\gamma/2)$ as a function of γ, considering the typical value of S_3=0.5. As it can be seen, the original I/Q signals can be directly recovered from $I_{out}(t)$ and $Q_{out}(t)$ if γ=90º, and no amplitude imbalance is observed in this case. The amplitude imbalance increases as γ separates from 90º, so either analog or digital amplitude imbalance correction is required. Around γ=90º, $1/\mu_Q$ keeps a constant value of 1, and $1/\mu_I$ is equal to $\tan(\gamma/2)$, which presents a linear tendency. An analog amplitude compensation could be easily performed by means of a variable gain block in the I-channel, as the correction can be directly obtained from the received $Q_{out}(t)$ signal. Amplitude imbalance can be also digitally compensated.

The work presented in [133] responds to the particular situation of a five-port circuit with γ=90º, and the same amplitude response in the three ports. The authors

extract the equations describing the I/Q regeneration circuit behavior from these specific conditions, but they do not consider a general five-port junction. However, the design criterion of an optimal five-port network imposes γ=120º. We have demonstrated that the proposed I/Q regeneration technique can be extended to any five-port structure, as long as it fulfils the amplitude and phase symmetry conditions just in ports 3 and 5 (5-7)-(5-8).

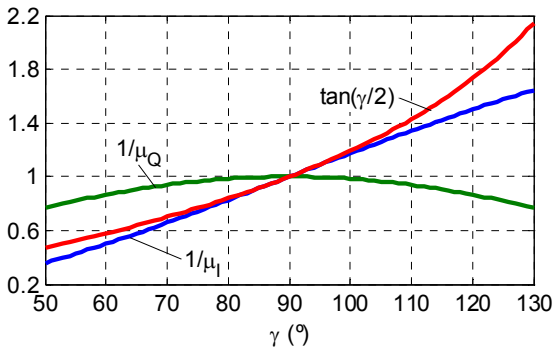

Fig 5.7: Variation of $1/\mu_I$, $1/\mu_Q$, and tan(γ/2) with γ.

5.3.2.3 DC-offset and IMD2 suppression

The term $K_2 \cdot [x(t)]^2$ in (2-25) represents a second-order nonlinearity, which generates undesired baseband beats affecting the performance of direct conversion receivers [27],[42]. These undesired distortion terms are represented as $V_{dc,i}$ and $R_i \cdot n(t)$ in (2-48). Moreover, in the presence of strong interfering signals, other undesirable distortion products can be generated. This situation occurs, for example, when an adjacent channel is located within the bandwidth of the receiver's RF filter. In this case, the RF input signal would be:

$$v_{RF}(t) = \Re e\left\{\left[I(t) + jQ(t)\right] \cdot e^{j2\pi f_{RF} t} + z_{adj}(t) \cdot e^{j2\pi f_{adj} t}\right\} \tag{5-36}$$

where f_{adj} and $z_{adj}(t)=I_{adj}(t)+jQ_{adj}(t)$ represent, respectively, the frequency and the complex envelope of the adjacent channel signals. If $|f_{adj} - f_{LO}|$ is greater than the cut-off frequency of the low pass filter, the output $v_i(t)$ signals will be:

$$\begin{aligned} v_i(t) &= \frac{K_{2i}}{2} A_i^2 V_{LO}^2 + \frac{K_{2i}}{2}\left\{B_i^2\left(I^2(t)+Q^2(t)\right) + B_{f_{adj},i}{}^2\left(I_{adj}{}^2(t)+Q_{adj}{}^2(t)\right)\right\} \\ &+ S_i\left(I(t)\cos\Phi_i + Q(t)\sin\Phi_i\right) \end{aligned} \tag{5-37}$$

with $B_{fadj,\,i}$ the five-port circuit attenuation from the RF port at f_{adj}. Therefore, not only the self-mixing of the LO and useful signals will appear, but also the self-mixing of the adjacent channels, which occupy twice the bandwidth of $I_{adj}(t)$ or $Q_{adj}(t)$. (5-37) can rewritten as follows

$$v_i(t) = V_{dc,i} + dc_i' + R_i n(t) + R'_i\, n_{adj}(t) + S_i\left[\cos\phi_i I(t) + \sin\phi_i Q(t)\right] \tag{5-38}$$

where $R'_i = \frac{K_{2i}}{2} B^2_{f_{adj},i}$. dc_i' and $n_{adj}(t)$ are, respectively, the DC and time variant components of the self-mixing of the adjacent channel. Now the expression of I_{out}/Q_{out} will be:

$$\begin{bmatrix} I_{out}(t) \\ Q_{out}(t) \end{bmatrix} = \begin{bmatrix} \vec{a}_I \\ \vec{a}_Q \end{bmatrix} \cdot \begin{bmatrix} I(t) \\ Q(t) \end{bmatrix} + \begin{bmatrix} R_I \\ R_Q \end{bmatrix} \cdot n(t) + \begin{bmatrix} R'_I \\ R'_Q \end{bmatrix} \cdot n_{adj}(t) + \begin{bmatrix} V_{dcI} \\ V_{dcQ} \end{bmatrix} \tag{5-39}$$

Where $R'_I = -R'_3 + \frac{2}{\beta} R'_4 - R'_5$, and $R'_Q = R'_3 - R'_5 = 0$.

On one hand, the amplitude symmetry condition between ports 3 and 5 involves that the terms V_{dcQ}, R_Q and R'_Q are null. Hence, no DC-offset and IMD2 will appear in the Q-path. On the other hand, if the same amplitude response is presented in port 4, V_{dcI}, R_I and R'_I will be null, and the DC-offset and IMD2 terms will be also eliminated in the I-path.

Another possible situation that results in the generation of undesirable baseband components is the following. Consider two strong signals, $cos(2\pi f_1 t)$ and $cos(2\pi f_2 t)$, separated in frequency an amount f_2-f_1=Δ, less than the bandwidth of interest. When these signals are exposed to a second-order nonlinear behavior, a baseband beat is generated at Δ Hz:

$$\begin{aligned} v_i(t) &= V_{dc,i} + R_i \cdot n(t) + \sum_{n=1}^{2} R'_{i,n} \cdot n_{adj,n}(t) \\ &+ S_i\left(\cos\Phi_i I(t) + \sin\Phi_i Q(t)\right) + S'_i \cos(2\pi\Delta t) \end{aligned} \tag{5-40}$$

where $S'_i = K_{2i} \cdot B_{f1,i} \cdot B_{f2,i}$, and B_{f1} and B_{f2} are the five-port circuit attenuations from the RF port at frequencies f_1 and f_2. The same conclusions can be extracted in this case: the amplitude symmetry condition between ports 3 and 5 ensures distortion rejection in the Q-signal; considering the same attenuation in port 4, the distortion can be also

eliminated in the I-path. Consequently, the IMD2 and the DC-offset can be eliminated in the regenerated I/Q signals if there is the same attenuation in three output ports.

5.3.3 Method validation

A five-port receiver prototype has been developed in order to validate the proposed I/Q regeneration method. The block diagram of the fabricated five-port receiver is shown in Fig. 5.8. It is composed of a five-port demodulator circuit and an analogical I/Q regeneration circuit.

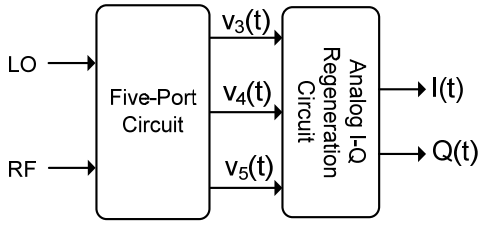

Fig. 5.8: Block diagram of the developed five-port receiver.

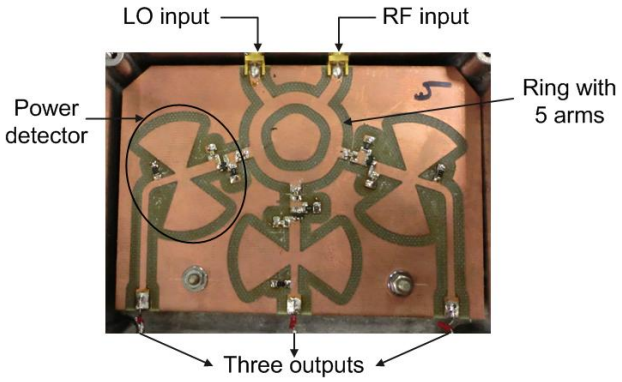

Fig. 5.9: Fabricated five-port circuit.

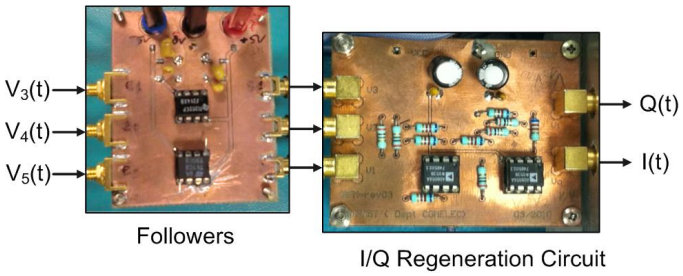

Fig. 5.10: Fabricated I/Q regeneration circuit.

Fig. 5.9 illustrates a photograph of the fabricated five-port circuit, using MIC (Microwave Integrated Circuits) technology. It is composed of a five-port junction and three power detectors. The five-port interferometer is a microstrip ring designed for a 2.1 GHz central frequency, using a FR4 substrate (ε_r=4.7, h=1.59 mm). It is designed under amplitude and phase conditions (5-7)-(5-8), with γ=120º. The power detectors are implemented using the Agilent HSMS2850 Schottky diode.

Fig. 5.10 shows the fabricated I/Q regeneration circuit, which responds to the configuration represented in Fig. 5.5, with $\beta=1$. The values of R1 and R2 have been selected to achieve a voltage gain of 30. Therefore, in order to ensure equal and high load impedance at the three detectors outputs, a simple circuit composed of three followers has been added before the I/Q regeneration circuit.

5.3.3.1 Measured I/Q phase and amplitude imbalance

According to the theory presented above, the orthogonality of the regenerated I/Q signals is ensured when both amplitude and phase symmetry conditions (5-7)-(5-8) are maintained. Consequently, the first step is to verify if the developed five-port circuit fulfils these symmetry conditions.

Two sinusoidal signals with a 10 kHz frequency displacement are introduced into the RF and LO input ports. These signals come from two Agilent E8267D signal generators, which have been phase locked. The LO power level is fixed to P_{LO}=0 dBm, and the RF power to P_{RF}= -35 dBm. The three output signals of the five-port circuit are introduced into the Agilent 54622A oscilloscope. Fig. 5.11 represents the measured amplitudes of the three output signals (V_3, V_4, V_5), and the measured phase shifts of signals $v_3(t)$ and $v_5(t)$ with respect to signal $v_4(t)$ (Φ_3-Φ_4, Φ_4-Φ_5). As it can be seen, the circuit keeps phase symmetry in a very large frequency range, from 0.5 to 2.5 GHz. However, the amplitude balance between ports 3 and 5 is only maintained around the central frequency, 2.1 GHz, as five-port rings typically cover less than 20% bandwidth. A ±3.5 dB amplitude imbalance between ports 3 and 5 is observed from 0.5 to 2.5 GHz. Therefore, from Fig. 5.6, a maximum IQ phase imbalance of 11.5º is foreseen.

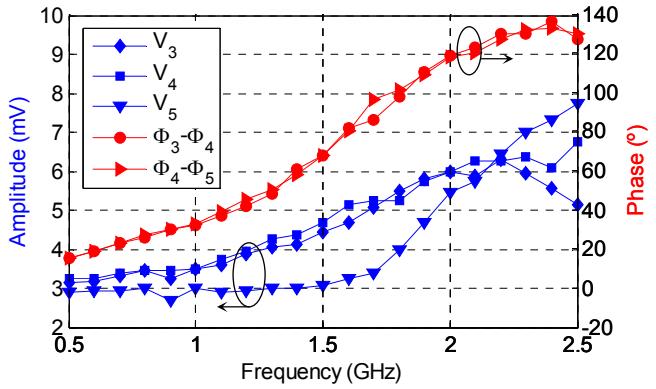

Fig. 5.11: Measured amplitude and phase shift of the five-port circuit output signals (P_{RF}=-35 dBm, P_{LO}=0 dBm, Δf= 10 KHz), and simulated IQ phase difference.

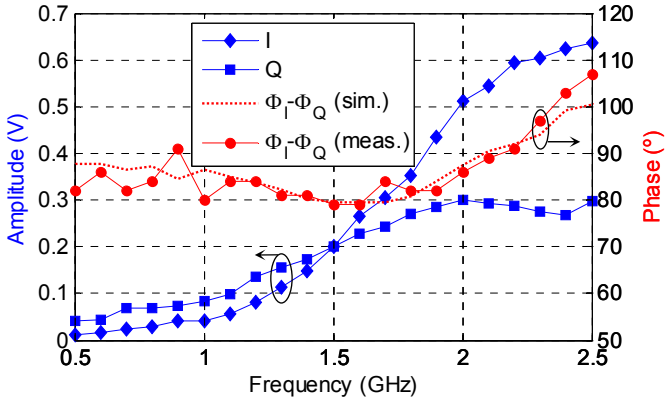

Fig. 5.12: Measured amplitude and phase of the received I/Q signals (P_{RF}=-35 dBm, P_{LO}=0 dBm, Δf= 10 KHz), and simulated I/Q phase difference.

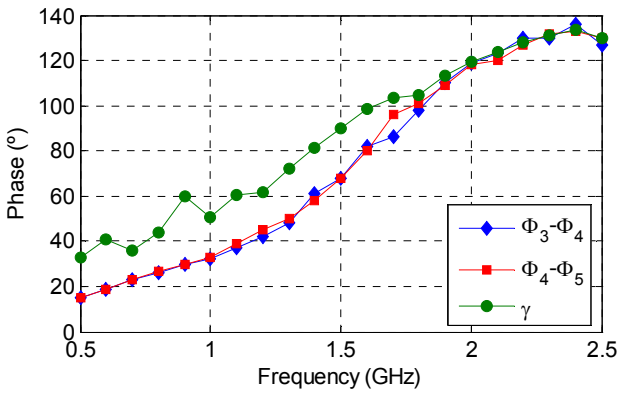

Fig. 5.13: Comparison between the measured phase shift of the five-port circuit output signals and the value of γ calculated from the measured IQ amplitudes.

Next, the I/Q regeneration circuit is connected to the five-port circuit, and the received I/Q signals are introduced into the Agilent 54622A oscilloscope. The measured amplitudes and phase difference of the received I/Q signals are presented in Fig. 5.12. The simulated IQ phase imbalance, calculated from the measured five-port circuit response (Fig. 5.11), is also plotted in Fig. 5.12. On one hand, a constant phase difference around 90º is maintained from 0.5 to 2.3 GHz, although there is not amplitude symmetry in this frequency range. The maximum phase imbalance is 10º. Therefore, it seems that the phase symmetry condition has more influence in the I/Q orthogonality than the amplitude symmetry condition. Consequently, the proposed technique permits to increase the operating frequency of the five-port demodulator. On the other hand, as it was demonstrated in section III.B, the relation between the amplitudes of the regenerated I/Q signals is given by the term $\tan(\gamma/2)$. Therefore, the value of γ can be calculated from the measured I/Q amplitudes. The comparison between the calculated value of γ, and the measured phase shift of the five-port circuit output signals is presented in Fig. 5.13. The system follows the theoretical behavior from 1.8 GHz to 2.5 GHz, although there is not perfect amplitude symmetry between ports 3 and 5 (Fig. 5.11).

5.3.3.2 Measured DC-offset and IMD2 suppression

As it was demonstrated before, the IMD2 and the DC-offset can be eliminated in the received I/Q signals if there is the same attenuation in three output ports. The first experiment to prove this affirmation will be carried out without the presence of adjacent channel signals, in order to evaluate just the DC-offset suppression performance. Two sinusoidal signals, coming from two Agilent E8267D generators and separated 10 kHz in frequency, are introduced into the RF and LO input ports. The RF power is P_{RF}=-35 dBm. Since the I/Q regeneration circuit has a voltage gain of 30, the relation between the DC-voltage and the amplitude of the received signal will be evaluated. This relation will be firstly measured at the three five-port circuit outputs, using the Agilent 54622A oscilloscope. It corresponds to the case of using a typical five-port receiver configuration, where the three outputs are directly digitalized. After, we will connect the analog I/Q regeneration circuit between the five-port circuit and the oscilloscope, and the relation will be measured at the I and Q outputs. Setting the LO power to P_{LO}=0 dBm and varying the frequency, the measured results are that

presented in Fig. 5.14. The ratio DC-voltage/Amplitude is effectively lower in the I/Q signals for all the measured frequency range. This ratio approximates to zero around the central frequency of the five-port circuit, since there is amplitude symmetry and the DC-voltage tends to be null. Fig. 5.15 shows the ratios DC-voltage/Amplitude as a function of the LO power, fixing a frequency of 2.1 GHz. Once again, the ratio is lower in the I/Q signals for all the values of P_{LO}. In addition, the DC-offset is completely cancelled for values of P_{LO} around -4 and -3 dBm.

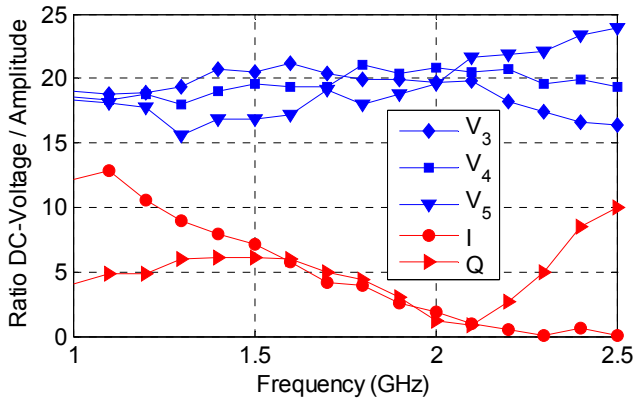

Fig. 5.14: DC-offset suppression performance versus frequency, P_{LO}=0 dBm.

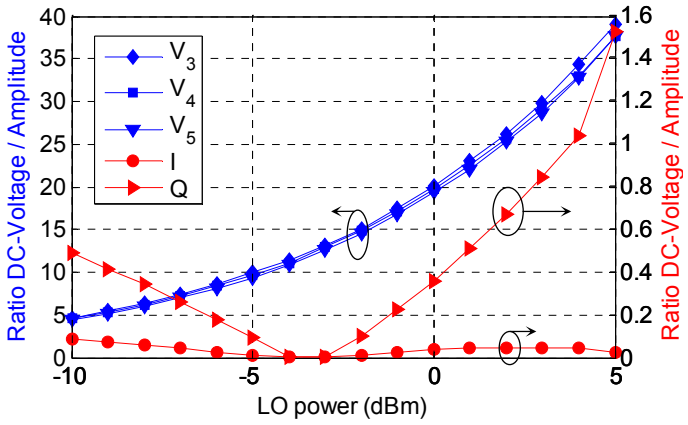

Fig. 5.15: DC-offset suppression performance versus LO power, f=2.1 GHz.

Secondly, the IMD2 suppression performance will be evaluated in the presence of strong interfering signals. We have considered the two situations expounded in section III.C: one interfering adjacent channel signal, and two interfering signals. In the first situation, both wanted and interfering signals are 100 kbps QPSK modulated signals, located at f_{RF}=2.1 GHz and f_{adj}=2 GHz, respectively. The LO power is

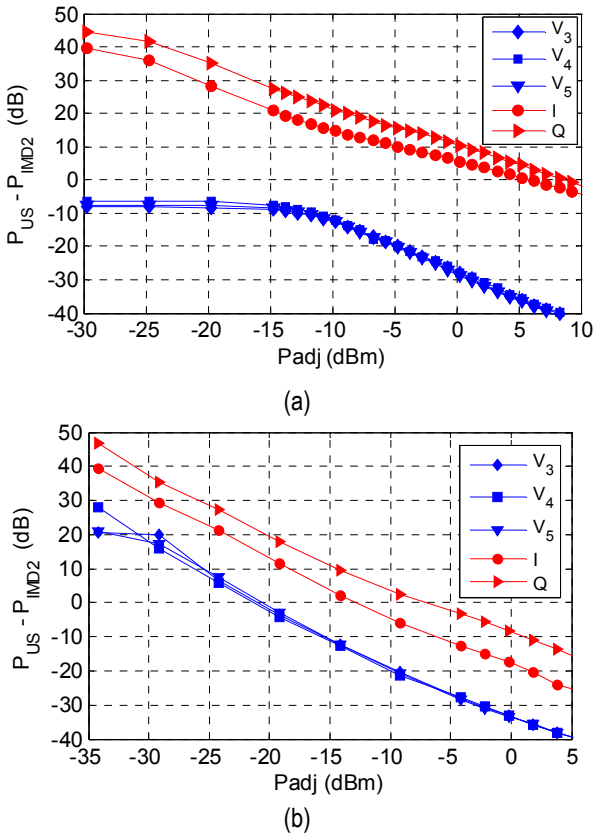

Fig. 5.16: IMD2 suppression performance versus adjacent channel power, P_{adj} (a) One interfering adjacent channel signal (b) Two interfering signals.

P_{LO}=-3 dBm, and the wanted signal power is P_{RF}=-39.8 dBm. The interference power (P_{adj}) will be swept from -30 to 10 dBm. First, we introduce the wanted signal into the input of the five- port circuit. Using a spectrum analyzer, we measure the power concentrated into the baseband signal bandwidth (0-50 kHz), which will be called useful signal power (P_{US}). This power comprises the contribution of the desired signal, and its self-mixing. Next, we introduce the interfering signal and repeat the same measurement. In this case, the measured power corresponds to the self-mixing of the interfering signal (P_{IMD2}). The measured relation between P_{US} and P_{IMD2} for different values of P_{adj} is shown in Fig. 5.16 (a). The quadratic behavior of the self-mixing terms can be clearly appreciated in the curves corresponding to V_i. The IMD2 reject improvement with respect to a conventional five-port receiver is evident. P_{US} is lower than P_{IMD2} at the five-port circuit outputs, while the opposite situation happens when the I/Q regeneration circuit is used. The proposed five-port demodulator achieves an increment in the relation P_{US}-P_{IMD2} between 26 and 45 dB.

In the second situation, two tones separated 200 kHz at 2 GHz are combined with the wanted signal, which is a tone separated 10 kHz from the f_{LO}=2.1 GHz. The LO power is P_{LO}=-3 dBm, and the wanted signal power is P_{RF}=-39.8 dBm. Now P_{US} will be the power of the received tone at 10 kHz, and P_{IMD2} will be the power of the interferences beat at 200 kHz. Fig. 5.16 (b) collects the measured results, where P_{adj} is the power of each interfering tone. In this case, the IMD2 term is linear with the power, as expected from (5-40). Once again, the improvement in the IMD2 reject is significant, around 15 dB better in the output I, and 23 dB in the output Q.

5.3.3.3 Demodulation results

In this section, we will verify the demodulation capacity of the developed five-port receiver. The test bench is shown in Fig. 5.17. Two Agilent E8267D signal generators are used as LO and RF QPSK-modulated signals. Both generators are phase locked. The I/Q output signals of the five-port demodulator are sampled by an acquisition card (PCI-6110E National Instruments), using an 800 kHz sampling frequency. The symbol rate is 100 kbps, thus the over-sampling ratio is OSR=8. The format of the data burst is in conformity with Fig. 5.18. It consists of a training sequence (TS) and a data sequence. The TS is used to perform the symbol synchronization and the equalization process based on the Minimum Mean Square Error Zero Forcing (MMSE) algorithm, which compensates the amplitude imbalance of the regenerated I/Q signals. The TS is composed of 13 symbols, which correspond to the 26 bits of the GSM TSC1 training sequence. The data sequence is made up of 64 symbols (128 bits).

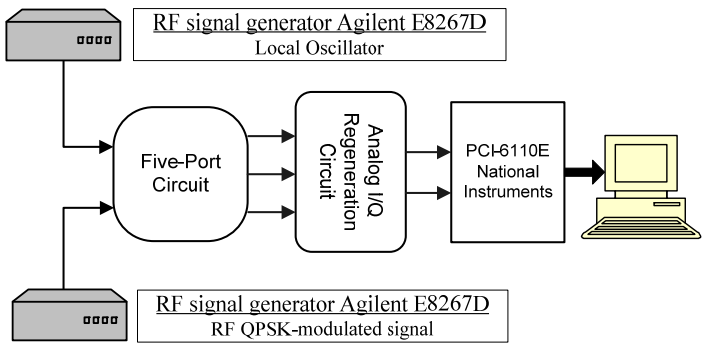

Fig. 5.17: Set-up of the five-port receiver test bench.

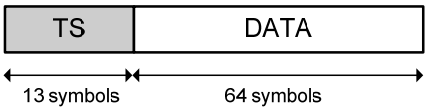

Fig. 5.18: Structure of the transmitted data burst.

Fig. 5.19 shows an example of the QPSK constellation diagrams recovered by our circuit at 1 GHz, 1.5 GHz, and 2 GHz. The represented constellations include all the acquired data (grey traces), and the recovered symbols after synchronization (black points). We observe correct equalization performance, since constellation diagrams are normalized and centred. In addition, the symbol synchronization is good, as the recovered symbols are located close to their ideal position. The variation of the Error Vector Magnitude (EVM) with frequency is also presented in Fig. 5.20. The value of EVM is quite high, due to the slight rotation that can be observed in the constellations. This rotation comes from the difference between the real behavior of the circuits, and the theoretical I/Q regeneration equations. However, it can be easily compensated in the digital domain. Furthermore, an EVM of 14 % is enough to demodulate a QPSK signal without errors. In any case, the importance of these results is that they demonstrate the demodulation capacity of the system in a large frequency range, even if not perfect five-port symmetry is achieved.

Finally, we have measured the sensitivity of our receiver, defined as the RF input power to ensure a BER of 10^{-3}. The following figure represents the BER versus the power of QPSK modulated signal. We obtain a sensitivity of –65.4 dBm for the developed five port receiver, without using a low noise amplifier. The sensitivity improves around 3 dB with respect to digital I/Q regeneration [92], as a consequence of the DC-offset cancelation. Furthermore, a BER improvement will be also observed when handing high power levels, or in the presence of interfering signals, due to the IMD2 suppression.

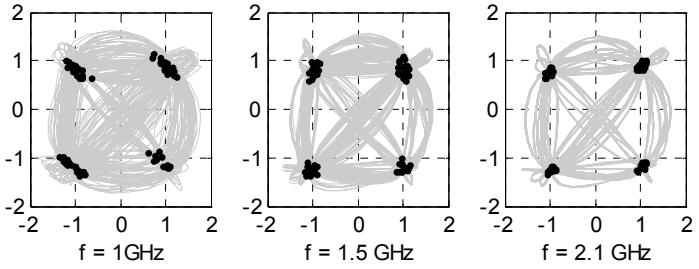

Fig. 5.19: Received constellations, P_{RF}= -35 dBm, P_{LO}=-3 dBm.

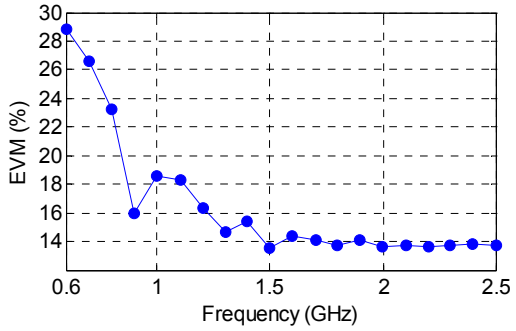

Fig. 5.20: Measured EVM versus frequency, P_{LO}= -3 dBm, P_{RF}=-35 dBm.

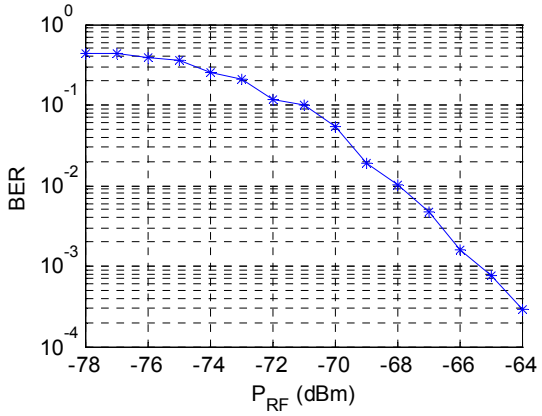

Fig. 5.21: Measured BER versus RF power of the QPSK modulated signal, f= 2.1 GHz, P_{LO}=-3 dBm.

5.4 SUMMARY

Two new real time I-Q regeneration techniques for six(five)-port receivers have been proposed in this chapter.

The first technique is a new auto-calibration method based on a computational efficient sub-band division. The method is specially suited for broadband communications and strict QoS requirements. The proposed FIR filters are easy to implement and have few coefficients, so operations can be real-time performed by the hardware. In addition, operations can be reduced to sums and subtractions using four filters, speeding up the signal processing. Measurement results show a significant BER improvement, above one order of magnitude with respect to conventional auto-calibration method.

The second technique is a direct baseband I/Q regeneration method applicable to five-port architectures. It is based on the property that the five-port circuit has an axis of symmetry, which can be easily satisfied by five-port and three-phase circuits. The validity of the method has been satisfactorily proved in an experimental five-port receiver. The proposed method meets some typical drawbacks of five-port receivers. On one hand, it eliminates one baseband output and the calibration algorithm without any reduction in the operating frequency band. On the other hand, it improves the DC-offset and IMD2 rejection, which are main problems in direct conversion architectures.

The proposed channelized auto-calibration method has been published in the Journal *Progress in Electromagnetics Research* [PIER 2011], and presented in the national conference *XXIV Simposium Nacional de la Unión Científica Internacional de Radio URSI 2009* [URSI 2009].

Regarding to the regeneration method for five-port receivers, it was developed in collaboration with Prof. Bernard Huyart, during a research internship in the Telecom ParisTech (Paris, France) in 2011. Currently, we have an accepted paper for publication in the *IEEE Trans. Microwave Theory and Techniques* [MTT 2012-1].

Chapter 6

SIX-PORT RECEIVER IN LTCC TECHNOLOGY

6.1 INTRODUCTION

The main advantage of the six-port architecture is its extremely large bandwidth, which involves multi-band and multi-mode capabilities. However, an important problem is the large dimensions of the passive six-port structure. The higher the frequency, the smaller the passive circuit and the easier the integration in a MMIC design. But for operating frequencies in the lower gigahertz region, a broadband design leads to large dimensions, which could be prohibitive, for example, for mobile communication applications. Therefore, new technologies must be explored in order to achieve compact size and low-cost productions for configurable radio terminals

Low-Temperature Cofired Ceramic (LTCC) is a cost-effective substrate technology which enables to develop compact microwave and millimeter wave modules [134]. It makes possible to integrate passive and active microwave circuits, antenna structures, low-frequency electronics, and digital components on one multilayer substrate. Owing to low conductor loss, low dielectric loss, and up to fifty laminated layers, LTCC provides a suitable approach for embedded microwave and millimetre-wave passive components and accessories including antennas. In addition, LTCC substrate materials possess a wide range of thermal expansion coefficients, being very attractive for integrated packaging solutions.

Our objective is to study the contribution of LTCC to the miniaturization of the six-port architecture. Consequently, and continuing our previous work, we have developed a new version of the six-port receiver based on LTCC technology. In the

first place, the LTCC 90-degree hybrid coupler was designed and fabricated, since it is the most critical component of the six-port network. Once proved the viability of the technology, the complete LTCC six-port receiver was developed and characterized.

6.2 VALIDATION OF THE TECHNOLOGY: LTCC 90º HYBRID COUPLER DEVELOPMENT

The critical element of the six-port network is the 90-degree hybrid coupler, as it determines the system bandwidth. Consequently, in order to prove the feasibility and performance of the LTCC technology, we have firstly developed the 90-degree hybrid coupler. It will be implemented by the tandem connection of two symmetrical multisection 8.34-dB couplers.

The LTCC layer structure, represented in Fig. 6.1, is composed of eight DuPont-951 substrate layers (ε_r=7.8, tgδ=0.006 @3GHz). It is worth to point out that our research group (Microwave and Radar Group, GMR) was participating in a research project funded by the Spanish National Board of Scientific and Technological Research (CICYT) for 3D integration of microwave and millimetre wave circuits using LTCC technology (TEC2008-02148). Therefore, the substrate and layer distribution were imposed by the project, since other circuits were included in the same LTCC wafer, hence no modifications were admitted.

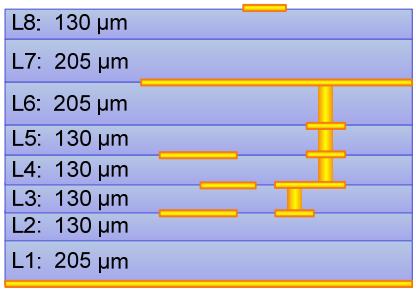

Fig. 6.1: LTCC layer structure using DuPont-951 substrate.

The highest coupling level required in a multisection coupler design, which corresponds to the central section coupling level, will limit the bandwidth. From the design tables [119], for a ±0.05-dB ripple 8.34-dB coupler, the central section coupling level is 6.28 dB for three λ/4-sections, 5.18 dB for five sections, and 4.47 dB for seven sections. Higher ripple levels provide wider bandwidths, but it leads to higher

coupling levels. Considering a 930 μm substrate height, the theoretical coupling level achieved with two 50 Ω λ/4 broadside-coupled striplines with a 130 μm separation is 5.89 dB. This reduces the possibilities to use a three-section design, with a stripline structure composed of layers L1-L6 (930 μm). The ripple could be increased until ±0.2 dB, achieving a theoretical bandwidth of $B=f_2/f_1=3.18211$, which means that the 1838.4-5850 MHz frequency range could theoretically be covered. If a larger bandwidth is required, coupling can be maximized by reducing the separation of the inner conductors, and increasing the distance to the ground planes. A low dielectric constant substrate also maximizes the highest coupling, as the ground plane separation will be large relative to the overlay separation, although this increases the circuit dimension. However, our design has to adapt to the fixed layer structure, and no modifications can be realized to increase the bandwidth.

The even and odd impedances for a symmetrical 3-section, ±0.2-dB ripple level, 8.34-dB coupler are compiled in Table 6.1. Central section coupled lines will be placed on top of layers L2 and L3. Sections 1 and 3 will be synthesized with offset-broadside-coupled lines over layers L2 and L4. They will be interconnected to the central section by means of vias. The cross section of the three-section 8.34-dB coupler is presented in Fig. 6.2. The coupler dimensions are also given in Table 6.1.

Table 6.1 Three-section 8.34-dB coupler characteristics, DuPont-951 substrate.

Parameter	Section1	Section2
Z_{oe} (Ω)	54.32	87.43
Z_{oo} (Ω)	46.02	28.59
Line width (μm)	210	150
Line spacing (μm)	618	0

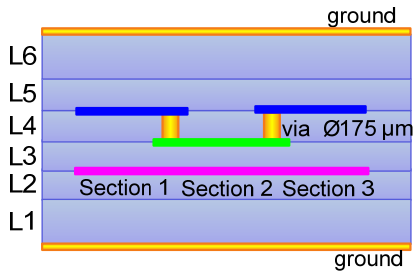

Fig. 6.2: Cross section of the LTCC 8.34-dB coupler, DuPont-951 substrate.

Two 8.34-dB couplers are connected in tandem to form the 3-dB coupler. Fig. 6.3 shows the top view of the LTCC 3-dB tandem coupler, whose dimensions are

20x4.7 mm. The simulated frequency response will be presented in Fig. 6.5-Fig. 6.7, together with the measurement results. All the simulations have been realized using the EMPIRE XCel 3D-EM field simulator from the IMST GMbH [134].

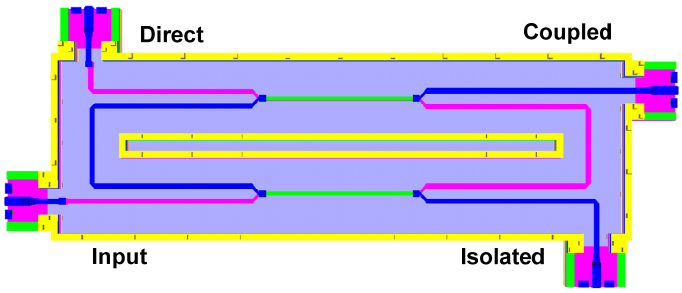

Fig. 6.3: Top-view of the LTCC 3-dB tandem coupler, DuPont-951 substrate.

The photograph of the constructed LTCC 3-dB tandem coupler is shown in Fig. 6.4. The circuit has been measured with good performance. Measured return loss and isolation, plotted in Fig. 6.5, are better than 20 dB from 1 to 7 GHz. Simulated and measured insertion losses are quite similar, as shown in Fig. 6.6, excepting for an additional 0.8 dB loss in the coupling level. Simulated and measured imbalances are presented in Fig. 6.7. Measured amplitude imbalance is below 2 dB from 1.5 to 6.5 GHz. Measured phase difference between direct and coupled ports varies from 91° to 98 between 1.5-6.5 GHz.

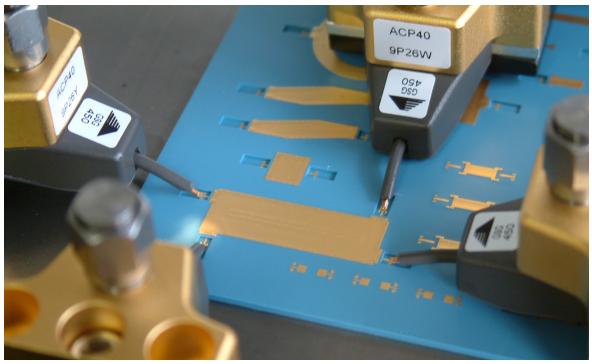

Fig. 6.4: Fabricated LTCC 3-dB tandem coupler, DuPont-951 substrate.

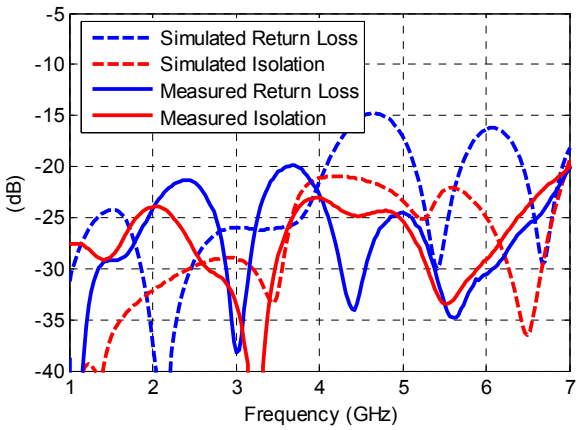

Fig. 6.5: Input return loss and isolation of the LTCC 3-dB tandem coupler, DuPont-951 substrate.

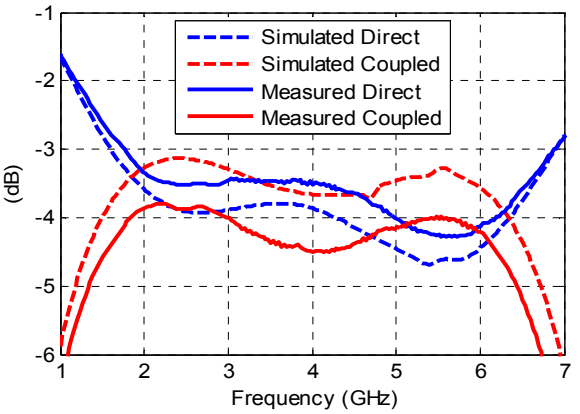

Fig. 6.6: Insertion loss of the LTCC 3-dB tandem coupler, DuPont-951 substrate.

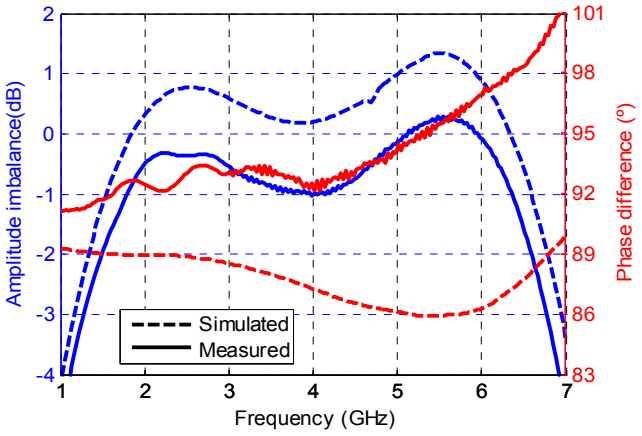

Fig. 6.7: Amplitude and phase imbalances of the LTCC 3-dB tandem coupler, DuPont-951 substrate.

6.3 LTCC SIX-PORT RECEIVER DESIGN AND SIMULATION

Once the viability of the technology was proved, the design of the complete LTCC six-port receiver was carried out. However, for this second realization, a new substrate with lower loss has been selected: the DuPont-943 (ε_r=7.4, tgδ=0.001@3GHz). DuPont-943 admits narrower layers than DuPont-951, being 42 µm the minimum layer thickness. Then, a wider bandwidth than that obtained with the DuPont-951 substrate could be achieved, since it is determined by the central section coupling level of the 3-dB tandem coupler.

The new layer structure is represented in Fig. 6.8. With this new layer structure, the three sections composing the 3-dB tandem coupler could be synthesized with offset-broadside-coupled lines over layers L3 and L5, avoiding the use of interconnection vias (see Fig. 6.2). A five-section coupler design could be also affordable, with the consequent bandwidth increment. Nevertheless, it would result in a larger size circuit, thereby a three-section coupler design will be maintained.

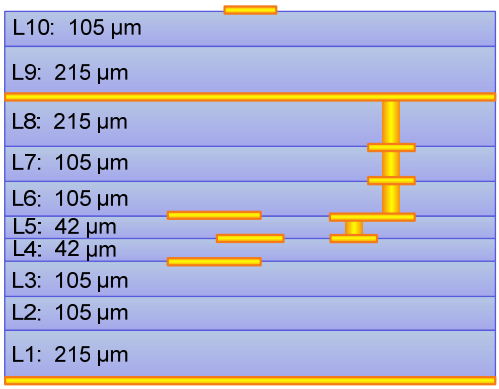

Fig. 6.8: LTCC layer structure using DuPont-943 substrate.

The detailed description of the different circuits composing the LTCC six-port receiver is presented below.

6.3.1 3-dB tandem coupler

The new stripline structure has a height of 934 µm. Then, the maximum theoretical coupling level achieved with two overlapped 50 Ω $\lambda/4$ broadside-coupled striplines, with a 84 µm separation, is 4.58 dB. It means that a five-section coupler

design could be also affordable, with the consequent bandwidth increment ($B=f_2/f_1=6.35$ for $\delta=0.35$ dB) [119]. Nevertheless, with five-section couplers the complete six-port receiver would result in a large size circuit, as three couplers and one power divider must be included.

Alternatively, if the three-section coupler design is maintained, the bandwidth can be extended by increasing the amplitude ripple. For example, a theoretical B=4.665 bandwidth can be obtained for $\delta=0.55$ dB, leading to a 1254-5850 MHz operating frequency range. In addition, with the new layer structure, the three sections composing the 3-dB tandem coupler can be synthesized with offset-broadside-coupled lines over layers L3 and L5, avoiding the use of interconnection vias in the previous design (see Fig. 6.2). Consequently, we will opt for a three-section coupler design.

The even and odd impedances for a symmetrical 3-section, ± 0.55 dB ripple level, 8.34-dB coupler are compiled in Table 6.2, together with the coupler dimensions. The lines of the three sections will be placed on top of layers L3 and L5, as shown in Fig. 6.9.

Table 6.2 Three-section 8.34-dB coupler characteristics, DuPont-943 substrate.

Parameter	Section1	Section2
Z_{oe} (Ω)	55.95	91.21
Z_{oo} (Ω)	44.67	27.4
Line width (μm)	250	145
Line spacing (μm)	645	130

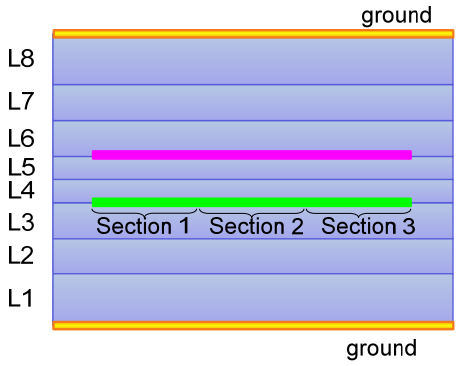

Fig. 6.9: Cross section of the LTCC 8.34-dB coupler, DuPont-943 substrate.

Fig. 6.10 shows the top view of the LTCC 3-dB tandem coupler, composed of two 8.34-dB couplers connected in tandem. Its simulated frequency response is presented in Fig. 6.11-Fig. 6.12. The simulated input return loss and isolation are

better than 20 dB from 0.5 to 6.5 GHz. The simulated insertion loss is 3 ± 0.5 dB from 1.22-5.88 GHz. The amplitude imbalance is below 2 dB from 1 to 6 GHz, while the phase difference between direct and coupled ports varies from 89.8º to 92 between 0.5-6.5 GHz.

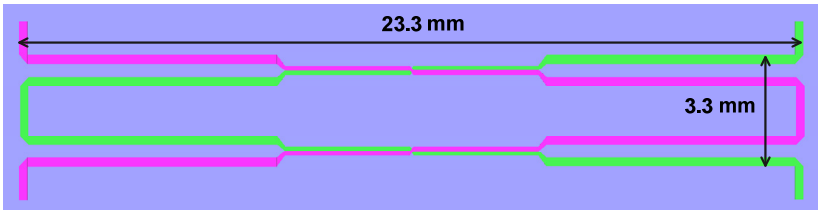

Fig. 6.10: Top-view of the LTCC 3-dB tandem coupler, DuPont-943 substrate.

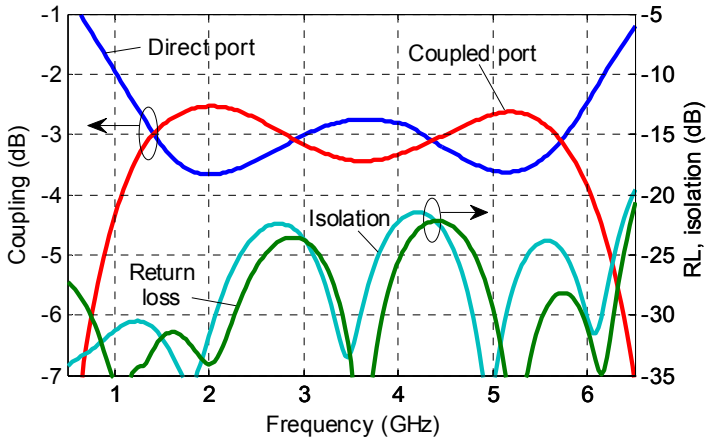

Fig. 6.11: Simulated frequency response of the LTCC 3-dB tandem coupler, DuPont-943 substrate.

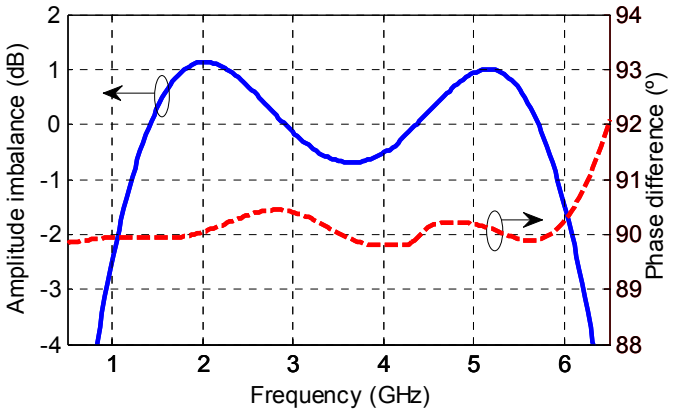

Fig. 6.12: Simulated amplitude and phase imbalances of the LTCC 3-dB tandem coupler, DuPont-943 substrate.

6.3.2 Wilkinson power divider

A multisection Wilkinson divider design is needed to cover the design frequency range of the 3-dB tandem coupler (1254-5850 MHz). From the design equations [135], and setting an input return loss better than 20 dB, we obtain that three sections are required to cover the operating frequency range. The Wilkinson divider will be implemented in microstrip using layers L1 and L2. The parameters of the 3-section Wilkinson divider are given in Table 6.3. The layout of the circuit and the EM simulated response (using EMPIRE) are presented in Fig. 6.13 and Fig. 6.14, respectively.

Table 6.3 Wilkinson divider characteristics, DuPont-943 substrate.

Design Parameters	**Section1**	**Section2**	**Section3**
Z_o (Ω)	57.77	70.71	86.54
R (Ω)	371.41	207.66	108.64
Implementation	**Section1**	**Section2**	**Section3**
Line width (μm)	285	185	100
R (Ω)	365	205	100

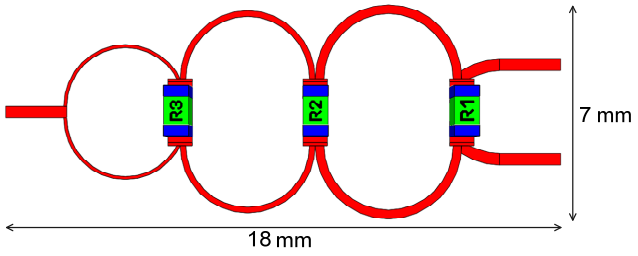

Fig. 6.13: Layout of the LTCC Wilkinson divider, DuPont-943 substrate.

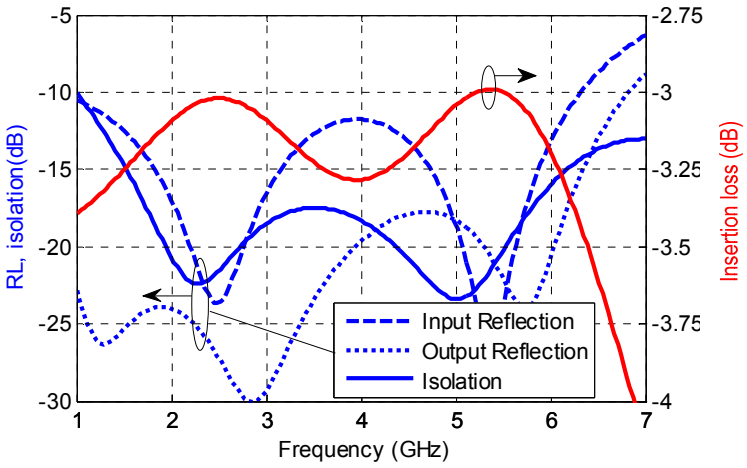

Fig. 6.14: Simulated frequency response of the LTCC Wilkinson divider.

6.3.3 LTCC six-port network

For the design of the six-port network, three 3dB tandem couplers and a Wilkinson divider have been connected according to the well known topology of Fig. 3.2. The top view of the LTCC six-port network, along with the scheme of the circuits' distribution in the layer structure, are presented in Fig. 6.15 (the ground metal located over layers L2 and L8 has been removed in the figure). The inputs and outputs of the six-port network are implemented in microstrip using layers L9 and L10. The design of a microstrip-to-stripline transition has been required to connect the couplers with the Wilkinson divider and with the outputs. For the interconnection between the LO input port and the Wilkinson divider, a microstrip-to-microstrip transition design has been also developed. The dimensions of the six-port network are 30x30x1.254 mm. Our purpose is to take advantage of the LTCC possibilities to develop a complete LTCC six-port receiver. Then, the free area over the three couplers will be used to locate the four power detectors and the low-frequency components. Furthermore, there is a central free space above the Wilkinson divider occupying layers L3 to L8, which can be used, for example, to locate a RF filter.

The EM simulated response of the LTCC six-port network will be presented in section 6.4.1, together with the measurement results.

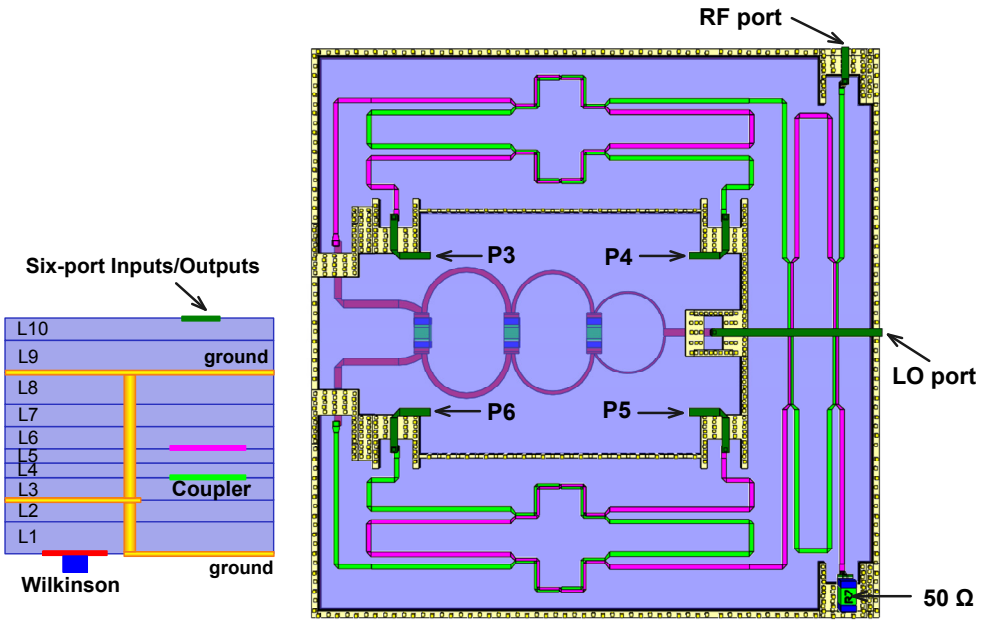

Fig. 6.15: Top-view of the LTCC six-port network.

6.3.4 Complete LTCC six-port receiver

Here we present the final design of the complete LTCC six-port receiver. The distribution scheme of the six-port receiver components can be seen in Fig. 6.16. The 3dB tandem couplers will be implemented in stripline using layers L1 to L8. The Wilkinson divider will be implemented in microstrip using the lower layers L1 and L2. The microstrip structure composed of the two upper layers L9 and L10 will be used to place the four power detectors, the low-frequency components, and the input/output access ports. The interconnection between the different layers will be made by means of vias (diameter=175 μm). These vias will be also used to build electrical walls in order to isolate the circuits composing the receiver.

Regarding to the power detectors, the same design considerations than in the previous six-port receiver has been followed (see section 3.3.2.2). A wide video bandwidth and high dynamic range detector design has been carried out, which leads to a high bias current. However, in this case a lower bias current has been selected in order to reduce the sensitivity degradation. A current value of I_b=0.5 mA will be used, instead of the previous 1 mA.

The low-pass filter has been substituted by a more compact device: the *Minicircuits* LFCV-45+. This filter has higher 3dB cut-off frequency (77 MHz), thereby wider channels could be supported (154 MHz-wide RF channels). However, as seen in Fig. 6.17(a), the LFCV-45+ filter does not provide a good short circuit around 1.1 GHz. To solve this problem, a 33 pF shunt capacitor has been placed before the low-pass filter, achieving the response plotted in Fig. 6.17(b).

The rest of the low-frequency components, i.e., the video amplifier and the high-pass filter for DC-offset cancellation, are the same than that used in the first six-port receiver prototype (see section 3.3.2.2).

The 3D view of the final LTCC six-port receiver is represented in Fig. 6.18. The dimensions of the LTCC six-port receiver are 30x30x1.254 mm. It is worth to mention that there is a free area of 238 mm^2 above the Wilkinson divider in layers L3-L8, which may still be occupied. One of the possibilities could be, for example, to locate a RF filter.

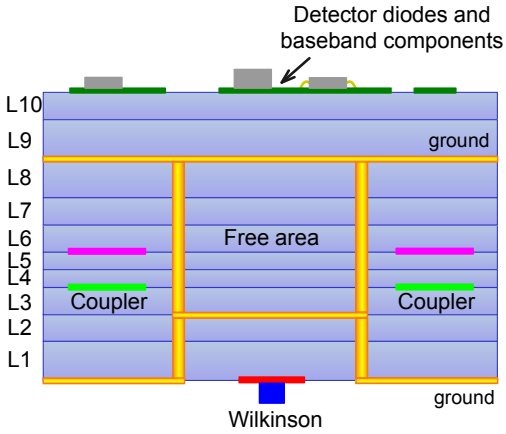

Fig. 6.16: Distribution of the six-port receiver circuits in the 10 layer LTCC structure.

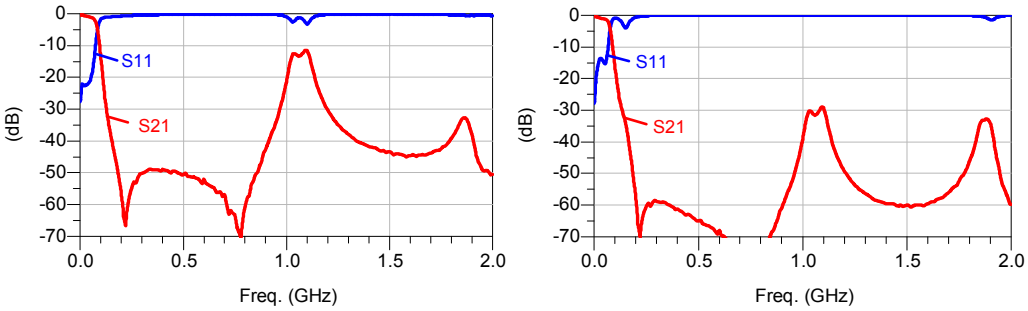

Fig. 6.17: Frequency response of the LFCV-45+ low-pass filter (a) without and (b) with a 33 pF capacitor.

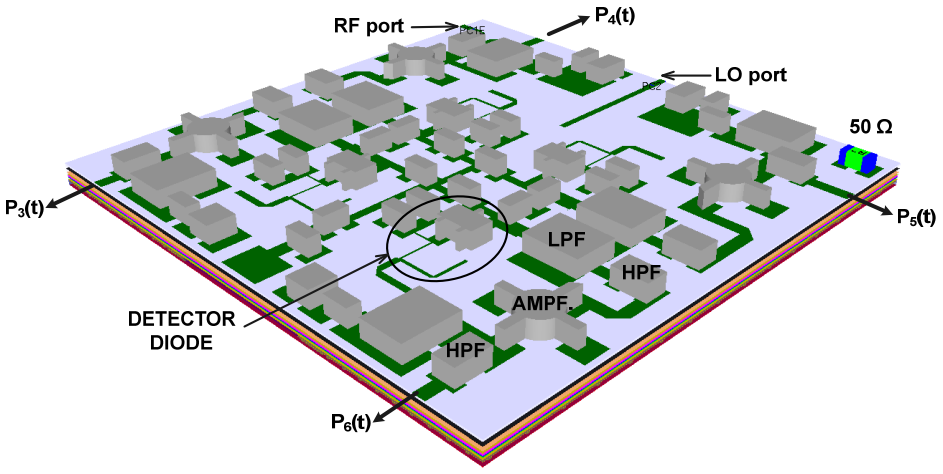

(a)

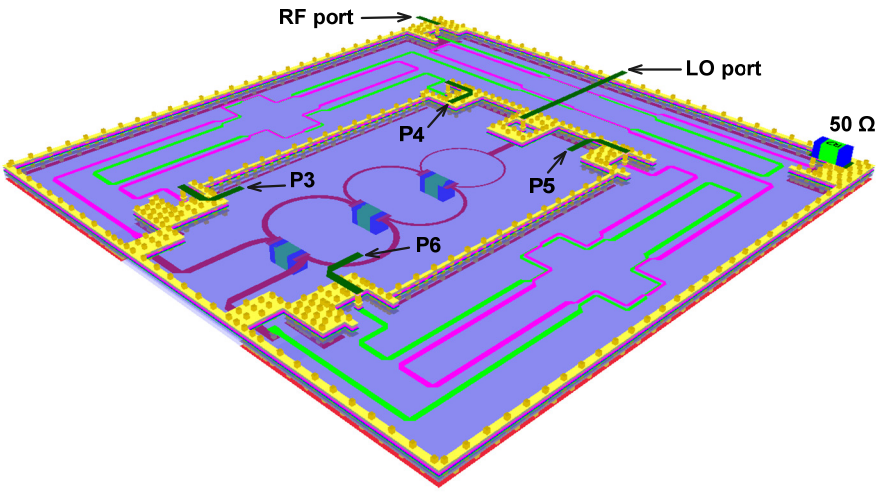

(b)

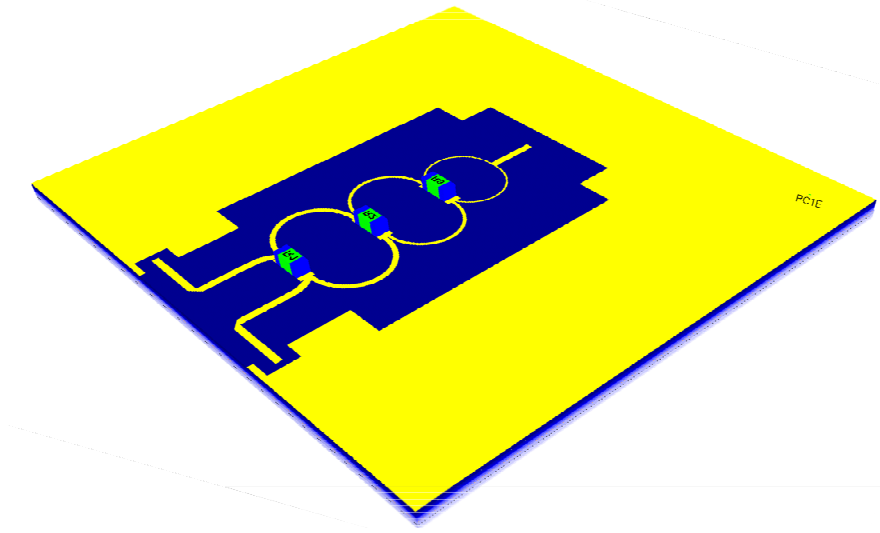

(c)

Fig. 6.18: 3D-view of the LTCC six-port receiver (a) top (b) layers L1-L8 (c) bottom.

6.4 IMPLEMENTATION AND EXPERIMENTAL CHARACTERIZATION

Completed the LTCC six-port receiver design, the circuit was fabricated by the IMST GMbH [134]. The photograph of the fabricated circuit is shown in Fig. 6.19, whose dimensions are 30x30x1.25 mm. A detail of the Wilkinson divider is presented in Fig. 6.20.

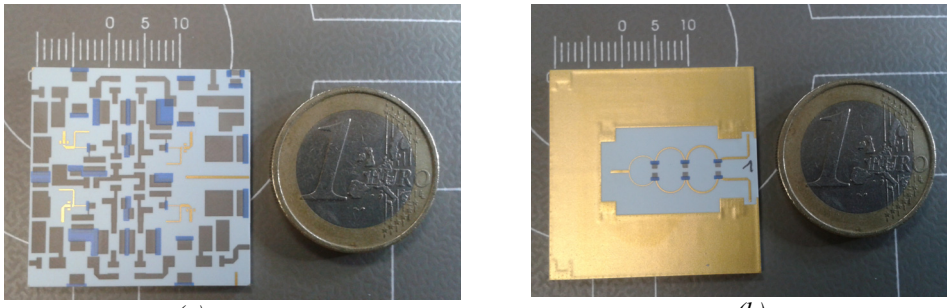

(a) (b)

Fig. 6.19: Fabricated LTCC six-port receiver (a) Top view (b) Bottom view.

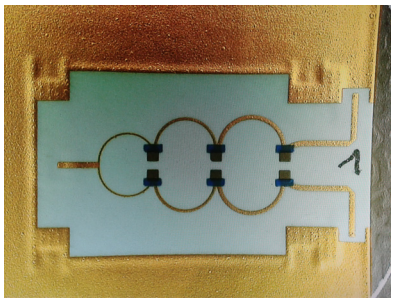

Fig. 6.20: Detail of the fabricated LTCC Wilkinson divider.

6.4.1 LTCC six-port network

Firstly, the scattering parameters of the LTCC six-port network will be measured. The measurement will be performed using a probe station, as shown in Fig. 6.21. The development of a test-platform composed of a metallic test-box and two access circuits has been required for the measurement, which can be seen in Fig. 6.22. In addition, the four output microstrip lines of the six-port network have not been joined to the detector diodes, and two ground patches have been placed at every output port for probe positioning. The detail of one output port can be seen in Fig. 6.23. Once the six-port network measurement has been made, the four output lines will be joined to the detector diodes. For this first measurement, only the 50 Ω resistor and the Wilkinson resistors need to be soldered.

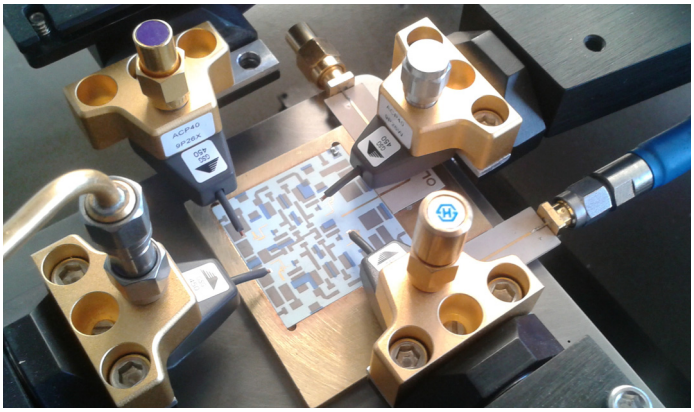

Fig. 6.21: Test-bench for the measurement of the six-port scattering parameters.

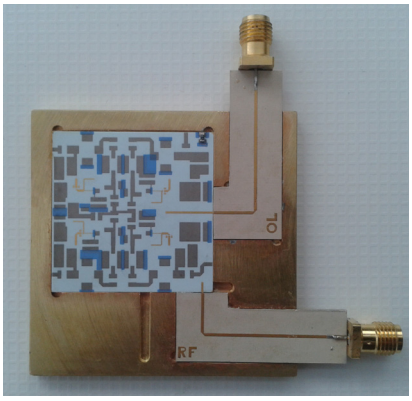

Fig. 6.22: Fabricated circuit test platform for the measurement of the six-port scattering parameters.

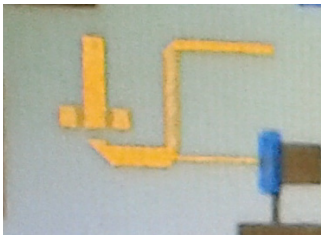

Fig. 6.23: Detail of one output port with ground patches for probe positioning.

The measured and simulated response of the LTCC six-port network is presented below. The responses of the additional elements required for the measurement, such as microstrip access circuits, probes, etc., have been removed by means of deembedding techniques. Fig. 6.24 shows the simulated and measured return loss and isolation of the six-port network. The measured return loss at the LO port, which is conditioned by the Wilkinson input reflexion, is in accordance with the

simulation results, with a value below 10 dB from 1GHz to 6 GHz. On the contrary, the measured return loss at RF port differs from the simulations, with worse values than expected. As for the measured RF-LO isolation, it is better than 20 dB up to 6.5 GHz.

Fig. 6.25 and Fig. 6.26 present, respectively, the simulated and measured attenuations from the LO and the RF ports. The simulated and measured curves present the same tendency, although additional losses are observed in the coupling levels, which can vary from 1 dB to 2 dB. Anyway, what is important is to maintain a good distribution of the q_i-points. Ideally, in this six-port topology the magnitudes of q_i-points are equal to 1, and the arguments differ 90 degrees. Fig. 6.27 shows the simulated and measured magnitudes of the q_i-points, while their phases are plotted in Fig. 6.28. The measured magnitudes of q_i are in the range of 0.5 to 1.8 from 1 GHz to 6 GHz. The behaviour of the curves below 1 GHz and above 6 GHz show that the operation range of the LTCC six-port receiver may be enlarged, as it happened with the first developed six-port receiver prototype. Regarding to the phase of the q_i-points, the maximum error in the relative phase differences is 20º over the theoretical value. This value may seem quite high; however, this deviation will be compensated by the calibration algorithm, as it will be seen in section 6.5.

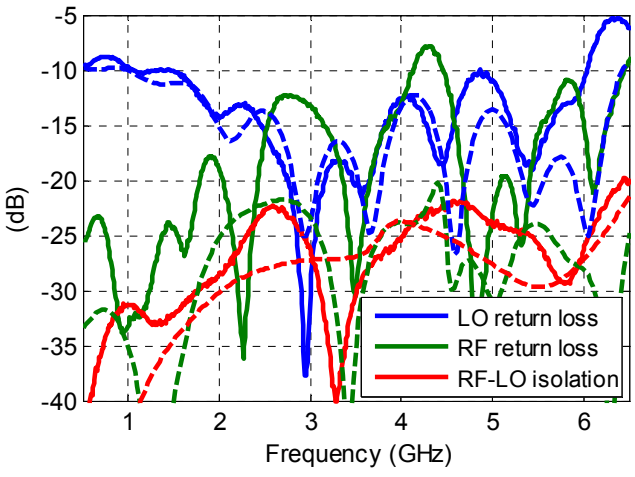

Fig. 6.24: Measured (solid line) and simulated (dashed line) input return loss and isolation.

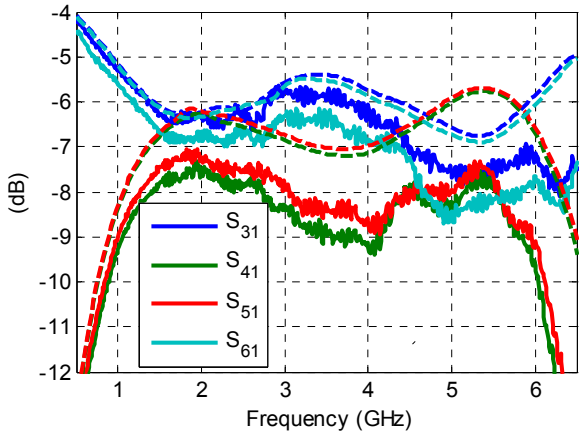

Fig. 6.25: Measured (solid line) and simulated (dashed line) attenuations from the LO port.

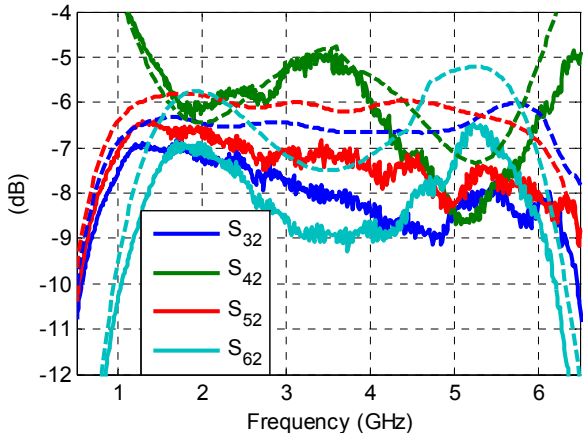

Fig. 6.26: Measured (solid line) and simulated (dashed line) attenuations from the RF port.

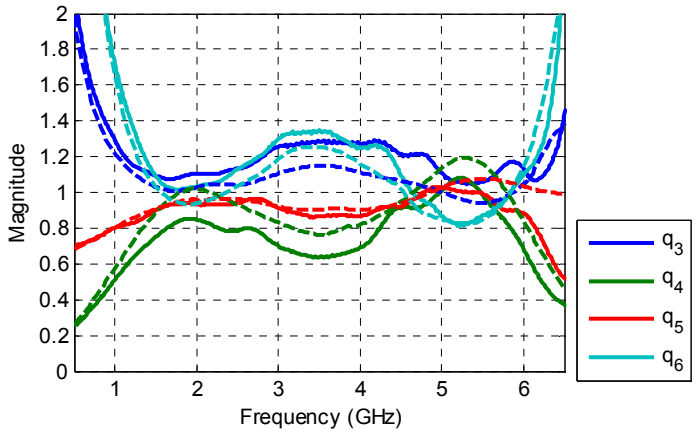

Fig. 6.27: Measured (solid line) and simulated (dashed line) magnitude of the q_i-points.

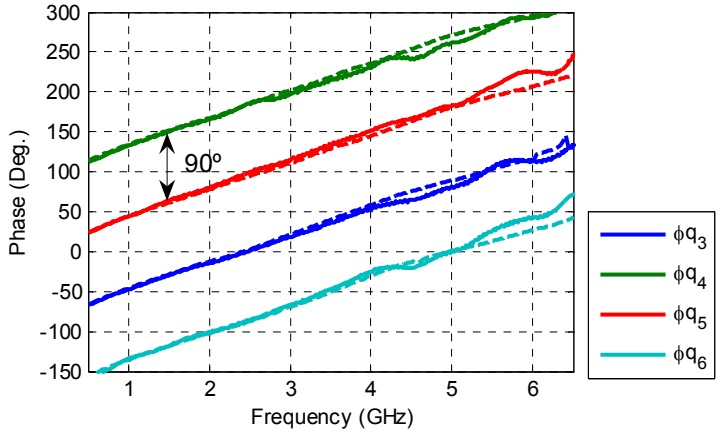

Fig. 6.28: Measured (solid line) and simulated (dashed line) phase of the q_i-points.

6.4.2 Complete LTCC six-port receiver prototype

Finally, after measuring the six-port network scattering parameters, the rest of the components were soldered to the LTCC circuit. The circuit was introduced into a metallic box, resulting in the final LTCC six-port receiver prototype. Its photograph can be seen in Fig. 6.29.

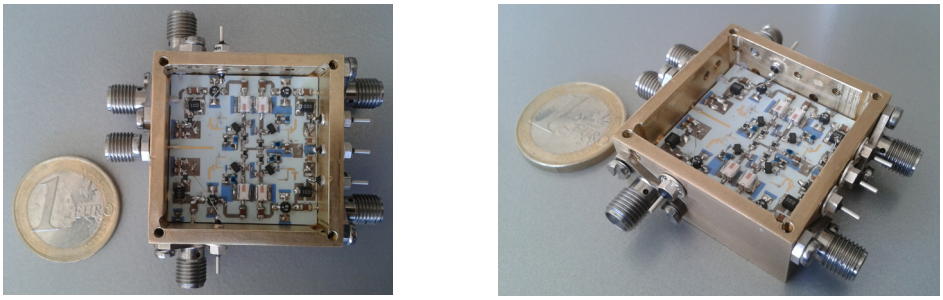

Fig. 6.29: Fabricated LTCC six-port receiver prototype.

The measured IF response of the fabricated LTCC six-port receiver (measured at port 3) is presented in Fig. 6.30. The value selected for the LO power level is 0 dBm. Fig. 6.31 shows the measured gain at the four output ports as a function of frequency, keeping f_{LO}-f_{RF}=5 MHz, while Fig. 6.32 shows the phase differences. Several problems appear clear: first, the measured gain at port 4 is larger than at the other ports; second, there is an undesirable attenuation at ports 3 and 5 for f=3GHz; and finally, the deviation of the phases from the ideal behaviour reaches to 40 º in the worst case. This would be a problem if the IQ regeneration were made analogically.

In our case, however, such errors will be compensated by the calibration in the digital domain, as it will be seen in section 6.5.

Table 6.4 summarizes the characteristics of the fabricated LTCC six-port receiver, measured for a LO power of 0 dBm.

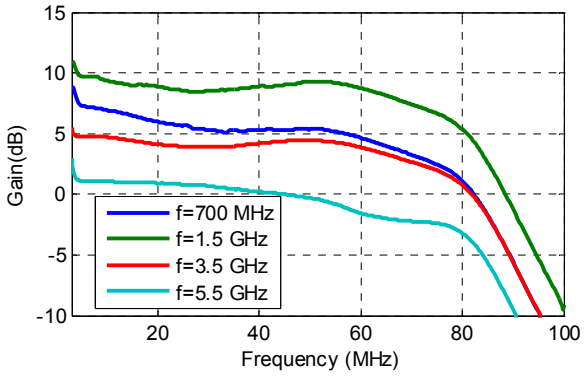

Fig. 6.30: Measured IF response of the LTCC six-port receiver (at Port 3).

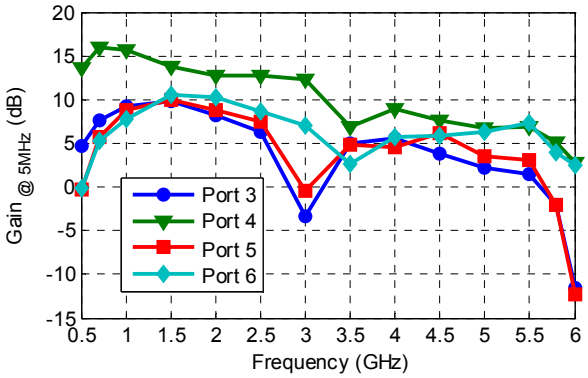

Fig. 6.31: Measured gain at the four output ports, f_{LO} - f_{RF} = 5 MHz.

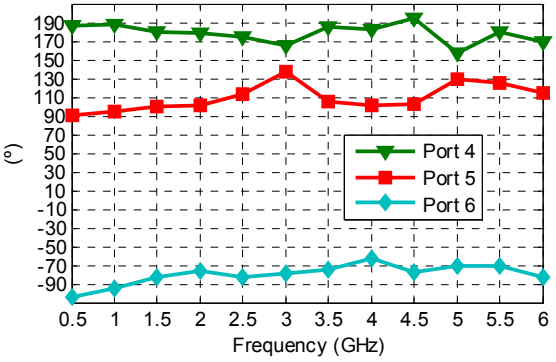

Fig. 6.32: Measured phase difference between output ports (Port 3 as reference port), f_{LO} - f_{RF} = 5 MHz.

Table 6.4 Measured LTCC six-port receiver characteristics, P_{LO}=0 dBm.

Parameter	Condition (MHz)	Value			Units
Max. Gain [1] DC-50 MHz	700	7.3			dB
	1500	9.7			
	2500	7.1			
	3500	4.8			
	4500	4.5			
	5500	1.5			
f_{c3dB} [1]	1500	74.9			MHz
	3500	76			
	5500	63.6			
Amplitude imbalance ΔA [2]	@ 5 MHz	Port 4	Port 5	Port 6	dB
	1500	4	0.2	0.71	
	3500	1.8	-0.1	-2.3	
	5500	5.5	1.6	5.8	
Phase difference $\Delta\Phi$ [2]	@ 5 MHz	Port 4	Port 5	Port 6	Deg. 82.6
	500	186.94	91.2	-104.3	
	1500	180.5	100	-82.6	
	3500	185.9	105.4	-74.7	
	5500	178.1	129	-70	
Output P_{1dB} [1]	700	7.8			dBm
	1500	5.6			
	3500	3.4			
	5500	5.6			
Spurious reject @-40 dBm	700	25.4			dB
	1500	32.2			
	2500	34.3			
	3500	35.4			
	4500	32.4			
	5500	33			

[1] Measured at port 3.
[2] With respect to reference port 3.

6.5 LTCC SIX-PORT DEMODULATION PERFORMANCE

Finally, the demodulation capability of the fabricated LTCC six-port receiver will be evaluated. The scheme of the test-bench is shown in Fig. 6.33. The *Agilent* E4438C ESG and N5182A MXG Vector Signal Generators (VSG) will be used for generating the RF modulated signal. The LO will be generated by the *Agilent* synthesized sweeper 83752A. The LO and RF signal generators will be phase locked. The output signals of the six-port receiver will be acquired by a four-channel oscilloscope (*Agilent Infiniium*), with an over-sampling ratio OSR=8. The calibration and I-Q regeneration software, implemented in *Matlab,* will be applied in a personal computer. The software does not include any diode linearization technique. The photograph of the test bench is presented in Fig. 6.34.

It is worth to mention that the maximum symbol rate that can be obtained with the E4438C ESG VSG is 12.5 Msymbol/s for an OSR=8. The *Agilent* N5182A MXG can provide 15.625 Msymbol/s for OSR=8, but it only operates up to 3 GHz. However, from the measured 3dB cut-off frequency (see Table 6.4), at least 127 Msymbol/s could be performed.

The LO power will be set to P_{LO}=0 dBm. After the acquisition of 1000 symbols (8000 samples, OSR=8), the data will be processed as bursts of length 200 symbols. The first 50 symbols of each burst will be used to auto-calibrate the system, and then the data sequence of length 150 symbols will be demodulated. The quality of the demodulated signal will be evaluated in terms of EVM.

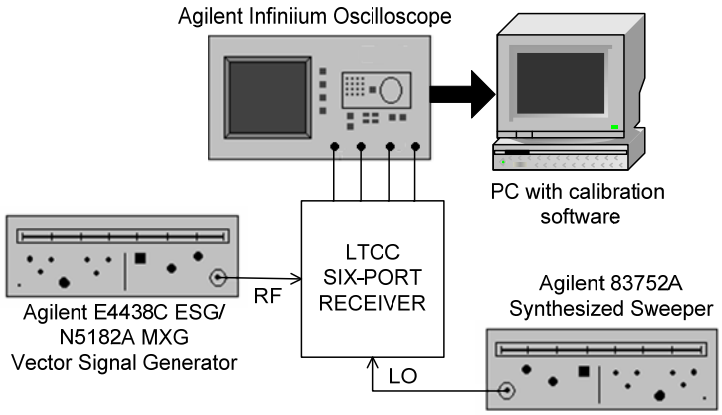

Fig. 6.33: Set-up of the LTCC six-port receiver test bench.

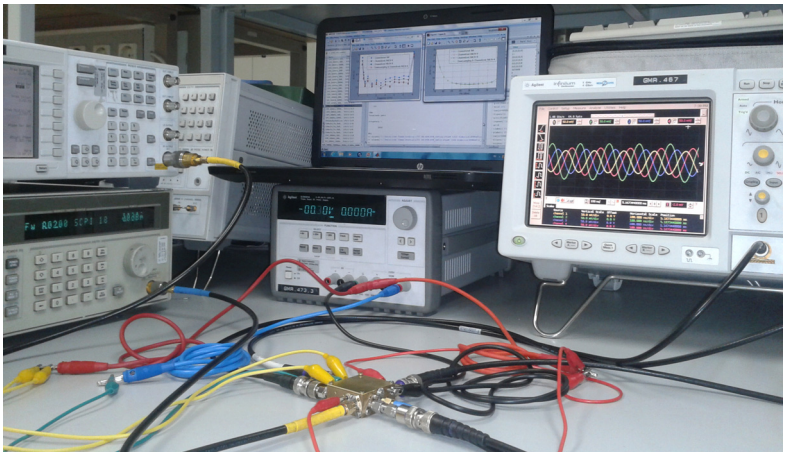

Fig. 6.34: Test bench for the measurement of the LTCC six-port receiver.

Fig. 6.35 shows the received constellation diagrams at 2.4 GHz and 15.625 Msymbol/s for different modulation schemes: 64-QAM, 16-QAM and QPSK. The measured EVM is around 3.7 % for the three cases. Fig. 6.36 plots the measured EVM as a function of the frequency. In this case, a -20 dBm 64-QAM signal at 12.5 Msymbols/s, i.e., data rate 75 Mbps, has been demodulated. These results show a good performance of the LTCC six-port receiver. The measured EVM is below 3.8 % from 700 MHz to 5.5 GHz, using the proposed channelized auto-calibration (AM) method with downsampling and four FIR filters. Moreover, the demodulation results demonstrate that the operating range of the LTCC six-port receiver can be extended from 300MHz to 6 GHz (4.32 octaves) with good performance, as it was expected. The measured EVM is below 5.75 % from 300 MHz to 6 GHz.

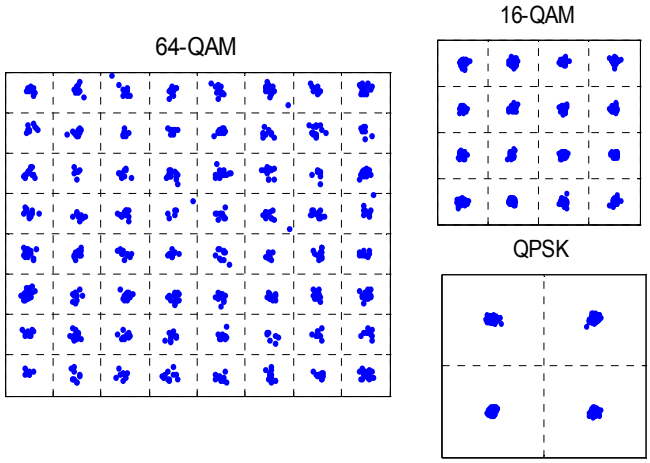

Fig. 6.35: Received constellations: 15.625 Msymbol/s, P_{LO}=0 dBm, P_{in}=-25 dBm, f=2.4 GHz.

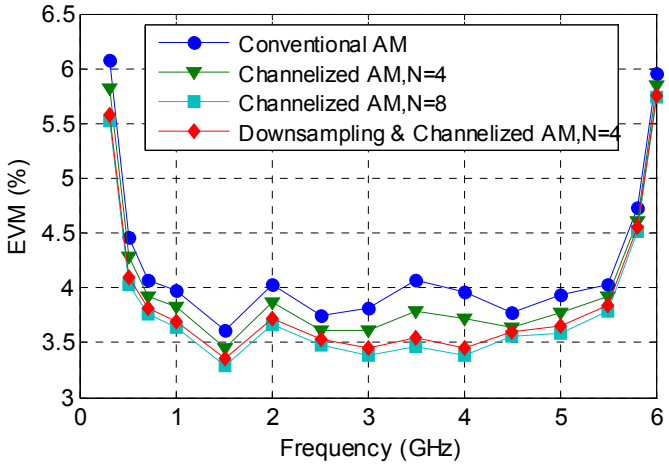

Fig. 6.36: Measured EVM versus frequency: 75 Mbps 64-QAM, P_{LO}=0 dBm, P_{in}=-20 dBm.

Fig. 6.37 shows the measured EVM as a function of P_{in} at 2.5 GHz. EVM curves show quality degradation for high levels of P_{in} due to nonlinear behaviour of the diodes and to the rectified wave, a baseband term superposed to the desired signal that increases quadratically with the signal power and, therefore, produces more degradation for high power levels. The results show significant EVM improvements, up to 0.5 percentage points with respect to conventional AM for N=8 filters or N=4 with downsampling. The measured EVM curve for a more extended range of P_{in} is plotted in Fig. 6.38, corresponding to the case downsampling and channelized AM with N=4. Fig. 6.39 presents the corresponding BER curves calculated from the measured EVM using (5-6). Note than in this case the EVM/BER improvement due to the use of the proposed channelized auto-calibration method is more significant than in the first six-port receiver (see Fig. 5.3), as the variation of the six-port parameters with frequency is stronger.

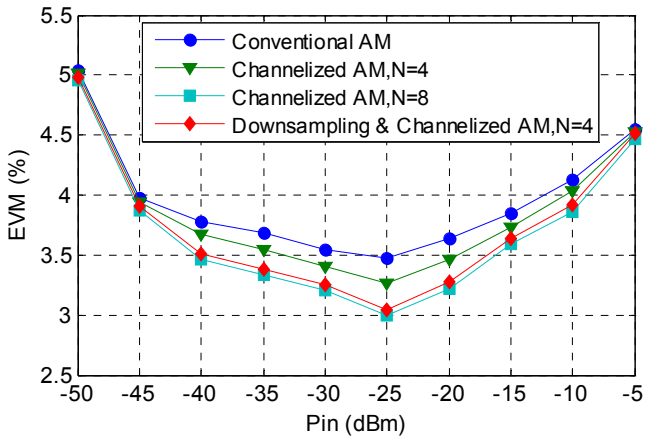

Fig. 6.37: Measured EVM versus P_{in}: 75 Mbps 64-QAM, P_{LO}=0 dBm, f=2.5 GHz.

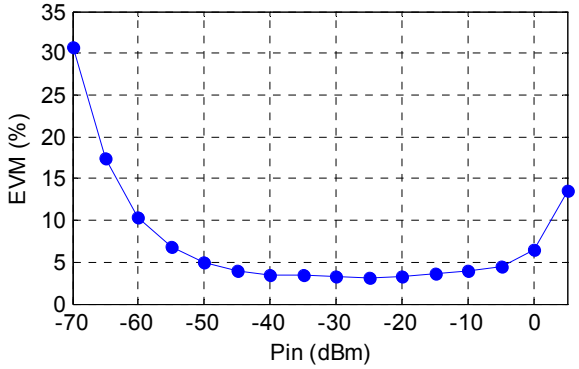

Fig. 6.38: Measured EVM versus P_{in}: 75 Mbps 64QAM, P_{LO}=0 dBm, f=2.5 GHz, Downsampling and Channelized AM, N=4.

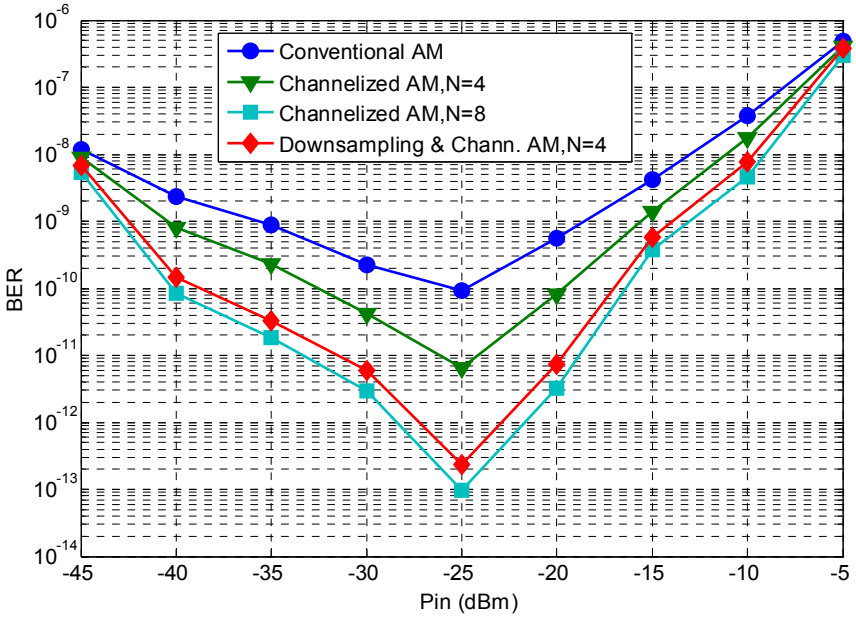

(a)

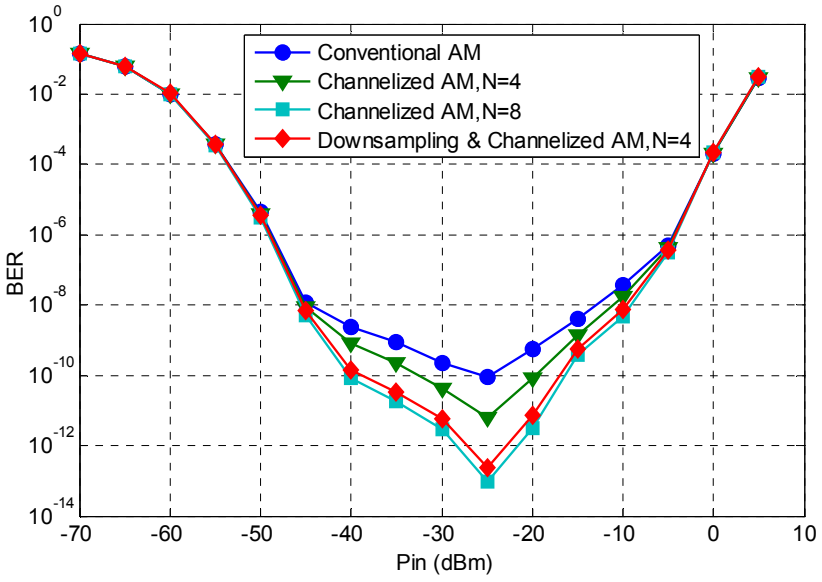

(b)

Fig. 6.39: BER calculated from measured EVM: 75 Mbps 64-QAM, P_{LO}=0 dBm, f=2.5 GHz (a) P_{in} from -45 dBm to -5 dBm, (a) P_{in} from -70 dBm to 5 dBm.

By defining the sensitivity as the RF input power to ensure a BER of 10^{-3}, we obtain a sensitivity value of -56.5 dBm at 2.5 GHz. Take into account that the LNA and the AGC stages have not been included in the receiver prototype. In addition, the dynamic range is 58 dB at BER<=10^{-3}. This is a high dynamic range compared with six-port receivers based on zero-biased detector diodes. For example, a 37.3 dB dynamic range at 2.4 GHz is measured in [105], despite that the response of the

detectors has been linearized using software techniques. On the contrary, we do not use any diode linearization technique.

Finally, the EVM has been measured for different LO power levels. Fig. 6.40 presents the measured EVM at 700 MHz, 3.5 GHz, and 5.8 GHz, using the channelized auto-calibration method with downsampling and four FIR filters. These results clearly demonstrate the capacity of the six-port receiver to operate with low values of LO power. This is an important advantage for SDR, as it entails low power consumption and cost reduction. In addition, problems derived from LO leakage and the self-mixing of LO, which are major drawbacks in direct conversion architectures, can be reduced.

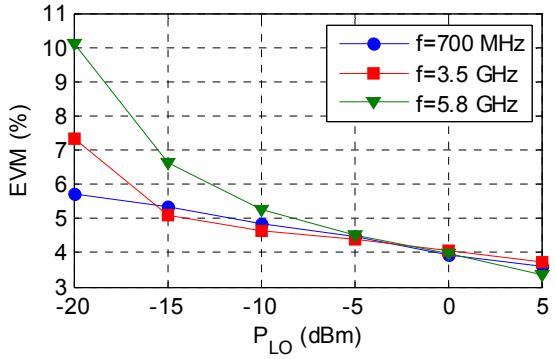

Fig. 6.40: Measured EVM versus P_{LO}: 25 Mbps QPSK, P_{in}=-20 dBm.

To conclude, the comparison with other multi-port demodulators operating in the frequency range of interest is presented in Table 6.5. Once again, we include the theoretical BER versus EVM curves for QPSK, 16-QAM and 64-QAM modulation schemes in Fig. 6.41 [126]. As it was previously commented in section 3.5.3, although the six-port receiver is said to be a good solution for the multi-band demodulation of high-speed signals, no many experimental demodulation results proving both assumptions have been published up to now. Some published works are not strictly multi-band [92],[104]; other are multi-band but only validate the demodulator for a single frequency [102],[106]; and other prove the multi-band behaviour but do not quantify the quality of the demodulated signal [101]. In [100],[105] the demodulation performance is quantified over the entire operating frequency range, but with data rates much lower than in our experiments. A six-port demodulator supporting a 1.67 Gbps data rate was published in [21]. However, this is not a broadband design, as it only covers the range from 7 to 8 GHz. In addition, the measured EVM is quite high, even

though the high LO power level (15 dBm). The two six-port receivers presented in this thesis outperform the other six-port receivers in terms of bandwidth, dynamic range, and quality of the demodulated signal. They have been validated over a four octave bandwidth (0.3-6 GHz), and for up to 93.75 Mbps data rates with very low values of EVM. However, the proposed LTCC six-port receiver not only outperforms the other receivers in these aspects, but also in terms of size: 30x30x1.25 mm. Other multilayer six-port designs have appeared in the literature [81],[136]-[137]. Nonetheless, they do achieve neither such a reduced size nor such large frequency range than the proposed LTCC six-port receiver. In addition, these publications do not provide any experimental demodulation results.

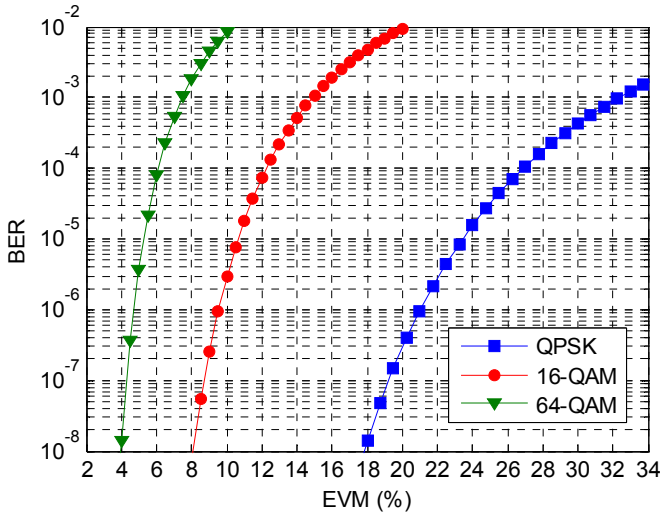

Fig. 6.41: Theoretical BER versus EVM curves.

Table 6.5 Comparison of six-port demodulators.

Ref.	Freq. band (GHz)	Measurement results				
		Data signal	P_{LO} (dBm)	P_{in} (dBm)	Freq. (GHz)	Quality of demodulated signal
[100] (2003)	0.9-5	97.2 Kbps QPSK	0	-20	0.9-4	EVM < 14 %
[92] (2004)	2-3	200 Kbps QPSK	0	-62.5	2	BER = 10^{-3}
[101] (2006)	2-9.4	8PSK	-	-19 -27 -31	2.4 5.8 9.4	Not quantified
[102] (2006)	0.9-4	1 Mbps QPSK	-10	-15	2.45	EVM = 12 %
[104] (2008)	3.1-4.8	1 Mbps QPSK	-1.5	-	3.432 3.96 4.488	EVM = 5.5 % EVM = 4 % EVM = 6.3 %
[105] (2009)	0.8-2.4	4 Mbps 16-QAM	-8.5	-33.3 to -2.6 -39.6 to -0.6 -38 to -0.7	0.8 1.6 2.4	BER < 10^{-3}
				≈ -32	1.6	BER = 10^{-6}
[106] (2010)	0.9-4	400 Kbps QPSK	-10	-20 -40	2.45	EVM = 5.9 % EVM = 7.9 %
[21] (2010)	7-8	1.67 Gbps 16-QAM	15	-15	7.5	EVM = 10.9 %
First work [PIER 2011] (2011)	0.3-6	75 Mbps 64-QAM	0	-20	0.3	EVM = 6.1 %
		62.5 Mbps 16-QAM			0.7	EVM = 4.8 %
		93.75 Mbps 64-QAM			2.45	EVM = 4.5 %
		25 Mbps QPSK			6	EVM = 4.4 %
		25 Mbps QPSK	-20	-20	1.8	EVM = 6.3 %
LTCC 6-port receiver (2012)	0.3-6	75 Mbps 64-QAM	0	-20	0.7-5.5 0.3-6	EVM < 3.8 % EVM < 5.75 %
				-56.5 to 1.5	2.5	BER<10^{-3}
		25 Mbps QPSK	-20 to +5	-20	0.7 3.5 5.8	EVM 5.75 - 3.6 % 7.3 - 3.7 % 10.1 - 3.3 %
		15.625 Msymbol/s 64-QAM 16-QAM QPSK	0	-25	2.4	EVM = 3.7 %

6.6 SUMMARY

This chapter represents the culmination of the thesis. On one hand, a new version of the broadband SDR six-port receiver has been developed based on LTCC technology. The new LTCC six-port receiver covers the same four octave bandwidth (0.3-6 GHz) than the first conventional technology six-port receiver. However, the size has been reduced to 30x30x1.25 mm in this new version. This work demonstrates empirically and quantitatively the multi-band behaviour of the six-port architecture, and the capability of performing high data rates. The demodulation of up to 15.625 Msymbol/s signals, i.e., 93.6 Mbps for 64-QAM, has been satisfactorily performed, with a measured EVM value of 3.7 %. Nevertheless, the LTCC six-port receiver can theoretically operate with at least 127 MHz instantaneous bandwidth, so a bit rate of 762 Mbps for a 64-QAM modulation is foreseen. The demodulation results show a good quality of the demodulated signal, with lower values of EVM than those published before in the literature. Once again, the benefits of the proposed channelized auto-calibration method have been experimentally proved in the LTCC six-port receiver. By using the proposed channelized auto-calibration method with four FIR filters and previous downsampling, an EVM below 3.8 % is achieved from 700 MHz to 5.5 GHz, and below 5.75 % from 300 MHz to 6 GHz. Furthermore, an important enhancement of the six-port receiver dynamic range has been achieved due to the use of biased detector diodes. It is worth to mention that we do not to use any digital diode linearization technique, which would extend the dynamic range for high power levels.

The contents of this chapter have been presented in the *European Microwave Conference 2011* [EuMC 2011], and in the *Simposium Nacional de la Unión Científica Internacional de Radio URSI 2010* [URSI 2010-1]. In addition, a paper describing the six-port network design and characterization has been accepted for the *Simposium Nacional de la Unión Científica Internacional de Radio URSI 2012* [URSI 2012]. Recently, a paper describing the complete LTCC six-port receiver has been submitted to the *IEEE Trans. Microwave Theory and Techniques* [MTT 2012-2].

Chapter 7

CONCLUSIONS AND PERSPECTIVE

7.1 CONCLUSIONS

This thesis is focused on the investigation and optimization of RF architectures for SDR implementation. Three RF architectures have been studied in detail in this thesis: zero-IF, low-IF, and six-port architecture. The six-port architecture shows high potential and advantages compared to conventional homodyne and heterodyne receivers for future communication systems, which will demand high bandwidths and high carrier frequencies. Therefore, this work has particularly focused on the study of this promising architecture.

The first contribution of this thesis is given in Chapter 3. It presents the experimental demonstration of the six-port architecture capabilities to implement a broadband SDR receiver. A SDR four-octave (0.3-6GHz) six-port receiver prototype has been developed in conventional technology. The six-port receiver has been measured with good performance over the frequencies of the main communication standards up to 6 GHz. The prototype has been validated for data rates of 93.75 Mbps (limited by the test instruments), although it has been designed to operate with 100 MHz instantaneous bandwidth, so a bit rate of 600 Mbps for a 64-QAM modulation is foreseen. This work demonstrates empirically and quantitatively the multi-band behaviour of the six-port architecture, and the capability of performing high data rates, outperforming previous results published by other authors.

Chapter 4 presents an experimental comparison between the three studied RF architectures. A zero-IF/low-IF receiver prototype has been developed for this purpose. The six-port receiver presents clear benefits over the other two architectures.

On one hand, it can operate with very lower values of LO power, keeping good quality of the demodulated signal. This is an important advantage for SDR, as it entails low power consumption, low cost, and reduction of the problems derived from LO leakage and the self-mixing of LO, which are major drawbacks in direct conversion architectures. On the other hand, the six-port receiver clearly outperforms the conventional zero-IF and low-IF receivers in terms of operating frequency range, and high-speed signal handling. The above six-port advantages have been experimentally demonstrated, although they were well known. However, two new and interesting conclusions are extracted from this work.

First, the capability of the six-port architecture to operate as both zero-IF and low-IF receivers has been demonstrated. The operation principle of six-port networks as both homodyne and heterodyne receivers is known from theory, although almost all six-port receiver implementations are direct frequency conversion architectures. Some heterodyne six-port receivers have been reported and demonstrated from simulations. However, heterodyne architecture is not a good option when a SDR hardware implementation is addressed. Here we have experimentally demonstrated that the advantages of both low-IF and zero-IF principles can be combined in a unique six-port receiver.

The second novelty is that the six-port receiver achieves larger dynamic range than the zero-IF/low-IF receiver. Multi-port architectures are said to present worse behaviour as for dynamic range compared to conventional homodyne and heterodyne architectures, as a consequence of the detector diode limitations. The reason is that six-port implementations typically use zero-bias detector diodes. On the contrary, we have biased the diodes in order to extend the square-law region. We have demonstrated that the use of a bias current has significant benefits in the dynamic range extension. The six-port receiver dynamic range has been extended to 58 dB. Therefore, we are not very far from the state-of-the-art high-speed ADCs, although more research must be done.

In effect, considering the 50 MHz video bandwidth, and an OSR=2, four 200 MSamples/s ADCs would be required. Table 7.1 shows several examples of commercial 200 MSamples/s ADCs. The 8-bit ADCs, while being the cheapest solution (from 30.68$ to 85$ for the four ADCs), do not achieve dynamic ranges above 46 dB. The dynamic range can be extended by increasing the resolution, at the

expense of the increment in cost and power consumption. A dynamic range similar to that obtained with our six-port receiver is achieved with 10-bit resolution (59-60 dB), with a prize between 100$ and 150$ for the four ADCs, and a power consumption from 1.3W to 2.3 W. The maximum dynamic range that can be obtained is around 74 dB by using 16-bit ADCs. However, for a SDR this solution is too expensive (400$) and requires a very high power consumption (5-8.6 W). Therefore, intensive research is needed not only in the analog front-end, but also in the digital part.

Table 7.1 Examples of commercial 200 MSPS ADCs.

Manufacturer	Part number	Bits	Sample Rate (MSPS)	Input channels	Dynamic range (dB)	Power consump. (mW)	Prize (US$)
Texas Instruments [138]	ADC08B200	8	200	1	45	543	16.5
	ADC08200	8	200	1	46	210	7.67
	ADC10DV200	10	200	2	59.8	450	50
	ADS58B18	11	200	1	67	310	27.4
	ADS5517	11	200	1	66	1230	41.15
	ADC11DV200	11	200	2	62.3	473	56
	ADS58C28	11	200	2	66.6	505	63.95
	ADS62C17	11	200	2	66.9	1081	66
	ADS58C48	11	200	4	66.6	900	111.95
	ADS5485	16	200	1	73.7	2160	98.95
Analog Devices [139]	AD9054A-200	8	200	1	43	781	21.22
	AD9211-250	10	200	1	59.4	353	39.47
	AD9211-200	10	200	1	59.5	333	32.38
	AD9601-200	10	200	1	59.5	344	32.38
	AD9230-11	11	200	1	62.8	373	36.43
	AD6657	11	200	4	66.3	1300	129.71
	AD9467-200	16	200	1	74.3	1240	100.3
Linear Technology [140]	LTC2241-10	10	210	1	60.5	585	32
	LTC2241-12	12	210	1	65.4	585	32
	LTC2156-12	12	210	2	68.4	592	55.43
	LTC2151-14	14	210	1	69.9	316	32.61
	LTC2156-14	14	210	2	69.9	605	55.43

Chapter 5 deals with a very important topic in multi-port receivers: the regeneration of the original IQ signals. Two new IQ regeneration techniques are introduced and validated. The first one is a real-time training-sequence-based channelized auto-calibration method for multi-port receivers. The channelized auto-calibration method is specially suited for broadband communications and strict requirements in the quality of service. Measurement results show a significant BER improvement, between one and two orders of magnitude with respect to conventional

auto-calibration methods. The second technique is an analog IQ regeneration technique for five-port receivers, based on the use of a simple IQ recovery circuit. This technique overcomes some typical drawbacks of five-port receivers. On one hand, it eliminates the calibration constants calculation (which entails a matrix inversion), and one baseband output, without any reduction in the operating frequency band. On the other hand, it improves the DC-offset and IMD2 rejection, which are main problems in direct conversion architectures.

The above contributions prove that the six-port receiver presents promising advantages and benefits. However, one important problem was still pending: the large size of six-port circuits. The bandwidth requirements of a RF front-end for SDR force to use multisection designs, which leads to large size circuits, especially for operating frequencies in the lower gigahertz region and conventional technology. Therefore, there was a need to explore new technologies in order to make the six-port network a viable and competitive solution for mobile terminals.

Chapter 6 represents the culmination of the thesis, where a new reduced version of the six-port receiver is developed in LTCC technology. Due to the use of the LTCC technology, the dimensions of the six-port receiver have been reduced to 30x30x1.25 mm. The LTCC six-port receiver covers the same four-octave frequency range (0.3-6 GHz), with excellent results in the demodulated of high-speed signals. These promising results may lead to reconsider the six-port architecture as an alternative for the lower gigahertz region, hence for mobile communication applications.

7.2 FUTURE RESEARCH WORK

One of the interesting research subjects for future work refers to the RF filtering. In a SDR implementation, multi-band or tuneable RF filters are needed to cover very large frequency ranges. Conventional multi-band filtering techniques have consisted of filter banks, with the disadvantage of the circuit size. Currently, the efforts are focused on the design of multi-band filters with an arbitrary number of pass-bands. Furthermore, microelectromechanical systems (MEMS) devices have displayed remarkable characteristics as variable devices, and have been applied as tuneable or

reconfigurable multi-band RF circuits. A very interesting work would be to integrate multi-band or MEMS tuneable filters on LTCC substrates.

One key topic in six-port architectures that needs intensive research is the extension of the dynamic range. In fact, this is a key drawback of broadband architectures. In this thesis we have proposed a high dynamic range detector design based on the use of a bias current. The detector design, however, can be further optimized. Another possibility is to investigate diode linearization techniques, in order to extend the square-law behaviour of the detectors. It would be very interesting to integrate a diode linearization technique into the calibration algorithm. Some diode linearization techniques have been reported. An exhaustive study of these linearization techniques is planned, as well as possible improvements and new solutions. Moreover, the investigation on DC-offset and IMD2 suppression techniques can be also interesting for dynamic range extension.

The investigation on new and improved real-time auto-calibration methods for multi-port receivers is also a future research work. The optimization of the proposed channelized auto-calibration method is one of our future objectives. On one hand, it is worth studying new families of filters, in order to improve the calibration performance. For example, we could think of a family with more selective filters. On the other hand, it would be interesting to develop an FPGA implementation of the channelized auto-calibration algorithm. The analysis of several parameters, such as run-time resource consumption, execution time, etc. would be interesting.

To conclude, other possible future research lines could be focused on the digital part. Without going far from the RF framework, since digital signal processing is an extremely wide field, one interesting point would be, for example, the investigation on carrier recovery algorithms, which can make use of the extra amount of information available in the four output ports.

BIBLIOGRAPHY

[1] The Software Defined Radio Forum (SDRF). http://www.sdrforum.org.

[2] A.C. Tribble, "The software defined radio: Fact and fiction," in *IEEE Radio and Wireless Symp.,* Jan. 2008, pp.5–8.

[3] B. Kelley, "Software defined radio for broadband OFDM protocols," in *IEEE Int. Conf. Systems, Man and Cybernetics,* Oct. 2009, pp. 2309–2314.

[4] J.L. Shanton, "A software defined radio transformation," in *IEEE Military Communications Conf.,* Oct. 2009, pp.1–5.

[5] Joint Program Executive Office for the Joint Tactical Radio System Homepage: http://jpeojtrs.mil.

[6] Project 25 Technology Interest Group Homepage: http://www.project25.org.

[7] Project MESA Homepage: http://www.projectmesa.org.

[8] J. Mitola, “The software radio architecture,” *IEEE Commun. Mag.*, vol. 33, no. 5, pp. 26–38, May. 1995.

[9] A. Bourdoux, J. Craninckx, A. Dejonghe, L. Van der Perre, "Receiver Architectures for Software-defined Radios in Mobile Terminals: the Path to Cognitive Radios," in *IEEE Radio Wireless Symp.*, Jan. 2007, pp.535–538.

[10] A.A. Abidi, "The Path to the Software-Defined Radio Receiver," *IEEE J. Solid-State Circuits*, vol. 42, no. 5, pp. 954–966, May 2007.

[11] M. Puvaneswari, O. Sidek, "Wideband analog front-end for multistandard software defined radio receiver," in *IEEE* 15th *Int. Symp. Personal, Indoor and Mobile Radio Communications,* Sept. 2004, vol. 3, pp. 1937–1941.

[12] M. Brandolini, P. Rossi, D. Manstretta, F. Svelto, "Toward multistandard mobile terminals-fully integrated receivers requirements and architectures," *IEEE Trans. Microw. Theory Tech.,* vol. 53, no. 3, pp. 1026–1038, Mar. 2005.

[13] J.-F. Luy, T. Mueller, T. Mack, A. Terzis, "Configurable RF receiver architectures," *IEEE Microw. Mag.,* vol. 5, no. 1, pp. 75–82, Mar. 2004.

[14] R.G. Bosisio, Y.Y. Zhao, X.Y. Xu, S. Abielmona, E. Moldovan, Y.S. Xu, M. Bozzi, S.O. Tatu, C. Nerguizian, J.F. Frigon, C. Caloz, K. Wu, "New-Wave Radio," *IEEE Microwave Magazine*, vol. 9, no. 1, pp. 89–100, Feb. 2008.

[15] M. Mohaer, A. Mohammadi, A. Adipour, “Direct conversion receivers using multi-port structures for software defined radio systems,” *IET Microw. Antennas & Propag.,* vol. 1, no. 2, pp. 363–372, April 2007.

[16] A. Koelpin, G. Vinci, B. Laemmle, D. Kissinger, R. Weigel, “The six–port in modern society,” *IEEE Microw. Magazine,* vol. 11, no. 7, pp. 35–43, Dec. 2010.

[17] X. Xu, R.G. Bosisio, K. Wu, "Analysis and implementation of six-port software-defined radio receiver platform," *IEEE Trans. Microw. Theory Tech.,* vol. 54, no. 7, pp. 2937–2943, July 2006.

[18] R. Mirzavand, A. Mohammadi, "Five-port receiver implementation in Ka-band for software-defined radio," in *Asia-Pacific Microwave Conf.,* Dec. 2006, pp. 480–483.

[19] N.K. Mallat, S.O Tatu, "Six-port receiver in millimeter-wave systems," in *IEEE Int. Conf. Systems, Man and Cybernetics,* Oct. 2007, pp. 2693–2697.

[20] G. Wu, Z. Liu, R.M. Weikle, "A millimeter-wave sampled-line six-port reflectometer at 300GHz," in *Joint 32nd Int. Conf Infrared and Millimeter Waves, and 15th Int. Conf. Terahertz Electronics,* Sept. 2007, pp. 775–776.

[21] J. Östh, A. Serban, Owais, M. Karlsson, S. Gong, J. Haartsen, P. Karlsson, “Six-port gigabit demodulator”, *IEEE Trans. Microwave Theory Tech.*, vol. 59, no. 1, pp. 125–131, Jan. 2010.

[22] F.M. Colebrook, “Homodyne,” *Wireless World and Radio Rev*., 13, pp. 645–648, 1924.

[23] E.H. Armstrong, "The super-heterodyne-Its origin, development, and some recent improvements," *Proc. Institute of Radio Engineers*, vol. 12, no. 5, pp. 539–552, Oct. 1924.

[24] D.G. Tucker, “The history of the homodyne and synchrodyne," *J. British Inst. Radio Engineers*, vol. 14, no. 4, pp. 143–154, April 1954.

[25] A. Bateman, D.M. Haines, “Direct conversion transceiver design for compact low-cost portable mobile radio terminals,” in *Proc. IEEE Veh. Technol. Conf.*, May 1989, pp. 57–62.

[26] A.A. Abidi, “Direct conversion radio transceiver for digital communications,” *IEEE J. Solid-State Circuits*, vol. 30, no. 12, pp. 1399–1410, Dec. 1995.

[27] B. Razavi, “Design considerations for direct-conversion receivers,” *IEEE Trans. Circuits Syst.*, vol. 44, no. 6, pp. 428–435, Jun. 1997.

[28] R. Svitek, S. Raman, “DC offsets in direct-conversion receivers: characterization and implications,” *IEEE Microw. Mag.*, vol. 6, no. 3, pp. 76–86, Sept. 2005.

[29] J.F. Wilson, R. Youell, T.H. Richards, G. Luff, R. Pilaski, “A single-chip VHF and UHF receiver for radio paging,” *IEEE J. Solid-State Circuits*, vol. 26, no. 12, pp. 1944–1950, Dec. 1991.

[30] Z. Zhang, J. Lau, “A flicker-noise-free dc-offset-free harmonic mixer in a CMOS process,” in *Proc. IEEE Radio Wireless Conf.*, Aug. 2001, pp. 113–116.

[31] T. Yamaji, H. Tanimoto, H. Kokatsu, “An I/Q active balanced harmonic mixer with IM2 cancelers and a 45-degree phase shifter,” *IEEE J. Solid-State Circuits*, vol. 33, no. 12, pp. 2240–2246, Dec. 1998.

[32] J. Wang, J. Wang, Y. Huang, W. Shen, X. Yi, Z. Hong, “A direct conversion WLAN receiver,” in *Int. Conf. ASIC*, Oct. 2005, vol. 1, pp. 374–377.

[33] S.-M. Oh, K.-S. Park, H.-H. Yoo, Y.-S. Na, T.-S. Kim, “A design of DC offset canceller using parallel compensation,” in *IEEE Int. Symp. Circuits Syst.*, May 2007, pp.1685–1688.

[34] H. Yoshida, H. Tsurumi, Y. Suzuki, “DC offset canceller in a direct conversion receiver for QPSK signal reception,” in *IEEE Int. Symp. Personal, Indoor, Mobile Radio Commun.*, Sept. 1998, vol. 3, pp. 1314–1318.

[35] S. Hsu, W. Namgoong “An AC-coupled direct-conversion receiver for Global Positioning System,” in *IEEE Int. Symp. Circuits Syst.*, May 2005, vol. 4, pp. 3235–3238.

[36] W. Namgoong, “DC-Offset and 1/f noise effects on AC-coupled direct-conversion receiver,” in *IEEE Midwest Symp. Circuits Syst.,* Aug. 2001, vol. 2, 886–889.

[37] S. Sampei, K. Feher, “Adaptive dc-offset compensation algorithm for burst mode operated direct-conversion receiver,” in *IEEE Vehicular Technology Conf.*, May 1992, vol. 1, pp. 93–96.

[38] W. Namgoong, T. H. Meng, “Direct-conversion RF receiver design”, *IEEE Trans. Communications*, vol. 49, no. 3, pp. 518–529, Mar. 2001.

[39] S. Zhou, M.-C. Frank Chang, “A CMOS passive mixer with low flicker noise for low-power direct-conversion receiver,“ *IEEE J. Solid-State Circuits*, vol. 40, no. 5, pp. 1084–1093, May 2005.

[40] J. Park, C.-H. Lee, B.-S. Kim, J. Laskar, "Design and analysis of low flicker-noise CMOS mixers for direct-conversion receivers", *IEEE Trans. Microw. Theory Tech.*, vol. 54, no. 12, pp. 4372–4380, Dec. 2006.

[41] I. Elahi, K. Muhammad, P.T. Balsara, "IIP2 and DC offsets in the presence of leakage at LO frequency", *IEEE Trans. Circuits Syst. II: Express Briefs*, vol. 53, no. 8, pp. 647–651, Aug. 2006.

[42] E.E. Bautista, B. Bastani, J. Heck, "A high IIP2 downconversion mixer using dynamic matching," *IEEE J. Solid-State Circuits*, vol. 35, no. 12, pp. 1934–1941, Dec. 2000.

[43] S.J. Fang, S.T. Lee, D.J. Allstot, A. Bellaouar, "A 2 GHz CMOS even harmonic mixer for direct conversion receivers," in *IEEE Int. Symp. Circuits Syst.,* Aug. 2002, vol. 4, pp. 807–810.

[44] M. Hotti, J. Ryynanen, K. Halonen, "IIP2 calibration methods for current output mixer in direct-conversion receivers", in *IEEE Int. Symp. Circuits Syst.*, May 2005, vol. 5, pp. 5059–5062.

[45] K. Dufrene, Z. Boos, R. Weigel, "Digital adaptive IIP2 calibration scheme for CMOS downconversion mixers", *IEEE J. Solid-State Circuits*, vol. 43, no. 11, pp. 2434–2445, Nov. 2008.

[46] J. Ryynanen, K. Kivekas, J. Jussila, L. Sumanen, A. Parssinen, K.A.I Halonen, "A single-chip multimode receiver for GSM900, DCS1800, PCS1900, and WCDMA," *IEEE J. Solid-State Circuits*, vol. 38, no. 4, pp. 594–602, Apr. 2003.

[47] Y.-J. Kim, Y.-S. Son, V.N. Parkhomenko, I.-C. Hwang, J.-K. Cho. K.-S. Nah. B.-H. Park, "A GSM/EGSM/DCS/PCS direct conversion receiver with integrated synthesizer," *IEEE Trans. Microw. Theory Tech.*, vol. 53, no. 2, pp. 606–613, Feb. 2005.

[48] G. Cafaro, T. Gradishar, J. Heck, S. Machan, G. Nagaraj, S. Olson, R. Salvi, B. Stengel, B. Ziemer, "A 100 MHz - 2.5 GHz direct conversion CMOS transceiver for SDR applications", in *IEEE Radio Frequency Integrated Circuits Symp.*, Jun. 2007, pp. 189–192.

[49] R. Bagheri, A. Mirzaei, S. Chehrazi, M.E. Heidari, L. Minjae, M. Mikhemar, T. Wai, A.A. Abidi, "An 800-MHz-6-GHz software-defined wireless receiver in 90-nm CMOS," *IEEE J. Solid-State Circuits*, vol. 41, no. 12, pp. 2860–2876, Dec. 2006.

[50] M. Ingels, C. Soens, J. Craninckx, V. Giannini, T. Kim, B. Debaillie, M. Libois, M. Goffioul, J. Van Driessche, "A CMOS 100 MHz to 6 GHz software defined radio analog front-end with integrated pre-power amplifier," in *European Solid State Circuits Conf.,* Sept. 2007, pp.436–439.

[51] Epiq Solutions: http://epiqsolutions.com/matchstiq

[52] FUNcube Dongle: http://www.funcubedongle.com

[53] Lime Microwystams: http://www.limemicro.com

[54] T.S. Rappaport, J.N. Murdock, F. Gutierrez, "State of the Art in 60-GHz Integrated Circuits and Systems for Wireless Communications", *Proc. of the IEEE*, vol. 99, no. 8, pp. 1390–1436, Aug. 2011.

[55] J. Crols, M.S.J. Steyaert, "Low-IF topologies for high-performance analog front ends of fully integrated receivers," *IEEE Tran. Circuits Syst. II: Analog and Digital Signal Processing*, vol. 45, no. 3, pp.2 69–282, Mar. 1998.

[56] R. Hartley, “Single-sideband modulator,” U.S. Patent 1 666 206, Apr. 1928.

[57] D. K. Weaver, “A third method of generation and detection of singlesideband signals,” *Proc. IRE*, vol. 44, pp. 1703–1705, 1956.

[58] J.P.F. Glas, "Digital I/Q imbalance compensation in a low-IF receiver", in *IEEE Global Telecommunications Conf.,* 1998*,* vol. 3, pp. 1461–1466.

[59] I. Elahi, K. Muhammad, P.T. Balsara, "I/Q mismatch compensation using adaptive decorrelation in a low-IF receiver in 90-nm CMOS process," *IEEE J. Solid-State Circuits,* vol. 41, no. 2, pp. 395–404, Feb. 2006.

[60] A. Gimeno-Martin, J.M. Pardo-Martin, F.J. Ortega-Gonzalez, "Adaptive algorithm for increasing image rejection ratio in low-IF receivers," *Electronics Letters*, vol. 44, no. 6, pp. 447–448, Mar. 2008.

[61] H. Yoshida, S. Otaka, T. Kato, H. Tsurumi, "A software defined radio receiver using the direct conversion principle: implementation and evaluation," in *11th IEEE Int. Symp. Personal, Indoor & Mobile Radio Communications, 2000*, vol. 2, pp.1044–1048.

[62] C. Carta, R. Vogt, W. Bachtold, "Multiband monolithic BiCMOS low-power low-IF WLAN receivers," *IEEE Microwave and Wireless Components Letters,* vol. 15, no. 9, pp. 543–545, Sept. 2005.

[63] H. Darabi, J. Chiu, S. Khorram, H.J. Kim, Z. Zhou, H.-M. Chien, B. Ibrahim, E. Geronaga, L.H. Tran, A. Rofougaran, "A dual-mode 802.11b/bluetooth radio in 0.35-µm CMOS," *IEEE J. Solid-State Circuits,* vol. 40, no. 3, pp. 698–706, Mar. 2005.

[64] P.-I. Mak; S.-P. U; R.P. Martins, "Two-step channel selection-a novel technique for reconfigurable multistandard transceiver front-ends," *IEEE Trans. Circuits Syst. I: Regular Papers*, vol. 52, no. 7, pp. 1302–1315, July 2005.

[65] M. Kitsunezuka, T. Tokairin, T. Maeda, M. Fukaishi, "A low-IF/zero-IF reconfigurable analog baseband IC with an I/Q imbalance cancellation scheme", *IEEE J. Solid-State Circuits*, vol. 46, no. 3, pp. 572–582, Mar. 2011.

[66] C. A. Hoer, “The six-port coupler: a new approach to measuring voltage, current, power, impedance and phase,” *IEEE Trans. Instrum. Meas*., vol. 21, no. 4, pp. 466-470, Nov. 1972.

[67] G. F. Engen, and C. A. Hoer, “Application of an arbitrary 6-port junction to power-measurement problems,” *IEEE Trans. Instrum. Meas*., vol. 21, no. 4, pp. 470-474, Nov. 1972.

[68] C. A. Hoer, and K. C. Roe, "Using an arbitrary six-port junction to measure complex voltage ratios," *IEEE-MTT-S Int. Microwave Symposium,* 12-14 May 1975, pp.98-99.

[69] G. F. Engen, “The six-port reflectometer an alternative network analyzer,” *IEEE Trans. Microw. Theory Tech.*, vol. MTT-25, pp. 1075–1079, Dec. 1977.

[70] T. Hentschel, "The six-port as a communications receiver," *IEEE Trans. Microw. Theory Tech.*, vol.53, no.3, pp. 1039-1047, March 2005.

[71] F.M. Ghannouchi, A. Mohammadi, “The six-port technique with microwave and wireless applications,” Artech House, 2009, Norwood, MA.

[72] G. F. Engen, “A (historical) review of the six-port measurement technique,” *IEEE Trans. Microw. Theory Tech.*, vol. 45, no. 12, pp. 2414–2417, Dec. 1997.

[73] L. Kaliouby, R.G Bosisio, “A new method for six–port swept frequency automatic network analysis,” *IEEE Trans. Microw. Theory Tech.*, vol. 32, no. 12, pp. 1678–1682, 1984.

[74] M. Berman, P.I. Somlo, M.J. Buckley, “A comparative statistical study of some proposed six-port junctions designs,” *IEEE Trans. Microw. Theory Tech.*, vol. 35, no. 11, pp. 971–977, Nov. 1987.

[75] E.R.B Hansson, G.P. Riblet, "An ideal six-port network consisting of a matched reciprocal lossless five-port and a perfect directional coupler," *IEEE Trans. Microw. Theory Tech.*, vol. 31, no.3, pp.284-288, Mar. 1983.

[76] V. Bilik, J. Bezek, "Vector reflectometer system for industrial applications," in *24th European Microwave Conf.,* Sept. 1994, vol. 2, pp. 1010–1015.

[77] E.J. Griffin, T.E. Hodgetts, "Theoretical comparison of six-port reflectometer junction designs," in *IEEE Int. Microwave Symp. Dig.,* 1984, pp.575–577.

[78] T. Mack, A. Honold, J.-F. Luy, "An extremely broadband software configurable six-port receiver platform," in *European Microwave Conf.,* 2003, pp.623-626, Oct. 2003.

[79] C.M. Potter, G. Hjipieris, N.J. Fanthom, ”A novel 250 MHz-26.5 GHz reflection analyzer”, in 23rd *European Microwave Conference*, Oct. 1993, pp. 302-304.

[80] S. O. Tatu, E. Moldovan, K. Wu, and R. G. Bosisio, “A new direct millimeter-wave six-port receiver,” *IEEE Trans. Microw. Theory Tech.*, vol. 49, no. 12, pp. 2517–2522, Dec. 2001.

[81] S. Abielmona, H.V. Nguyen, C. Caloz, K. Wu, R.G. Bosisio, “Compact multilayer ultra-wideband six-port device for modulation/demodulation,” *Electronics Lett.*, vol. 43, no. 15, pp.813–814, July 2007.

[82] F. Wiedmann, B. Huyart, E. Bergeault, L. Jallet, “New structure for a six-port reflectometer in monolithic microwave integrated-circuit technology,” *IEEE Trans. Intrumentation Measurements*, vol. 46, no. 2, pp. 527–530, April 1997.

[83] J. Li, R.G. Bosisio, A. Koelpin, R. Weigel “Six-port receiver analog front-end: multilayer design and system simulation,” *IEEE Trans. Int. Microwave Symp. Dig.*, San Diego, CA, pp. 1659–1662, May 1994.

[84] I. Bahl, P. Bhartia, *Microwave solid state circuit design*, John Wiley & Sons, Inc., Chapter 11.2, 1988.

[85] G. F. Engen, “Calibrating the six-port reflectometer by means of sliding terminations,” *IEEE Trans. Microw. Theory Tech.*, vol. 26, no. 12, pp. 951–957, Dec. 1978.

[86] G.F. Engen, C.A. Hoer, "The application of "thru-short-delay" to the calibration of the dual six-port," in *IEEE MTT-S Int. Microwave Symp. Dig.,* vol. 78, no. 1, pp. 184-185, Jun. 1978.

[87] C.A. Hoer, "Choosing line lengths for calibrating network analyzers," *IEEE Trans. Microw. Theory Tech.,* vol. 31, pp. 76-77, Jun. 1983.

[88] J.D. Hunter, P.I Somlo, "An Explicit Six-Port Calibration Method Using Five Standards," *IEEE Trans. Microw. Theory Tech.,* vol. 33, no. 1, pp. 69-72, Jan 1985.

[89] T. Yakabe, M. Kinoshita, H. Yabe, "Complete calibration of a six-port reflectometer with one sliding load and one short," *IEEE Trans. Microw. Theory Tech.,* vol. 42, pp. 2035-2039, Nov. 1994.

[90] J. Li, R.G. Bosisio, K. Wu, 'Dual-tone calibration of six-port junction and its application to the six-port direct digital millimetric receiver', *IEEE Trans. Microw. Theory Tech.*, vol. 44, no. 1, pp. 93–99, 1996.

[91] Y. Xu, R.G. Bosisio, "On the real time calibration of six-port receivers (SPRs)," *Microw. Opt. Technol. Lett.*, vol. 20, no. 5, pp. 318–322, 1999.

[92] G. Neveux, B. Huyart, G.J. Rodriguez-Guisantes, "Wide-band RF receiver using the "five-port" technology," *IEEE Trans. Vehicular Technology*, vol. 53, no. 5, pp. 1441-1451, Sept. 2004.

[93] A. Stelzer, C.G. Diskus, R. Weigel, and H.W. Thim: "Using a six-port device in an FM-CW radar," *Proc. Int. Symp. Microwave and Optical Technology,* Montreal, Quebec, Canada, 2001, pp. 323–326.

[94] H. Zhang, L. Lin, K. Wu, "Software-defined six-port radar technique for precision range measurements," *IEEE Sensors Journal*, vol. 8, no. 10, pp.1745–1751, Oct. 2008.

[95] V.Y. Vu, A.J. Braga, X. Begaud, B. Huyart, "Measurement of direction-of-arrival of coherent signals using five-port reflectometers and quasi-Yagi antennas," *IEEE Microwave and Wireless Components Letters*, vol. 15, no. 9, pp. 558–560, Sept. 2005.

[96] B. Amante-Garcia, D. Kerneves, B. Huyart, "Measurement of direction of arrival for radar application," in *European Microwave Conf.*, Sept. 2002, pp. 1–4.

[97] Y. Zhao, J.-F Frigon, K. Wu, R.G. Bosisio, "Multi(Six)-port impulse radio for ultra-wideband," *IEEE Trans. Microw. Theory Tech.*, vol. 54, no. 4, pp. 1707–1712, June 2006.

[98] K.Mabrouk, B. Huyart, X. Begaud, A.B. Mohammed, "Baseband to baseband calibration of a MIMO wireless system," in *European Conf. Wireless Technologies,* Oct. 2007, pp.142–145.

[99] S. Haruyama, R. Morelos-Zaragoza, "A software defined radio platform with direct conversion: SOPRANO," in *Proc. IEEE Semiannual Vehicular Technology Conf.*, Atlantic City, NJ, Oct. 2001, pp. 1558–1560.

[100] X.Z. Xiong, V.F. Fusco, "Wideband 0.9 GHz to 5 GHz six-port and its application as digital modulation receiver," *IET Microw. Antennas Propag.*, vol. 150, no. 4, pp. 301-307, Aug. 2003.

[101] S.O. Tatu, K. Wu, T. Denidni, 'Multiband multiport direct conversion receiver: design, implementation and demodulation results', *Microw. Optical Technology Lett.*, vol. 48, no. 4, pp. 817–822, April 2006.

[102] K. Haddadi, H. El Aabbaoui, C. Loyez, D. Glay, N. Rolland, T. Lasri, 'Wide-band 0.9 GHz to 4 GHz four-port receiver', in *IEEE Int. Conf. Electron. Circuits and Systems,* Nice, France, Dec. 2006, pp. 1316–1319.

[103] C.-H. Wang, H.-Y. Chang, P.-S. Wu, K.-Y. Lin, T.-W. Huang, H. Wang, C.H. Chen, "A 60GHz low-power six-port rransceiver for gigabit software-defined transceiver applications," in *IEEE Int. Solid-State Circuits Conf. Dig. Tech. Papers,* Feb. 2007, pp. 192–596.

[104] P. Hakansson, G. Shaofang, "Ultra-wideband six-port transmitter and receiver pair 3.1-4.8 GHz," in *Asia-Pacific Microw. Conf.,* Hong Khong/Macau, China, Dec. 2008, pp. 1–4.

[105] P. Perez-Lara, J.A. Medina-Rodriguez, I. Molina-Fernandez, J.G. Wanguemert-Perez, A. Gonzalez-Salguero, "Wideband homodyne six-port receiver with high LO-RF isolation," *IET Microw. Antennas Propag.*, vol. 3, no. 5, pp. 882–888, 2009.

[106] K. Haddadi, M.M. Wang, C. Loyez, D. Glay, T. Lasri: 'Four-port communication receiver with digital IQ-regeneration', *IEEE Microw. Wireless Compon. Lett.*, vol. 20, no. 1, pp. 58–60, Jan. 2010.

[107] A. Martín-López, "Estudio comparativo de arquitecturas de RF para Radio Software", Proyecto Fin de Carrera, Escuela Técnica Superior de Ingenieros de Telecomunicación, Universidad Politécnica de Madrid, Dic. 2008.

[108] *TelMAX Project*: http://www.proyectotelmax.es

[109] R. Gomez-Garcia, M. Sanchez-Renedo, B. Jarry, J. Lintignat, B. Barelaud, "A class of microwave transversal signal-interference dual-passband planar filters," *IEEE Microwave and Wireless Components Letters,* vol. 19, no. 3, pp. 158–160, March 2009.

[110] R. Gomez-Garcia, J. Munoz-Ferreras, M. Sanchez-Renedo, "Signal-interference stepped-impedance-line microstrip filters and application to duplexers," *IEEE Microwave and Wireless Components Letters,* vol. 21, no. 8, pp. 421–423, Aug. 2011.

[111] M.A.S. Alkanhal, "Dual-band bandpass filter using inverted stepped-impedance resonators", *J. of Electromagn. Waves and Appl.*, Vol. 23, No. 8/9, pp. 1211–1220, 2009.

[112] X.M. Lin, "Design of compact tri-band bandpass filter using λ/4 and stub-loaded resonators", *J. of Electromagn. Waves and Appl.*, vol. 24, No. 14/15, pp. 2029–2035, 2010.

[113] R.M. Weng, P.Y. Hsiao: "Double-layered quad-band bandpass filter for multi-band wireless systems", *J. of Electromagn. Waves and Appl.*, vol. 23, no. 16, pp. 2153–2161, 2009.

[114] A. Garcia Lamperez, M. Salazar Palma, "Block coupling transformations in multiband filters," in *41st European Microwave Conference,* Manchester, UK*,* Oct. 2011, pp. 95–98.

[115] L. Li, D. Uttamchandani, "Demonstration of a tuneable RF MEMS band-pass filter using silicon foundry process", *J. of Electromagn. Waves and Appl.*, vol. 23, no. 2/3, pp.405–413, 2009.

[116] J. P. Shelton, J. Wolfel, R. Van Wagoner, "Tandem couplers and phase shifters for multi-octave bandwidth," *Microwaves*, vol. 4, pp. 14–19, April 1965.

[117] R. Mongia, I.Bahl, P. Bhartia, "RF and Microwave Coupled-Line Circuits," 1999 Artech House, Inc., ISBN 0-89006-830-5.

[118] C.M. Potter, G. Hjipieris, "Improvements in ultrabroadband TEM coupler design", *IEE proceedings* - part H, vol. 139, no. 2, pp 171–178, April 1992.

[119] E.G. Cristal, L. Young, "Theory and tables of optimum symmetrical TEM-mode coupled-transmission-line directional couplers," *IEEE Trans. Microwave Theory Tech.*, vol.13 No.5, pp. 544–558, Sept. 1965.

[120] P.P. Toulios, A.C. Todd, "Synthesis of symmetrical TEM-mode directional couplers," *IEEE Trans. Microwave Theory Tech.*, vol. 13, no. 5, pp. 536–544, Sept. 1965.

[121] Agilent Technologies. Advanced Design Systems (ADS): www.agilent.com/find/eesof-ads.

[122] Agilent Technologies. Momentum 3D planar EM Simulator: www.agilent.com/find/eesof-momentum.

[123] Hewlett-Packard Application Note 923, Schottky Barrier Diode Video Detectors.

[124] Hewlett-Packard Application Note 956-5, *Dynamic Range Extension of Schottky Detectors.*

[125] X. Xu, K. Wu, R.G. Bosisio, " Six-port networks," *Wiley Encyclopedia of RF and Microwave Engineering*, John Wily & Sons, Inc., Hoboken, NJ, vol. 5, pp. 4641–4669, 2005.

[126] R.A. Shafik, S. Rahman, R. Islam, N.S. Ashraf, "On the error vector magnitude as a performance metric and comparative analysis," in *Int. Conf. Emerging Technologies*, Peshawar, Pakistan, Nov. 2006, pp. 27-31.

[127] S.M. Winter, H.J. Ehm, A. Koelpin, R. Weigel, "Six-port receiver local oscillator power selection for maximum output SNR," *IEEE Radio and Wireless Symp.,* Jan. 2008, pp. 151–154.

[128] K. Wu.: 'Multiport interferometer techniques for innovative transceiver applications', in *IEEE Radio and Wireless Symp.,* New Orleans, LA, Jan. 2010, pp. 531–534.

[129] S. O. Tatu, T. A. Denidni, "New millimeter-wave six-port heterodyne receiver architecture," in *IEEE MTT-S Int. Microwave Symp. Dig.*, June 2006, pp.1999–2002.

[130] D. Rodríguez-Aparicio, "Diseño y caracterización de receptores zero-IF y low-IF para radio definida por software", Proyecto Fin de Carrera, Escuela Técnica Superior de Ingenieros de Telecomunicación, Universidad Politécnica de Madrid, Sept. 2010.

[131] K. Mabrouk, F. Rangel, B. Huyart, G. Neveux, "Architectural solution for second-order intermodulation intercept point improvement in direct down-conversion receivers", *IET Microw. Antennas Propag*, vol. 4, no 9, pp. 1377-1386, 2010.

[132] K. Mabrouk, B. Huyart, "Circuit analogique pour le calibrage large bande, la suppression des tensions parasites dues aux DC-offset et produits d'intermodulation IMD2 et réduction d'un convertisseur CAN pour les démodulateurs Zéro-IF ou Low-IF de type cinq-port et triphasé", Patent FR2934934 (A1) - 2010-02-12.

[133] R. Mirzavand, A. Mohammadi, A. Abdipour, "Low-cost implementation of broadband microwave receivers in Ka-band using multiport structures," *IET Microw. Antennas Propag.*, vol. 3, no. 3, pp. 483-491, 2009.

[134] Low Temperature Cofired Ceramic at IMST. Available: www.ltcc.de.

[135] S. B. Cohn, "A class of broadband three-port TEM mode hybrids", *IEEE Trans. Microw. Theory Tech.*, vol. 16, no. 3, Feb. 1968.

[136] S.M. Winter, A. Koelpin, R. Weigel, "Six-port receiver analog front-end: multilayer design and system simulation," *IEEE Trans. Circuits Sist. II*, vol. 55, no. 3, pp. 254–258, March 2008.

[137] A. Moscoso-Martir, I. Molina-Fernandez, "Six-port junction with complete UWB band coverage in multilayer technology," in *European Microwave Conf.,* Manchester, UK, Oct. 2011, pp. 655-658.

[138] Texas Instruments: http://www.ti.com.

[139] Analog Devices: http://www.analog.com.

[140] Linear Technology: http://www.linear.com.